MICROPEN DIRECT-WRITE TECHNIQUE FOR FABRICATION OF ADVANCED ELECTROCERAMIC AND OPTICAL MATERIALS

by

JINGJING SUN

A dissertation submitted to the

Graduate School-New Brunswick

Rutgers, The State University of New Jersey

in partial fulfillment of the requirements

for the degree of

Doctor of Philosophy

Graduate Program in Material Science and Engineering

written under the direction of

Professor Ahmad Safari

and approved by

_____

_____

_____

_____

New Brunswick, New Jersey

January, 2010

ABSTRACT OF THE DISSERTATION

MICROPEN DIRECT-WRITE TECHNIQUE FOR FABRICATION OF ADVANCED ELECTROCERAMIC AND OPTICAL MATERIALS

By JINGJING SUN

Dissertation Director:
Professor Ahmad Safari

Direct-write technologies, a subset of the rapid prototyping, have been applied for many applications including electronics, photonics and biomedical engineering. Among them, Micropen^{TM} is a promising technique, providing precision deposition of materials with various viscosities, on-line design changes and writing on nonplanar substrates. The objective of this project was to directly write two- and three-dimensional novel structures by Micropen^{TM} for potential optical and transducer applications.

First, to gain a basic understanding of Micropen^{TM} operation, poly(methyl methacrylate) (PMMA) solutions were developed as a model system. The effects of solution rheological properties on deposition conditions were investigated. Secondly, PMMA/SiO_2 hybrids were developed using sol-gel process. The effects of organic/inorganic ratios on thermal stability, microstructure and optical properties were studied. The solution with 80 wt% PMMA loading was chosen to deposit lines for optical applications.

Another application was the direct-write of lead zirconate titanate (PZT) thick films (6-70 μm) for MEMS or high frequency medical imaging applications. Pastes consisting of 15-30 vol% ceramic loading in a sol-gel solution were prepared for the deposition of films on various substrates. The PZT sol was used as a binder as well as to achieve low temperature heat treatment of the films. Using the 15 vol% paste with a 250-μm pen tip, a four-layer film was deposited on a silicon substrate. This 16-μm film with 1 cm^2 area had K of 870, tanδ of 4.1%, P_r of 12.2 $\mu C/cm^2$ and E_c of 27 kV/cm.

Furthermore, Micropen^{TM} was utilized for the direct-write of ceramic skeletal structures to develop PZT ceramic/polymer composites with 2-2 connectivity for medical ultrasound transducers. Ceramic/binder based pastes were developed as writing materials. The 35 vol% paste exhibited shear thinning with a viscosity of 45 Pa·s at lower shear rate and 3 Pa·s at higher shear rate. Using a 100-μm pen tip, the fabricated composite with ~360 μm height had resonance frequencies of ~4 MHz, and electromechanical properties of K=650, tanδ=2.1%, k_t=0.60 and d_{33}=210 pC/N. Finally, composites with linear and Gaussian volume fraction gradients were fabricated by Micropen^{TM}. Their vibration amplitude profiles showed maximum output at center with gradual decreasing towards edge of the composites.

DEDICATION

This dissertation is dedicated to

my parents

Changxu Sun and Guizhen Zhao

ACKNOWLEDGEMENTS

I would like to take this opportunity to thank my thesis advisor Dr. Safari for his guidance and support throughout this thesis work. He demonstrated many important qualities that made a deep impression upon me such as being a hard worker, having a positive attitude and the being able and willing to work on a team. I am also very grateful to the members of my thesis committee, Dr. Klein, Dr. Danforth and Dr. Vittadello, for providing their valuable comments and taking time to review my thesis. In particular, I would like to thank Dr. Klein for being a great graduate director who always encouraged me and supported my research and graduate life, especially in difficult times. I would like to thank Dr. Vittadello for his enormous help in the lab and for his advice on writing technical papers.

I would like to thank Dr. Sigel for the instruction on analysis of optical properties; Dr. Jadidan for helpful discussion on my research; Dr. Pan for his help in FTIR measurement; and all the other professors who taught my courses and gave me help on research, such as Dr. Lehman, Dr. Cosandey, Dr. Greenhut, Dr. Birnie and Dr. Cannon.

Special thanks to the previous group members: Dr. Akdogan, Dr. Allahverdi, Asha, Nader, Irina and Bill; current graduate students: Maryam, Note and undergraduate students. Their help in my daily research and life was immeasurable and deeply appreciated.

I also wish to thank all the other graduate students and friends who helped and encouraged me during my graduate life, such as Yangyang, Jen, Wantinee, Milca, Beril, Kim, Navin, Julianne, Dr. Lai Qi, Dr. Yiyun Yang, to name a few. I am also grateful to

Mr. John Yaniero who helped me with lab equipments, and all the staff members in our department.

I would like to acknowledge the financial support of the Glenn Howatt Foundation at Rutgers University and New Jersey Commission on Science & Technology.

Last but not least, I appreciate my dear parents, Changxu Sun and Guizhen Zhao, very much. They are one of the greatest parents in the world. They have tried their best to love and support me in every way. Even now that they are both very sick, they are still supporting me to finish my Ph.D. degree in the U.S., while struggling with extremely difficult conditions by themselves in China. I also owe a very big thanks to my husband, Geliang Sun. He is always at my side, encouraging and supporting me. With him, I have been able to overcome many obstacles such as no scholarship since July 2006, having a baby and dealing with my parents' illness. I also need to thank our 2-year old son, Zhuangzhuang, for providing a lot of fun, deeper meaning in life and new hope for the future.

Table of Contents

Lists of Tables

List of Figures

CHAPTER1 INTRODUCTION

This chapter provides a literature review on direct-write techniques, which is organized into three sections: (1) The concept of direct-write is presented, and ink-jet printing and laser deposition are given as two examples. (2) Micropen^{TM} technique is introduced as a promising direct-write technique, and its basic operation and features are described. (3) The previous studies on the Micropen^{TM} are summarized to demonstrate its feasibility of direct writing multilayer, multimaterial ceramic components and thick films.

1.1 Direct-write techniques

It is expected that new technologies for materials fabrication will drive scientific and technological advances in areas of material science, chemistry, physics and biology. Direct-write technologies are among the emerging novel approaches to the fabrication of electronics and photonics devices, sensors, integrated power sources, tissue engineering scaffolds and drug-delivery devices, using different materials [1,2,3,4]. Direct-write technologies are a subset of the larger family of rapid prototyping. The term "direct-write" is used to describe fabrication methods that employ a computer-controlled translation stage, which moves a pattern-generating device, such as an ink deposition nozzle or laser writing optics, to create materials with controlled composition, pattern and architecture[5]. In direct-writing, in contrast to the manufacturing methods based on lithography, materials are deposited additively only where needed. This results in a more environmentally friendly approach, since processing involves fewer steps and less waste. In addition, low temperature fabrication can be accomplished, thus enabling manufacturing on flexible substrates (such as plastic or paper). Although most direct-write techniques are in relevant in the mesoscale regime (10 μm-several mm), at a bigger

size than that achievable by photolithography, their advantages lie in the rapid prototyping, design's versatility, cheaper and faster small-lot production and the ability to construct three-dimensional (3D) structures.

Several direct-write techniques to create 3D structures or 2D surfaces are summarized by Lewis[5] (Table 1.1), including ink-jet printing, robocasting, fused deposition of ceramics (FDC) and Micropen™ writing. The techniques can be divided into two approaches in terms of the types of writing materials: droplet and filament-based approaches (Fig. 1.1). Fig. 1.2 schematically shows three of these techniques: ink-jet printing, robocasting and FDC.

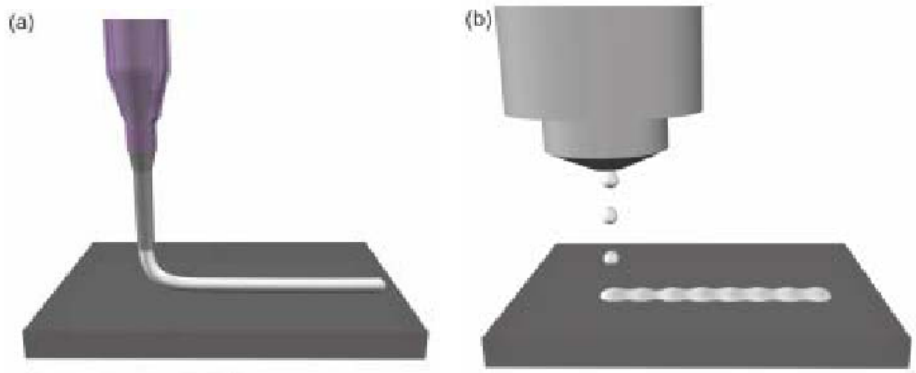

(a) (b)

Fig. 1.1 Schematic view of ink-based deposition schemes (a) continuous filament writing and (b) droplet jetting[6].

Table 1.1 Several direct-write techniques.

	Ink design	**Minimum printed feature size**
Droplet-based		
3D printing	Binder solution printed on powder bed	170 μm (lateral), 45μm (depth)
Ink-jet printing	Colloidal fluid	20 μm (lateral),100 nm (height)
Hot-melt ink-jet printing	Colloidal-filled wax (max. solids ~40%)	70 μm (lateral), <1μm (height)
Filament-based		
Robocasting (in air)	Concentrated colloidal gel	500 μm (diameter)
Robocasting (in oil)	Concentrated colloidal gel Concentrated nanoparticle gel	200 μm (diameter) 30 μm (diameter)
Fused deposition of ceramic (FDC)	Particle-filled polymer melt (max. solids ~ 60 vol%)	100 μm (diameter)
Micropen writing	Concentrated colloidal fluid	25 μm (diameter)

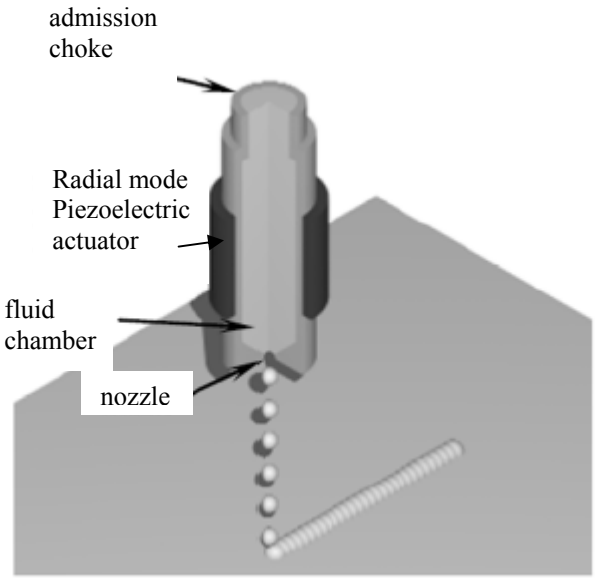

(a) ink-jet printing

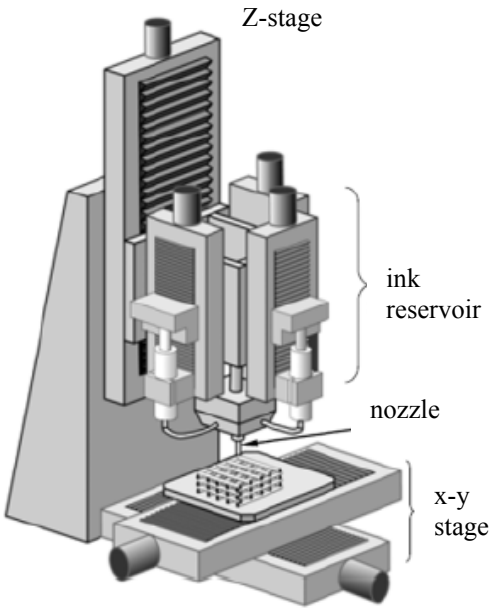

(b) robocasting

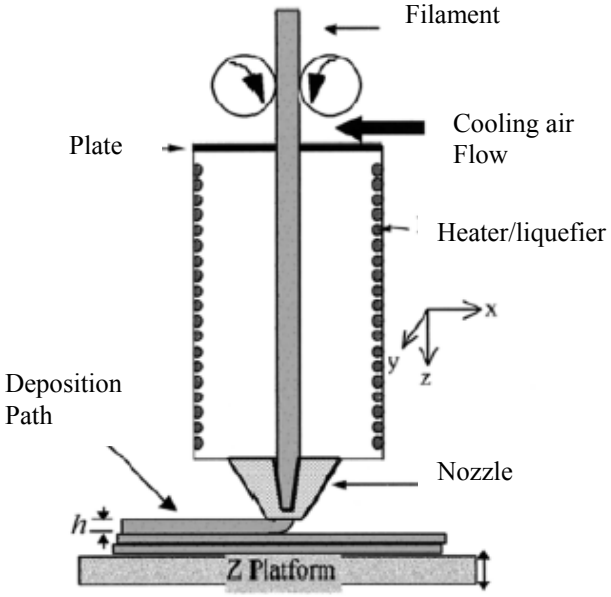

(c) FDC

Fig. 1.2 Schematic illustration of (a) Ink-jet printing, (b) Robocasting and (c) Fused Deposition of Ceramics (FDC)[5].

One of the direct-writing techniques has been widely used is ink-jet printing. This technique consists of the deposition of micro-droplets ejected via ink nozzle to build the successive layers of 2D or 3D structures. In continuous type of printers, an electric charge is imparted to the drops, which can be steered by applying an electrostatic field. Drops not required for printing are captured into the reservoir for recycling[7]. In the drop-on-demand type of printers, a volumetric change in the ink is induced by the application of a voltage pulse to a piezoelectric material that is coupled to the ink. The voltage is applied only when a drop is desired. In both printer types, nozzle sizes can be as small as 20-30 μm. The resolutions of ~10-50 μm can be achieved by adjusting the aperture of printing head, the rheology and surface tension of the ink, and the ejection and spreading phenomenon of droplets. A typical ink has a low viscosity < 2 mPa·s (cP), but printers can be designed to handle liquids up to 100 mPa·s. The main issue of printing process is to avoid clogging of the nozzle due to solvent drying.

Ding *et al.* deposited $BaTiO_3$ films by ink-jet printing using a dilute aqueous (8 vol%) $BaTiO_3$ colloidal ink[8]. The $BaTiO_3$ powders were prepared from the hydrothermal process with particle sizes of 100-200 nm. The films had a thickness of 1.5 μm, and the uniformity of the films was adjusted by the variation of printer and image file resolutions. PZT suspensions for ink-jet printing have been studied by Lee *et al.* [9]. To reduce particle size and break agglomerates, the PZT suspensions were ball milled for 18 h or attrition milled for 6h. 10-30 vol% PZT suspensions in organic solvent medium with lower viscosities of 5-15 mPa·s were developed for room temperature deposition, and 20-25 vol% suspensions in wax medium with higher viscosities of 10-20 mPa·s were used for high temperature (60 ºC) deposition.

In addition, several groups have demonstrated the feasibility of building 3D structures by ink-jet printing. Seerden *et al.*[10] have developed a 30 vol% alumina-filled wax, which was printed at 100 ºC to form 3D structures. The structures had high aspect ratio walls with a minimum lateral feature size of ~100 μm (Fig. 1.3(a)). Zhao *et al.*[11] have demonstrated the similar structures with minimum wall thickness of ~340 μm using a 14 vol% zirconia (ZrO_2) suspension (Fig. 1.3(b)). Noguera *et al.*[12] have built a 3D PZT pillar array corresponding to the skeleton of 1-3 ceramic/polymer composites for medical imaging (Fig. 1.3(c)). The PZT powder was attrition milled to 1 μm for a printing head aperture of 60 μm. The ink was a 10 vol% PZT suspension with a viscosity of 10 mPa·s. The pillar had a diameter ~90 μm, and a height of ~300 μm. However, they did not report the fabrication of PZT/polymer 1-3 composites using the PZT pillars.

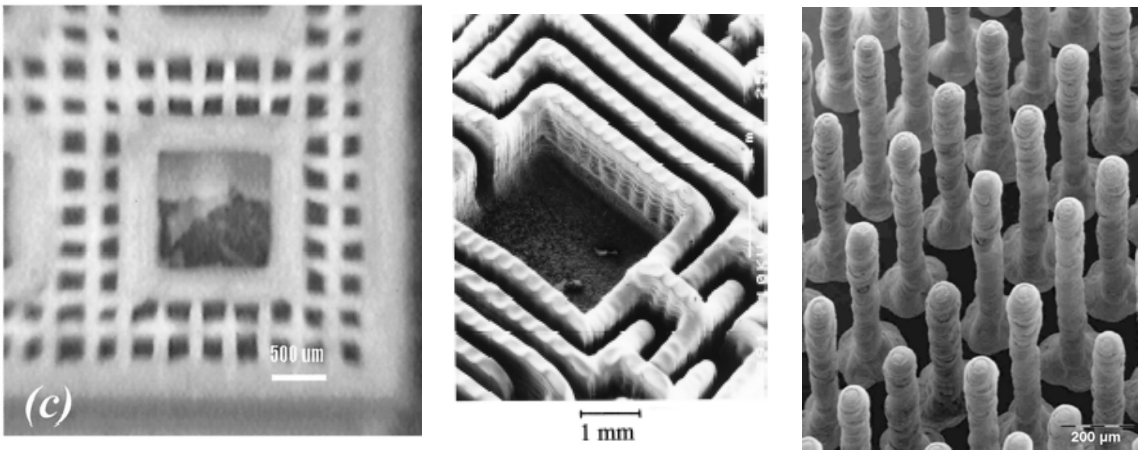

(a) (b) (c)

Fig. 1.3 Optical pictures of 3D structures built by ink-jet printing (a) a ceramic body using an alumina/wax ink[10], (b) a maze using a ZrO_2 suspension[11], and (c) a green PZT pillar array using a PZT suspension[12].

Laser deposition is another direct-write technique. It has become an important alternative to lithographic processes for generating high-resolution patterns. In these approaches, a pulsed laser is used to induce the transfer of materials from a source film onto a substrate close to or in contact with the film[13]. Fig. 1.4 shows a schematic illustrating the basic elements required for a laser forward-transfer apparatus. The laser is focused onto a layer of material mounted on the donor substrate. Ejected material is collected on the acceptor substrate, which can be manipulated by a translation stage. The original laser-induced forward transfer uses a laser to vaporize a thin film from a laser transparent donor substrate. This mechanism of material transfer is not useful for direct writing of complex multicomponent metal oxides, polymers and composite materials. Another method of laser deposition has been developed, called matrix-assisted pulsed-laser evaporation (MAPLE) direct write[14]. Briefly, MAPLE utilizes a frozen target made from a volatile solvent and a dilute solution of organic material to be deposited. When the laser pulse strikes the surface of the target, the solvent is vaporized and pumped away, while the organic material is released and collected on the substrate, forming a highly uniform thin film with minimal organic decomposition. In this process, the transferred material is not vaporized, which allows for the transfer of complex compounds without affecting their composition, phase and functionality. The resolution of ~10 μm can be achieved in this technique.

The laser direct-write technique has been applied to various materials for many applications including electronics and biomedical engineering[15]. Fig. 1.5 (a) shows a fine feature test pattern with a line width of ~50 μm on low temperature co-fired ceramic (LTCC), using commercial silver paste, deposited in the work of Zhang[16]. They also

demonstrated the fabrication of RF filter test vehicle on LTCC. Fig. 1.5 (b) shows a SEM image of the cross section of a $BaTiO_3$ capacitor made by MAPLE direct-write in the work of Piqué *et al.*, using a 25-μm laser spot. Fig. 1.5 (c) shows the optical image of Zn_2SiO_4: Mn pixels for high-definition displays stimulated by a MAPLE direct-write[17].

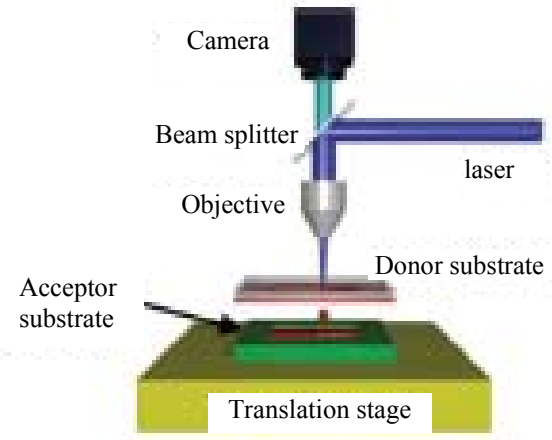

Fig. 1.4 Schematic illustration of a laser direct-write addition forward-transfer apparatus[13].

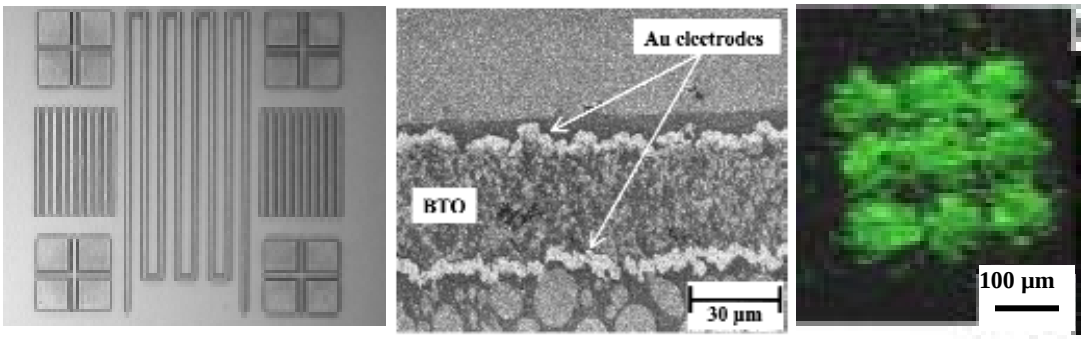

(a) (b) (c)

Fig. 1.5 (a) Fine feature test pattern with 50 μm line width (before firing) by laser deposition[16], (b) SEM image of a parallel plate capacitor made by MAPLE direct-write[14], and (c) a 3×3 array of Zn_2SiO_4:Mn phosphor deposited by MAPLE[17].

1.2 Micropen™: a promising direct-write technique

The need for fabrication of hybrid microelectronics increasingly requires multimaterials integration, rapid prototyping writing, and deposition on nontraditional substrates. One of the promising solutions to these challenges is the Micropen™ direct-write. Micropen™ is also an example of Solid Freeform Fabrication (SFF) techniques employed to produce a variety of electroceramic components[3]. One significant factor of utilizing the Micropen™ technique is to deposit thick films with thickness in the range of 1-10 μm, which covers the gap between thin film fabrication (up to 1 μm) and screen printing (>10 μm).

Fig. 1.6 shows the basic structure and operation of the Micropen™ system (OhmCraft Inc., Honeoye Falls, NY). It has been utilized for the deposition of commercial electronic circuitry with integrated passive components, such as resistors, capacitors and inductors. A new direction is the deposition of electrodes, bio-reagent solutions, sealing and heating elements on medical devices[18]. Similar to other direct-write techniques, the Micropen™ is a computer-automated equipment for precision printing of liquids or particulate slurries. It has a computer driven x-y stage which moves during deposition (a pen tip does not move), where print patterns are designed by AutoCAD software. Because print files in CAD can be easily modified, Micropen™ writing permits easy on-line design changes, in contrast to screen printing which needs a new screen for a pattern change. In addition, in contrast to tape casting, the Micropen™ technique is inherently capable of depositing multimaterials in one layer, by simply switching the pump block loaded with different materials.

Different deposition geometries can be obtained by Micropen™ technique, such as fine line traces and filled regions. The resolution of the Micropen™ is mainly determined by pen tip sizes, material rheology and writing parameters. In general, printed feature sizes vary from 25 micron to several millimeters, when using pen tips with different inner diameters from 25-2,500 μm (i.e. 1-100 mil).

Fig. 1.6 also shows that the writing material is loaded into a syringe which is then connected to a pump block in the Micropen™ system. A pneumatic ram compresses the plunger of the syringe and forces the material into the pump block, and then through a pen tip. The pump block has two internal chambers, which provide continuous, smooth delivery of materials. The key to obtaining uniform and consistent deposition quality is elimination of air bubbles in a writing material. This can be accomplished by centrifuging the syringe or bleeding air from the pump block before and during the deposition process. It is also important to maintain a uniform solids loading and viscosity to have uniform deposition.

Writing materials for the Micropen™ technique are liquids or particulate pastes (or slurries). The rheological requirements for thick-film pastes in the Micropen™ and screen printing are nearly identical[20]. Hence, most commercial screen printing pastes can be utilized in the Micropen™ technique. The pastes used in Dimos and Lewis' work had viscosities in the range of 25-300 Pa·s[20-23]. Moreover, a large variety of fluids with different viscosities can be employed as writing materials, such as water (0.001 Pa·s) and honey (>1 Pa·s)[19].

Another critical advantage of the Micropen™ technique is its ability to deposit on virtually any substrate, such as irregular surfaces and tubes. This is related to one of the

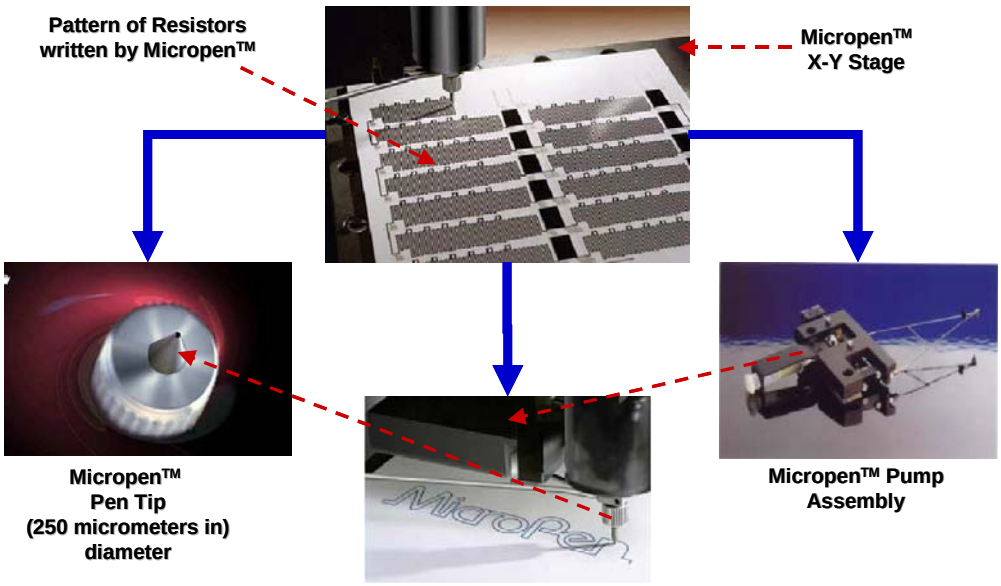

Fig. 1.6 The Micropen™ direct-write system[19].

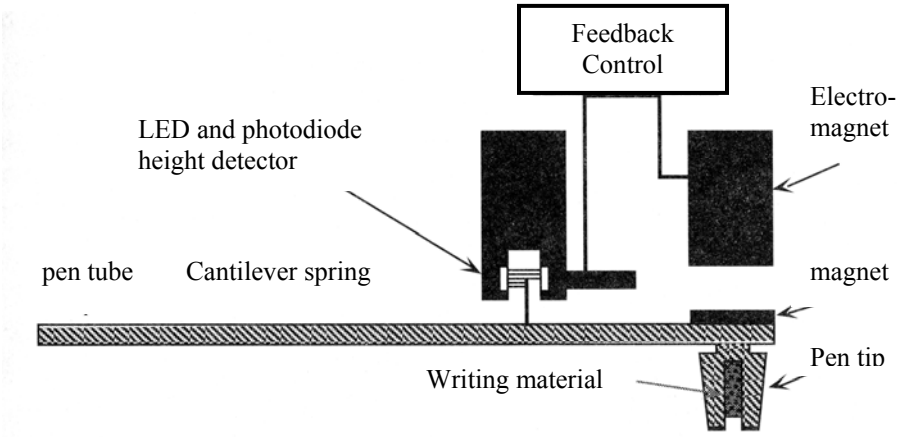

Fig. 1.7 The schematic of "dynamic pen control"[1].

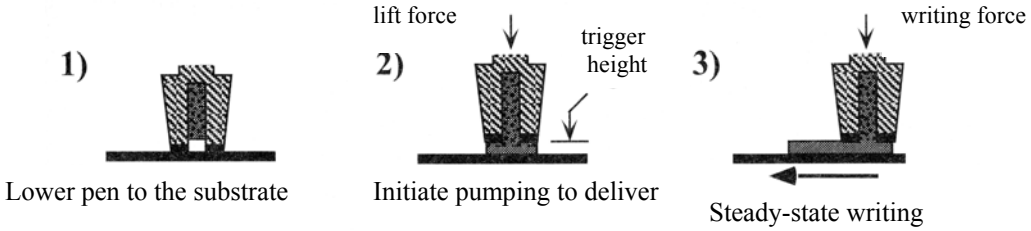

Fig. 1.8 The schematic of how to write using the Micropen™ technique[1].

Micropen™ features, called "dynamic pen control" [19]. Fig. 1.7 shows that "dynamic pen control" controls the force that a pen tip exerts on writing materials, without actually touching the substrates. The control is generated by the interaction between a small disc-shaped magnet and a larger electromagnet, and the pen height is sensed by an infrared photodiode height sensor on the pen tube. This feature enables the Micropen™ to have excellent control of the print thickness, as well as the ability to print on cambered and uneven substrates.

In the Micropen™, the movement in z direction is not automated, and the pen tip height needs to be calibrated and adjusted if changed to a new position. In addition, a deposited layer must be dried before depositing on top of it. Therefore, the Micropen™ is better suited for producing multilayer electronic devices on planar and curvilinear substrates[5], but not directly suited for building three-dimensional (3D) structures.

Fig. 1.8 shows how lines are written using the Micropen™ technique. The basic steps are as following[19]:

(1) Before writing starts, a material is withdrawn slightly into a pen tip.

(2) Then the X-Y table moves in place and the pen tip is lowered to the substrate. A slight downward force ("lift force") (normally 0-50 mg) is placed on the pen tip to prevent the tip from rising.

(3) The pump begins dispensing material at "lift speed" until the material reaches the substrate and lifts the pen tip to a predetermined height ("trigger height").

(4) When writing begins, the table moves at "writing speed", and the pen tip is under "writing force". During writing, a uniform amount of materials with a designed "cross section" is delivered.

(5) After writing, the pump is reversed at “termination speed” till “termination volume” amount of material is withdrawn into the pen tip. Finally, the pen lifts and waits for the next writing.

In addition, there are various writing parameters in the Micropen™ system, which can be divided into several groups: setup (to use during the entire writing process), line start (to control the beginning of writing), line writing (to use during writing), line stop (to ensure good line terminations and also to affect the next line start) and burst pump (a “burst” of pumping to reach the proper pressure during writing required for some materials) parameters. To obtain high quality writing, these parameters need to be varied depending on the specific pen tip size and material in use. Table 1.2 summarizes the definitions, setting values and effects of the main writing parameters of this technique[19].

Table 1.2 The definitions, setting values and effects of main writing parameters of the Micropen™ system[19].

	Parameters [unit]	Definition	Typical & valid settings	Effects
Setup parameters	**Cross section (CS) [mil^2]**	The volume of writing material dispensed in a single pass of a pen tip. CS=line width × line height; volume=CS × length of the pen path	20 mil^2; 1-1000 mil^2	CS allows for a precise control of the volume of writing materials.
Line start parameters	**Trigger height (TH) [mil]**	Before writing, a pen tip is lifted above the substrate to a predetermined height (TH) to allow air to escape.	0.2 mil; 0-100 mil	(a) Must be high enough to allow air to escape; (b) excess TH: too much material at line starts; (c) generally should < 1s to reach TH; (d) decrease TH for narrow lines; (e) increase TH when WS is fast.
	Lift force (LF) [mg]	Before writing, the system exerts a slightly downward force placed on a pen tip during pumping, to prevent the tip from rising.	0-50 mg; -1000-1000 mg	(a) Too high: too much material at the beginning; (c) Too low: the pen tip may float up, causing false line starts.
	Lift speed (LS) [mil^3/sec]	Before writing, the speed at which a material is delivered during pumping until TH is reached.	800-12500 mil^3/sec; 1-100000 mil^3/sec	(a) Too low: material may ooze out the sides of a pen tip without raising the pen to TH, resulting in too much material at the beginning; (b) Too high: line starts may be too wide; (c) For maximum efficiency, use the highest LS that gives the desired result.
Line writing parameters	**Writing force (WF) [mg]**	The downward force on a pen tip during writing.	10 mg; -1000-1000 mg	(a) High (or low) WF for wider (or narrower) lines; (b) Filling area usually uses high WF.
	Writing speed (WS) [mil/sec]	How fast the X-Y table moves during writing.	750 mil/sec (for a 10-mil pen,CS=20mil^2) 1-100000 mil/sec	(a) High WS: rounded corners; (b) High (or low) WS requires higher (or lower) WF and Burst Volume.

Line stop parameters	**Termination volume (TV) [mil^3]**	How much material is pumped in the reverse direction after writing.	12500-22500 mil^3; 0~10000000 mil^3	(a) Too low: too much material at the beginning of the next line; (b) Too high: the time required to reach TH may be excessive.
	Termination speed (TS) [mil^3/sec]	The speed at which material should be pumped in the reverse direction after writing.	500,000 mil^3/sec; 1-100000000 mil^3/sec	To regulate reverse pumping, change TV before change TS.
Burst pump parameters	**Burst volume (BV) [mil^3]**	How much burst pumping should occur to bring the material up to the deliver pressure after TH is reached	0-8000 mil^3; 1-100000000 mil^3	(a)Too low (high): narrow (wide) line starts; (b) Burst pumping is not used with small CS and slow WS.
	Burst speed (BS) [mil^3/sec]	How quickly material is pumped during burst pumping.	500,000 mil^3/sec; 1-100,000,000 mil^3/sec	To regulate burst pumping, change BV before change BS.

1.3 Previous studies on the Micropen™ technique

The original work on the Micropen™ direct-write started in Sandia National Laboratories (New Mexico) in 1997. Dimos *et al.* fabricated several integrated, multilayer electronic components by the Micropen™ technique (shown in Fig. 1.9 a), and did the primary investigation on the influence of paste rheology on line resolution and surface topography[20,21]. They used commercial screen printing thick-film pastes, such as dielectric, Ag conductor and RuO_2-based resistor slurries. There are several important conclusions in their work:

(1) They introduced the concepts of "printing range" and "settling range". Fig. 1.9 (b) shows the slurry viscosities as a function of shear rate. The "printing range" corresponds to higher shear rates (20-85 s^{-1}), while the "settling range" corresponds to lower shear rates (<1 s^{-1}). The rheological behavior of a writing material in "printing range" affects the writing parameters during printing, and that in "settling range" determines line resolution and surface topography of printed patterns.

(2) The pastes in their study exhibited shear thinning behavior (shown in Fig. 1.9 (b)). The viscosities in the "printing range" were about 25-100 Pa·s, and such convergence indicated that the writing parameters do not need to be varied greatly for different formulations. In contrast, the paste viscosity showed significant differences (50-500 Pa·s) at low shear rates ("settling range"), and consequently pastes need to be optimized for either high definition patterns or smooth filled regions. The resulting line resolution and surface topography are mainly determined by paste rheology at "settling range".

(3) It was also observed that although the paste viscosities were similar, the difference in drying condition also affected printing ability, thus the selection of a solvent was critical in making a suitable paste.

Following the study above was the collaborative work of Sandia National Laboratories and Lewis' group at University of Illinois at Urbana-Champaign. They developed rheologically tailored, cofireable thick-film pastes of functional ceramic materials (e.g. $Pb(Nb,Zr,Ti)O_3$ and ZnO) for capacitor and varistor applications[22,23]. The steps for tailoring a paste rheological behavior in their study included:

(a) Dispersant evaluation by varying the type and concentration of dispersants;

(b) Maximum packing fraction determination for suspensions by varying the amounts of powder (5-40 vol%);

(c) Vehicle system test by varying the volume fraction of binder (ethyl cellulose) in terpineol vehicle.

After the investigation on paste rheology, the contents of optimized $Pb(Nb,Zr,Ti)O_3$ paste were: 35 vol% powder with 1 wt% Menhaden fish oil (MFO) (as dispersant) and 5 vol% ethyl cellulose (as binder) in terpineol. Similarly, the developed ZnO paste contained 35 vol% powder, with 3 wt% MFO and 5 vol% ethyl cellulose in terpineol. Both $Pb(Nb,Zr,Ti)O_3$ and ZnO pastes exhibited shear thinning behavior. The viscosities reported for PNZT and ZnO pastes were ~60-200 and 300-700 Pa·s (at shear rate=10 s^{-1}), respectively.

The Electroceramics Research Group at Rutgers University has adopted the Micropen^{TM} technique for direct writing of thick films of lead zirconate titanate (PZT) and barium strontium titanate (BST). These films can be used for ferroelectric and

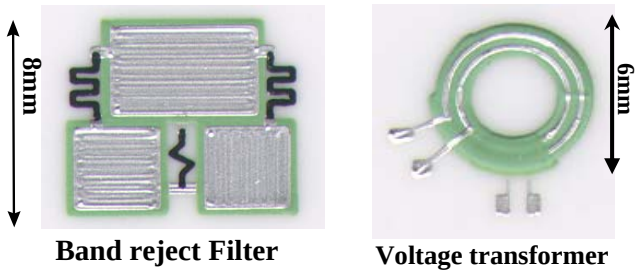

(a)

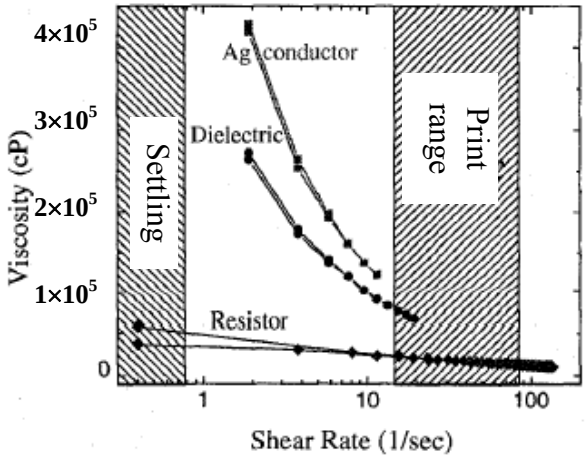

(b)

Fig. 1.9 (a) a 4-layer band reject filter and a voltage transformer fabricated by the Micropen™ and (b) Pastes' viscosity as a function of shear rate[20,21].

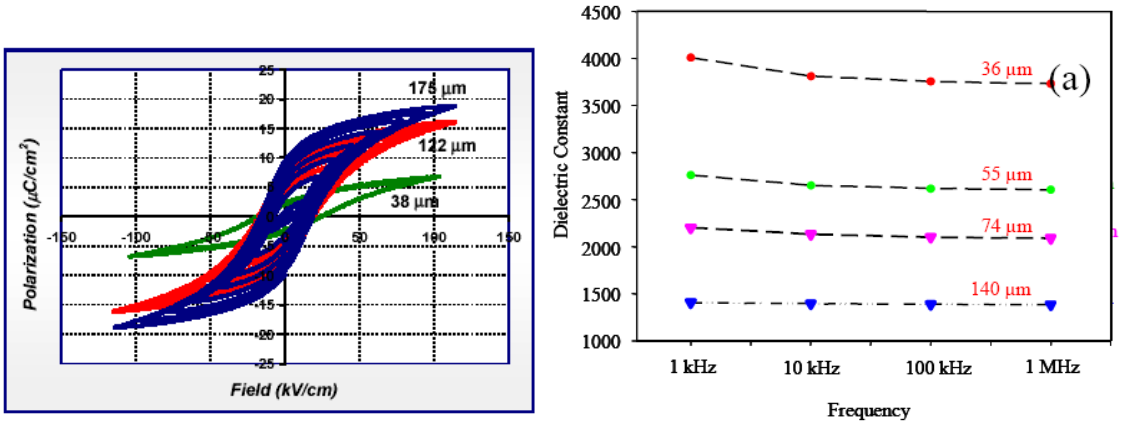

(a) (b)

Fig. 1.10 (a) Hysteresis loops for the PZT-2 wt% LB films and (b) dielectric constants of the BST films deposited by the Micropen™ [24,25].

piezoelectric applications, and capacitors for radio frequency (rf) and microwave components. The pastes composition and preparation were similar to the work in Lewis' group, except that stearic acid was used as a dispersant instead of fish oil. The film thickness was in the range of 10-200 μm, and was sintered at 1000-1300 ºC. Allahverdi *et al.* investigated the effects of three sintering aids on the microstructures and properties of PZT thick films[24]. It was found that the 2 wt% lithium bismuth oxide (LB) had a positive effect on the PZT properties. Fig. 1.10 (a) shows the hysteresis loops of three PZT films deposited by the Micropen^{TM} with 2 wt% LB additive. It reveals the thickness effect on the films' ferroelectric properties. For example, the remanent polarization increased from ~3 μC/cm^2 for the thinnest film (38 μm) to ~10 μC/cm^2 for the thickest film (175 μm). Kunduraci *et al.* deposited BST thick films by the Micropen^{TM} technique, and studied the residual stress, dielectric and ferroelectric properties of the thick films as a function of film thickness[25]. For example, Fig. 1.10 (b) shows the dielectric constant of the BST films decreased with increasing film thickness.

1.4 Summary

Micropen™ is a promising direct-write technique. It provides precision deposition of pastes with a wide range of viscosities, permits on-line design changes, and allows writing on nonplanar substrates. The writing quality and resolution of Micropen™ depends on pen tip size, paste rheology and writing parameters. This direct-write approach has been demonstrated for fabricating multilayer, multimaterial integrated ceramic components in an agile way, such as RC filters and voltage transformers. Thick films of PNZT, ZnO, PZT and BST have also been deposited and investigated for a variety of applications including capacitors and varistors.

CHAPTER2 STATEMENT OF PROBLEM AND METHOD OF ATTACK

In recent years, direct-write technologies have drawn increasing attention due to the advantages of rapid prototyping manufacture, such as design flexibility and fast small-lot production. Compared to the indirect methods such as photolithography, direct-writing allows additive deposition of materials only where needed. Fewer steps and less waste are involved in processing. As one of the promising direct-write technologies, the Micropen^{TM} provides precision deposition of pastes (or slurries) with a wide range of viscosities, permits on-line design changes, and allows writing on nonplanar substrates.

The Micropen^{TM} direct-write has been utilized for the fabrication of integrated, multilayer, multimaterial electronic components, such as capacitors, resistors and inductors. However, many other potential applications for the Micropen^{TM} technique represents attractive goals, such as the direct writing of organic/inorganic materials for optical applications, and the direct writing of thick films for microelectromechanical systems (MEMS) or high frequency medical imaging transducers. These two-dimensional (2D) structures are generally fabricated by spin-coating, screen printing and lithographic processes. The advantages of using the Micropen^{TM} direct-write include simplifying the process, avoiding the usage of molds and masks, reducing the cost and environmental impact. In addition, although the Micropen^{TM} has been proven to be well suited for the deposition of two-dimensional structures, its capability of building three-dimensional (3D) structures has not been reported. For example, for the fabrication of thin layer of ceramic/polymer composites for medical ultrasound transducers (1-10 MHz), traditional manufacturing techniques (such as dice-and-fill and injection molding) are not suitable for building novel and complex designs. Dicing or molding process could be avoided in

the fabrication of ceramic skeletal structures for composites, and novel designs would be accessible by utilizing the Micropen™ direct-write technique.

Therefore, this thesis work was focused on the demonstration of the feasibility of fabricating novel 2D and 3D designs using the Micropen™ direct-write, for potential applications such as optical, ferroelectric and piezoelectric devices. The main objectives of this thesis were:

- To synthesize and fully characterize organic/inorganic hybrid materials, and then directly write hybrid lines for optical applications.
- To fabricate lead zirconate titanate (PZT) thick films (10-100 μm in thickness) on silicon and alumina substrates, for MEMS or high frequency medical imaging transducers.
- To design and fabricate ceramic skeletal structures for the fabrication of ceramic/polymer composites (300-400 μm in thickness), for transducers including medical imaging applications.
- To design and build ceramic/polymer composites with volume fraction gradient (VFG), and to study the effects of different volume gradients (such as linear and Gaussian) on the electromechanical properties of the composites.

Micropen™ direct-write is a relatively new technique, thus the first step of this study was to gain a basic understanding of its operation for materials with various viscosities. Poly(methyl methacrylate) (PMMA) polymeric solutions with different concentrations were developed as a model system for the Micropen™ deposition. The rheological properties of the PMMA solutions were studied, and their effects on the deposition conditions and the dimensions (line width and height) of PMMA lines were

investigated. Such study provided valuable feedback to optimize the Micropen™ parameters for materials with comparable rheological properties. Based on the study on the PMMA solutions, various Micropen™ parameters were optimized for different writing materials and pen tips in the following studies.

The organic and inorganic hybrid system, PMMA/SiO_2, is important for optical applications. A hybrid sol-gel process was used to synthesis PMMA/SiO_2 hybrid monoliths with different organic/inorganic ratios. The effects of the PMMA/SiO_2 ratios on thermal stability, microstructure and optical properties of the monoliths were fully characterized. This study helped in understanding the formation of hydrogen bonding between the organic and inorganic phases and the optical properties of the monoliths. The PMMA/SiO_2 hybrid with the optimal composition was used for the direct writing of lines by the Micropen™ technique, and the dimensions (line width and height) and morphology of deposited lines were investigated.

For the deposition of thick films, a modified sol-gel process was combined with Micropen™ direct-write for the first time. The purpose was to achieve low temperature annealing as well as the deposition of one-layer film (1-17.5 μm) thicker than those deposited via a traditional sol-gel process. The writing material was prepared by dispersing commercial PZT powder in a PZT sol. The PZT sol was used as a binder in the system. Pastes with different solids loadings were designed, and their viscosities were measured. Other issues such as heat treatment profiles for the PZT pastes, film deposition procedures, and paste uniformity were investigated to prepare thick films with relatively high dielectric and ferroelectric properties. In addition, a critical Micropen™ parameter, “cross section” was studied to obtain films with controlled thickness. Films with different

thicknesses were deposited to study the effects of film thickness on the dielectric and ferroelectric properties.

Micropen^{TM} was used for the first time in the fabrication of ceramic/polymer composites. The main challenge in this study was to successfully deposit fine scale and high aspect ratio 3D ceramic skeletal structures. Therefore, ceramic/binder based pastes were prepared as writing materials to obtain more stability and higher viscosities (>0.3 Pa·s at shear rate=1 s^{-1}). Pen tips of different sizes (100, 150 and 250 μm in inner diameter) were used for the deposition of paste with the highest solids loading with the smallest pen tip size. In addition, different ceramic volume fractions in the composites were designed by AutoCAD software to study its effects on the composite properties. The optimized procedures of binder burnout, sintering, polishing and poling were established for the composites fabrication. The dielectric, piezoelectric and electromechanical properties of the composites (300-400 μm in thickness) were characterized and evaluated.

The volume fraction gradient (VFG) ceramic/polymer composites were designed to reduce the side and grating lobe intensities in medical ultrasound transducers. Composites with two types of gradients (Gaussian and linear) and two geometries (rectangular and annular) were designed and fabricated by the Micropen^{TM} technique. Beside characterization of dielectric, piezoelectric and electromechanical properties, vibration amplitude profiles of the composites were measured as function of ceramic gradient.

CHAPTER3 MODEL PMMA SOLUTIONS FOR THE BASIC STUDY OF MICROPEN WRITING

3.1 Introduction and objectives

This chapter describes the study on the Micropen™ deposition of lines using polymeric solutions (PMMA solutions) as a model system. This chapter is organized into three sections. The first section is an introduction to the basic theory of rheology, which is helpful for analyzing rheological properties of the PMMA solutions. The second section is the experimental procedures, which include the preparation of PMMA solutions with different concentrations and the deposition of PMMA lines by Micropen™. The third section is the discussion of the rheological properties of PMMA solutions and their effects on the deposition conditions.

3.1.1 The basic theory of rheology

3.1.1.1 Types of flow behavior

Rheology is the science of deformation and flow of matter. There are many types of flow behavior, shown in Fig. 3.1[26]. The simplest type of flow of matter is known as Newtonian and is characteristic of simple liquids, such as water, oils and alcohols[27]. Shear stress is required to initiate and maintain a laminar flow in a simple liquid. If the shear stress (σ) is linearly dependent on the velocity gradient ($-dv/dy$) of the layers of fluid, the liquid is said to be Newtonian[26].

$$\sigma = \eta(-dv/dy) \tag{3.1-a}$$

or $$\sigma = \eta\dot{\gamma} \tag{3.1-b}$$

where $\dot{\gamma}$ is the shear rate. The constant of proportionality is the coefficient of viscosity (η), which indicates the resistance to flow due to internal friction between the molecules of the liquid.

The conditions for Newtonian flow are not satisfied for more complex materials such as lubricating greases or facial creams[26]. For example, grease will not flow unless some threshold pressure is exerted upon it. This threshold stress below which flow does not occur is called the yield stress value of the fluid. When the yield stress value has been exceeded, the difference between the excess pressure and the pressure at the yield stress value will be proportional to the flow rate. This type of material is known as a Bingham plastic. The yield value is a result of the strength of bonds in the gel structure of the grease: once those bonds are sheared, the grease flows more readily.

Two other important types of flow behaviors are known as shear thinning (or pseudoplastic) and shear thickening (or dilatant)[26]. In the case of shear thinning, the stress required to increase the shear rate diminishes with increasing shear rate. Generally, in liquids or solutions containing larger molecules and in suspensions containing non-attracting anisometric particles, laminar flow may orient the molecules or particles. Such orientation reduces the resistance to shear and therefore shear thinning. Shear thickening is an example of dilatancy, or expansion of the system under flow. One simple reason for that is that the particles can glide past each other at low flow rates, but strongly interfere with one another at higher flow rates. Therefore, it is expected that faster-flowing particles cause an expansion effect of the fluid. Coating dispersions, moderately concentrated suspension containing larger agglomerates, and concentrated deflocculated slurries may have shear thickening behavior[27].

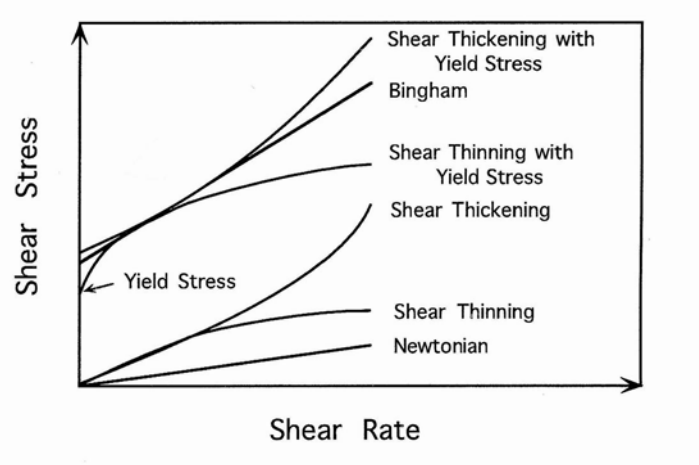

Fig. 3.1 Variations of shear stress with shear rate for different types of flow behavior[26].

Both shear thinning and shear thickening phenomena can be described by an empirical power law equation[26],

$$\sigma = K\dot{\gamma}^{n} \tag{3.2-a}$$

or $$\eta_a = K\dot{\gamma}^{n-1} \tag{3.2-b}$$

where K is the consistency index, and η_a is the apparent viscosity (also called "viscosity" or "shear viscosity"). The value of n indicates the departure from Newtonian behavior. If n<1, it is shear thinning; if n>1, it is shear thickening. Power law materials have no yield point[26].

3.1.1.2 Viscoelastic materials

Very few materials are perfectly elastic or viscous; the majority of samples exhibit both properties in various degrees. Materials having both viscous and elastic properties are termed viscoelastic materials[28]. Two or more parameters are required to characterize the flow of viscoelastic materials. Elasticity implies memory. A viscoelastic

material poured onto a flat surface will not smoothly cover the surface and will retain part of its shape before pouring. It is possible to perform a non-destructive test which measures both the viscous and elastic behavior of a sample simultaneously using an oscillatory rheometer. When conducting an oscillatory test, a sinusoidal stress wave is applied to the sample via a suitable measuring geometry, and the resulting strain wave is then measured. Oscillation test can be used to characterize the viscoelastic behavior and to determine structural changes occurring in the sample[28].

Hookean Solid—since stress is directly proportional to strain for a Hookean solid, a sinusoidal stress wave produces a sinusoidal strain wave perfectly in phase.

$$\sigma = A\sin\omega t \tag{3.3-a}$$

$$\varepsilon = B\sin\omega t \tag{3.3-b}$$

where ε is strain. The strain wave is in phase but may be of different amplitude.

Newtonian Liquid—since stress is directly proportional to strain rate for a Newtonian liquid, a sinusoidal stress wave produces a sinusoidal strain wave which is exactly 90º out of phase. When the stress is at maximum, the strain is at a minimum.

$$\sigma = A\sin\omega t \tag{3.4-a}$$

$$\varepsilon = -B\cos\omega t \tag{3.4-b}$$

A viscoelastic sample subjected to a sinusoidal stress wave produces a sinusoidal strain wave which is out of phase by more than 0º but less than 90º. The phase angle is 0º for an ideal elastic material (all energy stored in the material), 90º for an ideal viscous material (all energy dissipated as heat), and between 0 and 90º for a viscoelastic material. The closer the angle is to 90º, the closer the material is to a viscous material.

The shear modulus (resulting from changing strain) is the ratio of the shear stress to the shear strain. The rheological results can be presented in terms of "complex" shear modulus, G^*,

$$G^* = G' + iG'' \tag{3.5}$$

where *G'* and *G"* are referred to as "storage" (or elastic) modulus and "loss" (or viscous) modulus, respectively[29]. The balance between energy loss and storage is quantified by tanδ:

$$\tan\delta = G''/G' \tag{3.6}$$

3.1.2 Objectives

In Micropen^{TM} direct-write technique, it is important to study the rheological behavior of writing materials. Basically, Micropen^{TM} writing is an extrusional method, and the flow behavior of materials through a pen tip is one of the critical factors determining the writing conditions. Therefore, it is essential to gather information about the materials' rheological behavior, in order to better control writing quality for the Micropen^{TM} technique.

As mentioned in chapter 1, Dimos and Lewis' group have utilized Micropen^{TM} for the deposition of electronic components[20-23]. However, they have not explored the influence of material rheology on the line dimension and writing parameters. In addition, the pastes in their work were ceramic pastes with relatively higher viscosities (e.g. 25-300 Pa·s). No work has been done so far on Micropen^{TM} using polymer solutions with relatively lower viscosities, which is interesting to be explored.

Therefore, the objective of this chapter is to study the effects of material rheology on the line dimension and writing parameters using Micropen^{TM}. Poly(methyl methacrylate) (PMMA) polymeric solutions with different concentrations were used in this work as a model material system. The goal of the following study is to gain a basic understanding of the Micropen^{TM} operation for materials with different viscosities, and further to provide valuable feedback for optimizing writing parameters for any materials with comparable rheological properties.

3.2 Experimental Procedures

3.2.1 Sample preparation

Poly(methyl methacrylate) (PMMA) solutions were used as a model system in this study. The average molecular weight ($\bar{M}_w$) of PMMA in powder form is 120,000 g/mol, with 1.188 g/ml density, and a refractive index of 1.4900. The solvent used was N, N-dimethyl acetamide (DMAc), which has a relatively high boiling point of 165 °C. Both PMMA and DMAc were supplied by Aldrich, and were used as received.

PMMA powder was dissolved in the DMAc solvent to obtain solutions with seven concentrations of 10, 15, 20, 25, 30, 35 and 40 wt%. PMMA powder was added gradually into the solvent, and the solutions were prepared in closed glass vials (40 ml) under continuous magnetic stirring. The solutions were heated between 40-60 ºC to help dissolve PMMA powder. After dissolving, heating was stopped and the solution was continued to stir overnight at room temperature. Then the PMMA solutions were stored for 1 day to eliminate residual bubbles generated during stirring before rheological measurements and the Micropen^{TM} deposition.

3.2.2 Rheological measurements of the PMMA solutions

Rheological measurements were performed using an AR1000-N controlled stress rheometer (TA instruments, shown in Fig. 3.2), fitted with a concentric cylinder with conical end made from steel. All measurements were conducted at 20 ºC.

Several steps were carefully taken before measurement to ensure solution consistency and equilibration condition:

(1) Waited 20 min after pouring the solutions into the container;

(2) Waited 1 min for initial temperature of 20 ºC;

(3) Waited 2 min for "performing pre-shear" at angular velocity of 20 rad/sec;

(4) Waited 5 min for "performing equilibration".

Following two types of tests were carried out on the PMMA solutions:

(1) Steady state flow test: viscosity and shear stress as a function of shear rate in the range of 1-200 s^{-1};

(2) Stress sweep test: elastic (or storage) modulus (G'), viscous (or loss) modulus (G") and loss angle ($\tan\delta = G''/G'$), as a function of oscillation stress. When conducting an oscillatory test, a sinusoidal stress wave is applied to the sample with increasing the amplitude of the stress. The resulting strain wave is then measured[28]. In this test, the oscillation stress was 0.1-500 Pa, at a fixed angular frequency of 6.3 rad/sec.

The steady state flow test provides information on samples' viscosity, and the stress sweep test provides information on samples' viscoelasticity.

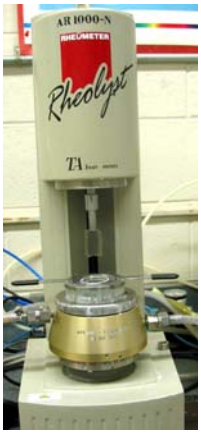

(a)

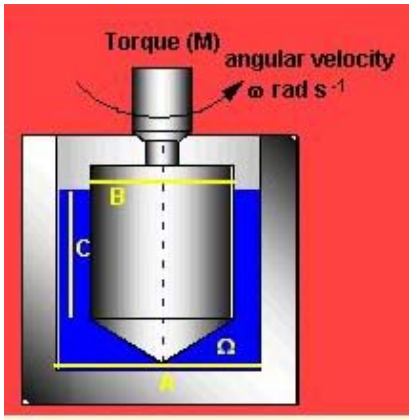

(b)

Fig. 3.2 (a) The AR1000-N controlled stress rheometer and (b) The concentric cylinder.

3.2.3 Deposition and characterization of the PMMA lines

The PMMA solutions with various concentrations were carefully loaded on Micropen^{TM} machine as writing materials. PMMA lines were deposited on glass slides (pre-cleaned by acetone and distilled water), and left in the hood overnight before the profilometric measurement.

In this study, a pen tip with inner diameter of 250 μm was used for the deposition. According to Micropen^{TM} manual, the general procedure of adjusting writing parameters for a new material is as following: first, to choose the values for the pressure exerted on the syringe, "cross section" and "writing speed"; then to set the initial values for the following parameters: LF, WF, BV, SD, MD=0, TV=10,000 mil^3, TH=0.5 mil, LS=10,000; finally, to adjust the following parameters for quality line starts (LF, TH, TV, WF, LF, BV). The optimized writing parameters for the PMMA solutions with different viscosities (at shear rate=20 s^{-1}) are listed in Table 2.1. "Cross section" (CS) of 20 mil^2 and "writing speed" (WS) of 200 mil/s were chosen for all the samples. The pressure exerted on the syringe for the 40 wt% PMMA solution was 30 psi, and 10 psi for the rest samples.

Table 3.1 The writing parameters for the PMMA solutions.

wt %	η	CS (mil^2)	WS (mil/s)	TH (mil)	WF (mg)	LF (mg)	LS (mil^3/s)	TV/TS (mil^3)/(mil^3/s)	BV/BS (mil^3)/(mil^3/s)
10	0.007	20	200	0.02	10	25	500	0/500	2000/20000
15	0.02	20	200	0.02	25	50	500	2000/5000	0/500
20	0.08	20	200	0.02	50	50	2000	0/500	2000/20000
25	0.2	20	200	0.06	100	50	4000	4000/40000	4000/80000
30	2	20	200	0.15	75	50	5000	5000/50000	0/500
35	6	20	200	0.15	50	50	5000	8000/80000	0/500
40	28	20	200	0.25	50	50	5000	40000/500000	0/500

Other parameters: Start Delay, End Delay, Motion Delay=0, Rev. Volume=1500 mil^3.

For one PMMA solution, ten lines (~24 mm long) were deposited on glass slides with the optimized writing parameters, and five of them were chosen as the representative lines. Then, the line dimensions (line width and height) of ten different spots along each representative line (from line start to end) were measured by a profilometer (TENCOR Instruments, alpha-step 200). The value of "Line width × line height" on each spot was simply calculated from the values of line width and line height.

Field emission scanning electron microscope (FESEM) was used to observe the cross section of a representative line deposited on glass slides using the 40 wt% PMMA solution. The FESEM sample was gold sputtered for 2 min.

3.3 Results and Discussion

3.3.1 Choice of the calibration materials

Poly(methyl methacrylate) (PMMA) solutions were used as a model material system in our Micropen^{TM} calibration study. PMMA is a widely used polymer which is cheap and easy to process. The use of polymer solutions provides the advantage of modulating solution viscosity simply by changing the ratio of solute to solvent. In addition, the main advantages of using DMAc, a solvent with a relatively high boiling point (~165°C) are:

(a) Low volatility to ensure little solvent evaporation during sample preparation and rheological measurements;

(b) Prevention of pen tip clogging in the Micropen^{TM} deposition.

3.3.2 Rheological properties of the PMMA solutions

3.3.2.1 Steady state flow test

Fig. 3.3 (a) depicts the shear stress as a function of shear rate for the seven PMMA solutions, along with distilled water as a reference. The viscosity as a function of shear rate are plotted in Fig. 3.3 (b) and (c). For the 40 wt% solution, no data could be measured when shear rates were larger than 40 s^{-1} due to the instrument's limitations. Rheometers using other geometries (such as cone and plate) may be used for higher-viscosity samples, but were not available to us.

It is clear that the PMMA solutions with lower concentrations (<35 wt%) and distilled water showed nearly linear relation between shear stress and shear rate ($\sigma = \eta\dot{\gamma}$), exhibiting Newtonian behavior. The 35 and 40 wt% PMMA solutions began to show a small degree of shear thinning behavior. These findings are consistent with previous

results in the literature[27]. Typically if a polymer solution is dilute, it exhibits Newtonian flow. If concentrated, it may form a gel structure and behaviors as a Bingham plastic. In between is a region where the solution does not have a yield value, but exhibits shear thinning behavior. One explanation of this phenomenon is that the polymer particles are random at low flow rates but tend to orient in the direction of flow as the rate increases and thereby offer less resistance[27].

Fig. 3.4 shows the viscosity of PMMA solutions increased with solution concentrations (wt%), and could be fitted using an exponential model. It was found that at a shear rate of 20 s^{-1}, the viscosities for the 10, 15, 20, 25, 30, 35 and 40 wt% PMMA solutions were 0.007, 0.02, 0.08, 0.2, 1.9, 6.4 and 28 Pa·s, respectively. This trend has also been observed for the ethyl cellulose solutions[22], and can be used to estimate the viscosities of PMMA solutions with higher concentrations (> 40 wt%).

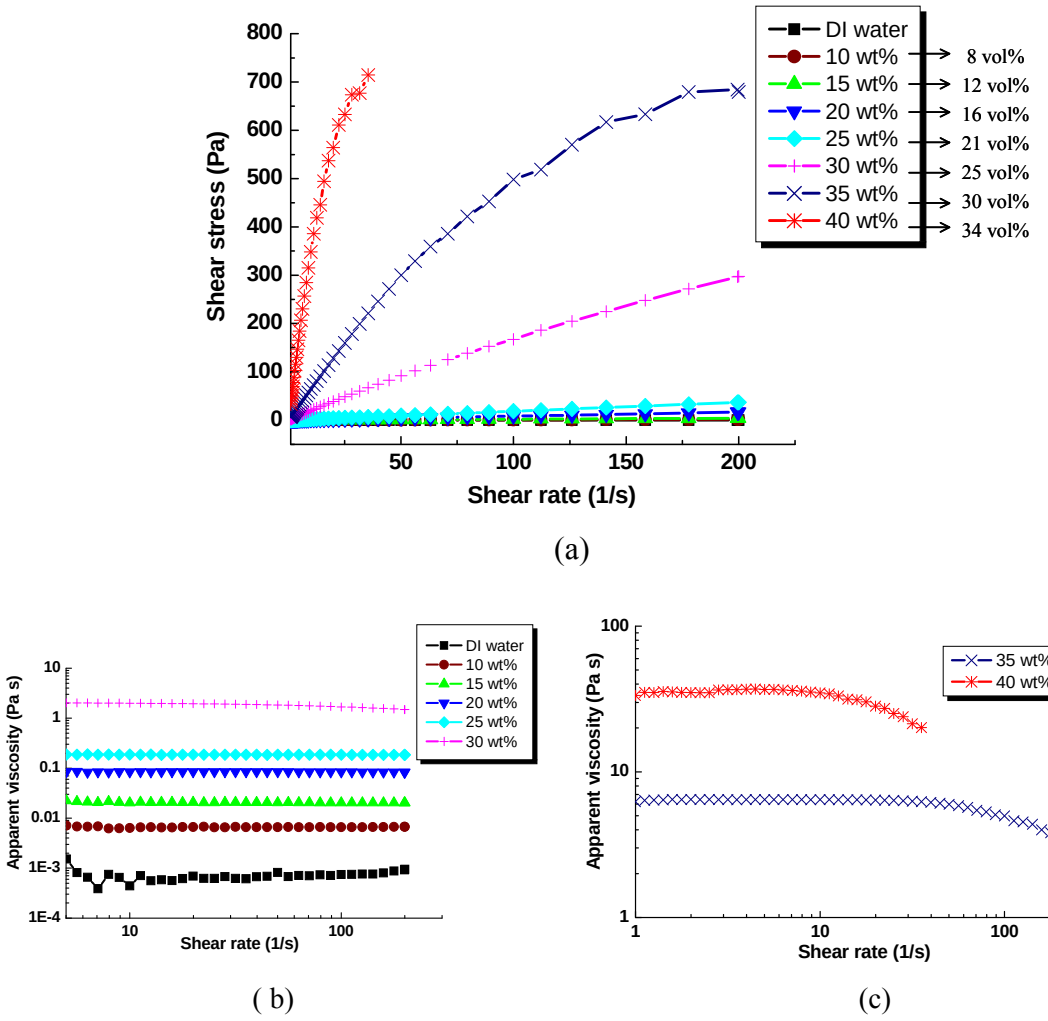

Fig. 3.3 (a) Shear stress as a function of shear rate and (b) (c) viscosity as a function of shear rate for all the samples.

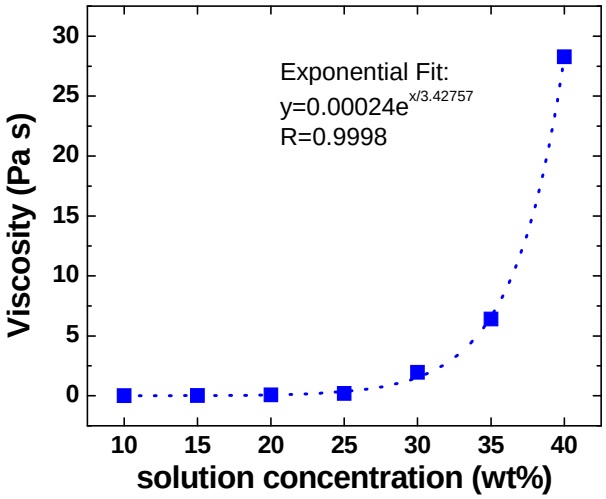

Fig. 3.4 Viscosity of the PMMA solutions as a function of solution concentration.

3.3.2.2 Stress sweep test

Fig. 3.5 (a) and (b) show the stress sweep plots for the 35 and 40 wt% PMMA solutions, respectively. Those plots are not shown for the other samples because of their low elastic modulus (G'<0), indicating that the PMMA solutions with lower concentrations and distilled water did not show obvious elastic properties.

The figures provide several results:

(1) The values of G' and G" for 30, 40 wt% solutions were almost constant in the oscillation stress range (0.1-500 Pa), indicating no structural changes with increasing oscillation stress.

(2) The values of G" were higher than G' for both the solutions, showing the two solutions were more viscous than elastic character.

(3) The G' value for the 40% solution (~35 Pa) was higher than that for the 30 wt% solution (~1 Pa), indicating the elasticity of PMMA solution increased with increasing PMMA concentration.

(4) The value of delta, $\delta = \tan^{-1}(G''/G')$, was ~ 89º for the 35 wt% solution, while ~ 81º for the 40 wt% solution. This is consistent with the knowledge that the closer the angle to 90º, the less the elasticity of the material. Therefore, the 40 wt% solution was more elastic than the 35 wt% solution.

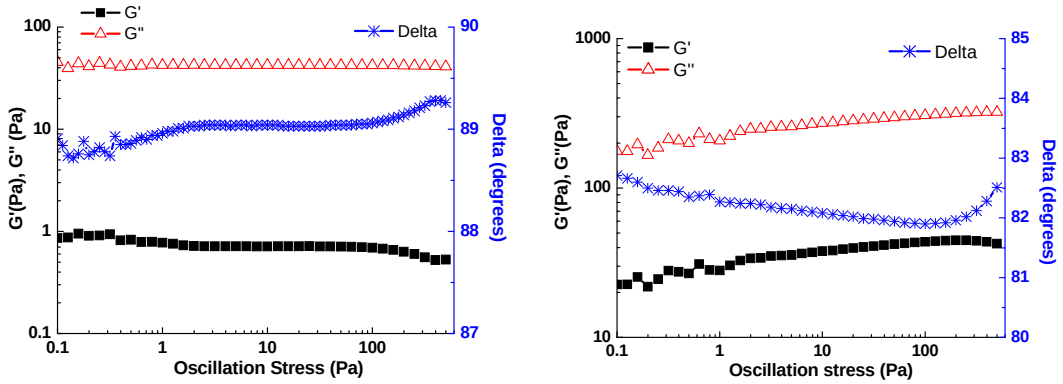

Fig. 3.5 Stress sweep tests for (a) the 35 wt% and (b) 40 wt% PMMA solutions.

In summary, based on the data above, following basic knowledge about the rheological properties of the PMMA solutions can be concluded:

(1) The PMMA solutions with lower concentrations (<35 wt%) exhibited Newtonian behavior, and had much lower viscosities (0.007-2 Pa·s). The PMMA solutions with higher concentrations (35, 40 wt%) began to show a small degree of shear thinning, and had higher viscosities (6-28 Pa·s). The lower viscosity values and smaller degree of shear thinning indicate that the PMMA solutions are more suitable for writing smooth filled regions (e.g. films) than writing high definition patterns (e.g. lines).

(2) The PMMA solution viscosity increased exponentially with solution concentration (wt%).

(3) The 35 and 40 wt% solutions showed viscoelastic properties, which is indicative of better shape retention after deposition than the lower concentration solutions.

3.3.3 Effects of solution concentration on the line dimension

The averaged values of the deposited line dimension using the seven PMMA solutions are plotted in Fig. 3.6. The error bars give the standard deviations for each of the values. The variations of line width for the 20, 25, 30, 35 and 40% solutions were about 4%, 4%, 3%, 1% and 1%, respectively. The variations of line height for the these solutions were about 8%, 8%, 4%, 2% and 2%, respectively. It was found that in general, the line width decreased and line height increased with increasing the solution concentration. The better line resolution (e.g. narrow line width) using the 40 wt% PMMA solution should be due to its highest viscosity (η~28 Pa·s) and elasticity (G'~35 Pa) compared to the rest solutions. This result is as expected that a solution with higher viscosity spreads less than a solution with lower viscosity. However, the 10 and 15 wt% solutions did not fit in this general trend. The viscosities of these two solutions were too low to allow accurate deposition control.

Fig. 3.7 (a)-(c) also show the linear fitting ($y = A + Bx$) for the line width, line height and line width×line height for the five PMMA solutions (20-40 wt%), respectively. The data for the 10 and 15wt% solutions were also neglected due to their large deviation from the general trend. As can be seen, nearly linear relations were observed for the PMMA solutions (20-40 wt%). In addition, as expected, a better linearity was observed in Fig. 3.7 (c), because the value of "line width×line height" is approximately the amount of material deposited, which should be proportional to the concentration of PMMA solution. Therefore, the linear correlations in Fig. 3.7 (a)-(c) show that the Micropen^{TM} technique enables the deposition of lines with precisely controlled line width and height for solutions with different concentrations.

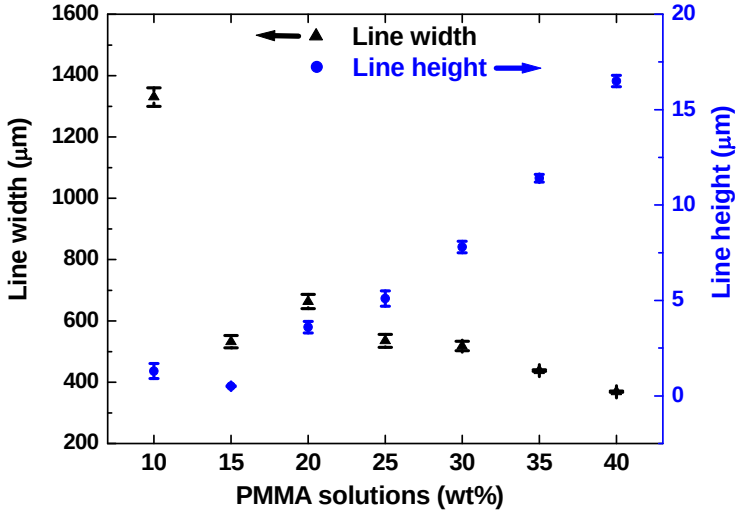

Fig. 3.6 The variations of line width and line height for the seven PMMA solutions.

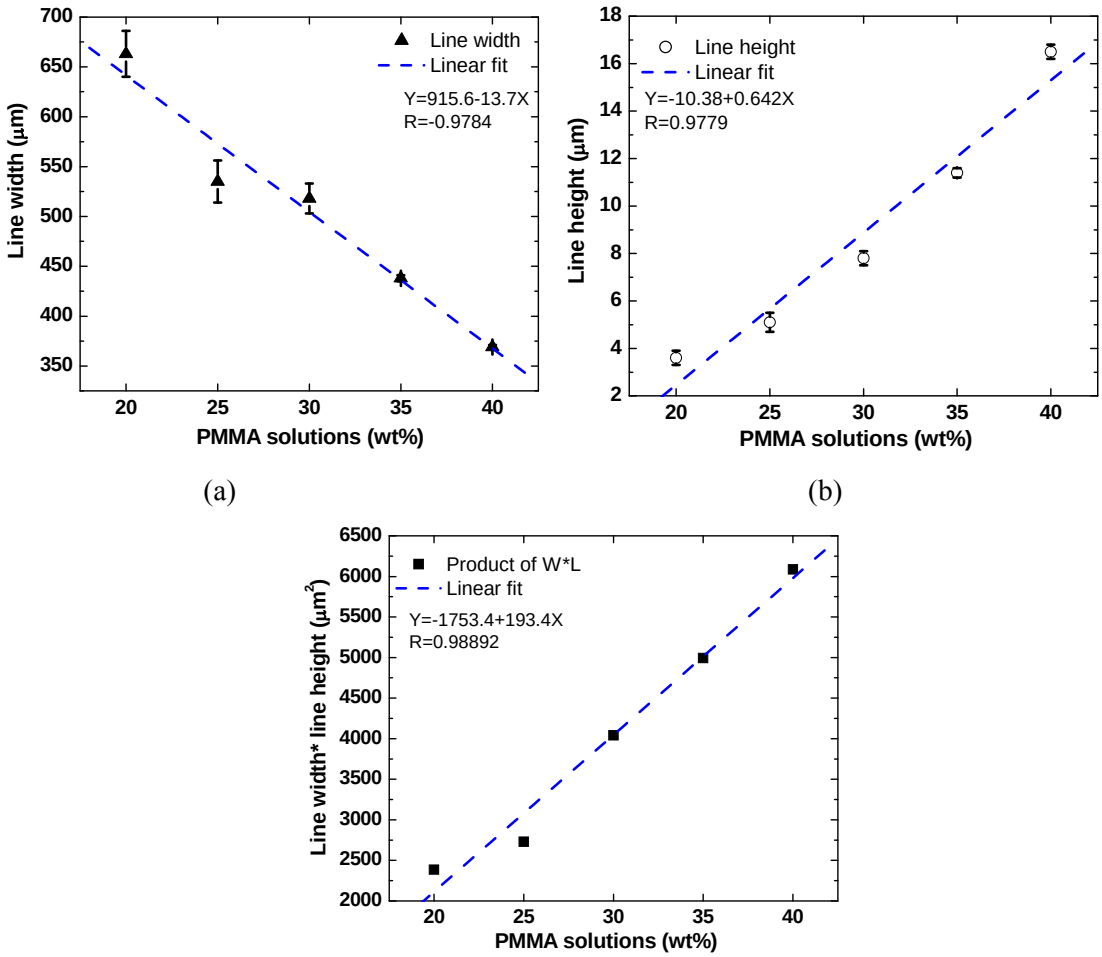

Fig. 3.7 Linear fitting for (a) line width, (b) line height and (c) line width×line height for the five PMMA solutions.

3.3.4 The variations of line dimension along a deposited line

Fig. 3.8 (a) and (b) show the averaged values of line width and height of ten chosen positions along a deposited line for the five PMMA solutions, respectively. The error bars give the standard deviations for each of the values.

The plots neglected the data for the 10 and 15 wt% solutions due to the same reason as mentioned in section 3.3.3. Following conclusions can be drawn:

(1) It showed that although the Micropen^{TM} writing parameters were carefully adjusted, it was still challenging to get high quality line starts and ends.

(2) It is noted that if neglecting the line starts and ends ("transient" region), the middle of each line ("stationary" region) exhibited relatively good consistency, for both the Newtonian and shear thinning solutions. In the middle region of each line, the variations for the line width and line height were about 1-3% and 2-8%, respectively.

(3) Based on our experiments, it was found that for the deposition of lines using a material with higher viscosity, larger TH ("trigger height"), larger TV/TS ("termination volume"/"termination speed") and lower BV/BS ("burst volume"/"burst speed") were preferred to obtain high quality line starts and ends (as listed in Table 2.1). For the lower-viscosity solutions with 10, 15, 20 and 25 wt% (η<0.5 Pa·s), more materials came out as writing continued. Increasing BV/BS values could keep the amount of material more consistent during writing in some degree.

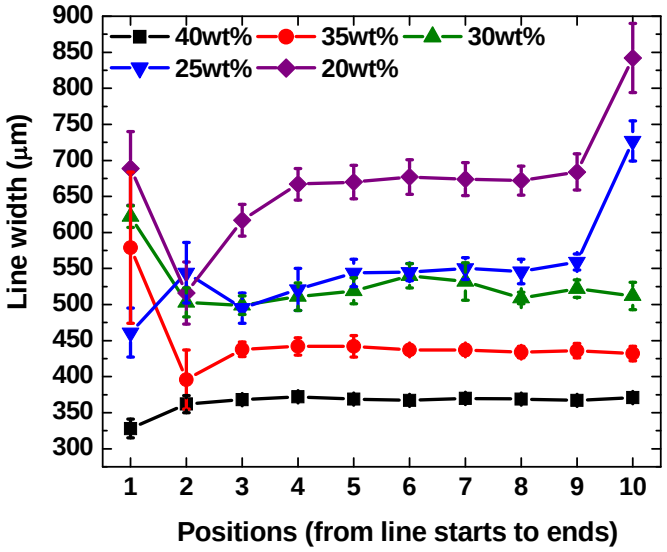

(a)

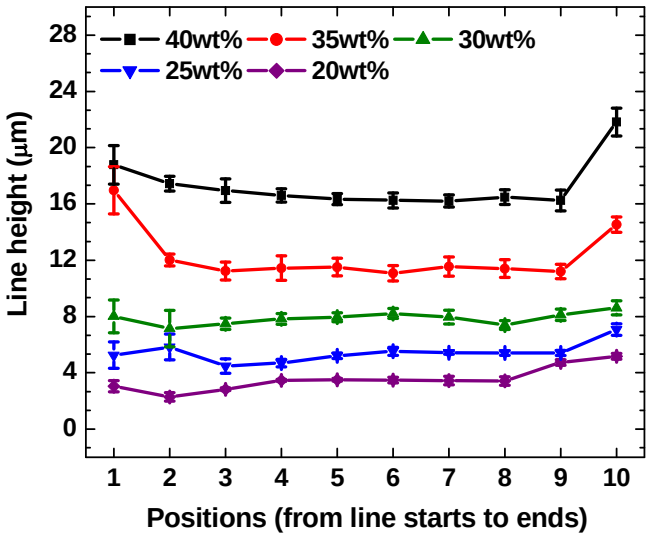

(b)

Fig. 3.8 The variations of (a) line width and (b) line height along a deposited line for the five PMMA solutions.

3.3.5 FESEM image of a representative sample

Fig. 3.9 shows a representative line deposited using the 40 wt% PMMA solution. The values of line width and line height were about 330 μm and 18 μm, respectively, close to that measured by the profilometer. This figure reveals that the cross section of the line was not rectangular, and the aspect ratio of line height to line width was small (~ 1:18). In order to get higher line height and aspect ratio, smaller pen tip, and solutions with higher viscosity and higher degree of shear thinning are desirable.

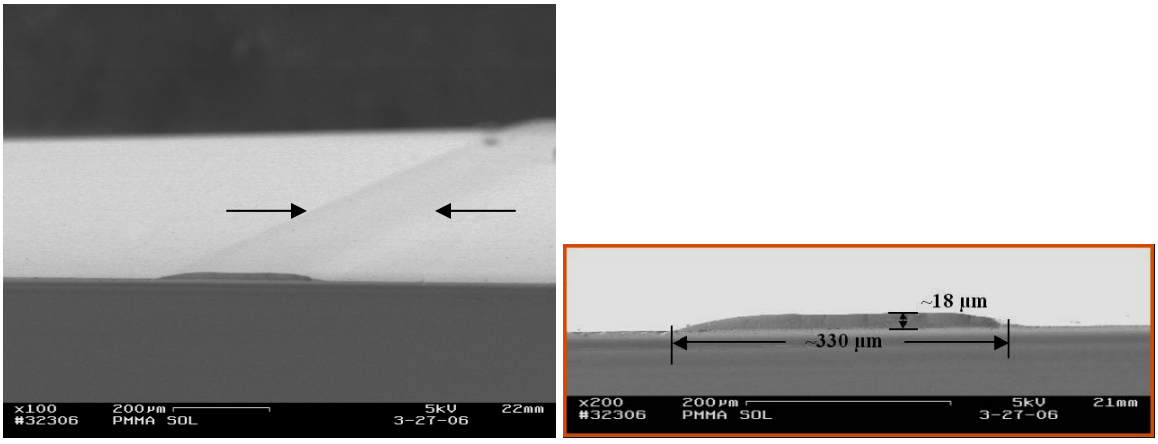

(a) (b)

Fig. 3.9 FESEM image of a deposited line using the 40 wt% PMMA solution (a) at lower and (b) at higher magnification.

3.4 Summary

In summary, PMMA polymeric solutions were developed as a model material system to study the effects of rheological properties on the Micropen™ writing conditions. The model PMMA solutions had viscosities in the range of 0.007-28 Pa·s (at shear rate=$20s^{-1}$), and exhibited Newtonian behavior at lower concentrations (<35 wt%), while exhibited a small degree of shear thinning behavior and elasticity (G'~35 Pa) at higher concentrations (35, 40 wt%).

This study demonstrated the feasibility of depositing the PMMA solutions with different viscosities using the Micropen™ technique. (1) Line writing was able to be accomplished for both the Newtonian and shear thinning-behavior PMMA solutions. (2) By increasing the solution concentration, the general tendency is that the line width decreased and line height increased. Thus, the better line resolution was obtained when using the 40 wt% PMMA solution, which should be due to its relatively higher viscosity (η=28 Pa·s) and elasticity. (3) Nearly linear correlations were observed for the line width, line height, and line width×line height as a function of the solution concentration. It indicates a valuable advantage of the Micropen™, to enable deposition of lines with precisely controlled dimension and the amount of materials dispensed. (4) It was challenging to obtain high quality line starts and ends, but the middle of lines exhibited relatively good consistency for the PMMA solutions with 20-40 wt%.

CHAPTER4 SYNTHESIS OF PMMA/SiO_2 HYBRID MONOLITHS BY SOL-GEL PROCESS AND DIRECT-WRITE OF PMMA/SiO_2 LINES

4.1 Introduction and objectives

This chapter describes the synthesis of the organic/inorganic hybrid materials (PMMA/SiO_2) and the Micropen^{TM} deposition of lines using the optimum composition. This chapter is organized into three sections. The first section is an introduction to the PMMA/SiO_2 hybrid materials prepared by a sol-gel process. The second section is the experimental procedures including the synthesis and characterization of the hybrids, and the deposition of PMMA/SiO_2 lines. The last section is the discussion of the experimental results.

4.1.1 PMMA/SiO_2 hybrids prepared by the sol-gel process

These types of organic/inorganic hybrid materials are a new class of composite materials composed of an intimate mixture of the organic and/or inorganic components a few nanometers in size. These novel materials combine the excellent properties of both organic (e.g. flexibility, toughness and formability) and inorganic components (e.g. mechanical, optical properties and high thermal stability) which offer new possibility for advanced applications. These hybrids are versatile in the composition, processing and properties. They have a variety of applications in optics, mechanics, electronics, energy, environment, biology and medicine, such as membranes, separation devices, functional smart coating, fuel and solar cells, catalysts and sensors[30].

The organic/inorganic hybrids have to be prepared at mild conditions (i.e. low temperature), due to the relative low thermal stability of organic components. The possibility of a hybrid sol-gel route has been successfully explored for the synthesis of hybrid materials since 1985, starting with Schmidt[31]. This field has been developed quickly because it provides an approach to design new materials and devices with outstanding properties. Compared to the traditional sol-gel (i.e. pure inorganic sol-gel reactions), some advantages of the hybrid sol-gel are the following[32]:

(a) The organic groups can modify the inorganic backbones by reducing the connectivity of the gel network, allowing thick film deposition;

(b) Homogeneous mixing of organic and inorganic components at the molecular level makes it possible to tailor the hybrids' properties by varying the compositions;

(c) The low temperatures for densification (~100-200 ^{o}C) of metal oxides in organic solvents opens the possibility of adding organic species to the sol-gel solution, such as organic dyes and biological species;

(d) It is possible to synthesize materials with controlled porosity, which can be impregnated by optically active dyes, and this open porosity makes these molecules accessible to other reagents used in chemical sensors.

Hybrid materials can be simply divided into two classes taking into account the type of bonds between the organic and inorganic components[33]:

(1) Class I corresponds to the hybrid materials in which organic and inorganic components are connected by weak interactions, such as hydrogen bonding, electrostatic attraction or van der Waals forces. In this group, organic components are simply "embedded" in inorganic backbones.

(2) Class II corresponds to the hybrids in which the two components are connected by strong interactions, such as covalent, or ionic bonds. In this group, organic components are "grafted" in the inorganic backbones. The preparation is generally made by the sol-gel approach of using alkoxysilyl-containing organic precursors or coupling agents.

One of the widely studied hybrid systems is poly(methyl methacrylate) (PMMA)/SiO_2, because of the commercial importance of PMMA and SiO_2. In recent years, this system has attracted special interest as matrices for rare earth ions and organic dyes in optical devices, due to the low optical absorption, refractive index tailorability, simple synthesis and low cost[34,35]. Recent remarkable reports on PMMA/SiO_2 hybrids were published on the synthesis [36 , 37] , mechanical properties [38 , 39] and thermal stabilities [40 , 41] . However, less information is available on their optical properties, especially in the near infrared region (800-2000 nm). In addition, most work on PMMA/SiO_2 is based on the hybrids where the organic phase is covalently bonded to the inorganic phase. Only a few researchers have studied PMMA/SiO_2 hybrids which do not contain covalent bonding. Although class II hybrids were found to have better optical and mechanical properties than class I hybrids[38], class I hybrids are easier to prepare, and are also homogenous hybrids with relatively good mechanical properties and optical transparency[42]. For example, Landry found that homogenous, transparent PMMA/SiO_2 composites could be formed under acidic conditions, with the result of improved mechanical properties and increased solvent resistance compared to pure PMMA[43]. Klein showed by infiltrating previously formed SiO_2 gels with MMA monomer, the optical transparencies of PMMA/SiO_2 composites were similar to that of porous SiO_2 xerogels

and the composites had reasonable thermal shock resistance[44]. Bian demonstrated that the Eu^{3+} concentration quenching was significantly reduced in the hybrid matrix in comparison to a pure PMMA matrix[45].

Fig. 4.1 shows the schematic of the polymerization of TEOS in the present of PMMA, which was created by Prof. E. Duguet at University of Bordeaux. This process is one of the sol-gel routes for preparing PMMA/SiO_2 hybrids containing hydrogen bonding (Class I), which was adopted in our study.

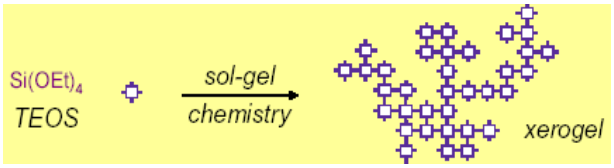

(a) TEOS forms silica xerogel network

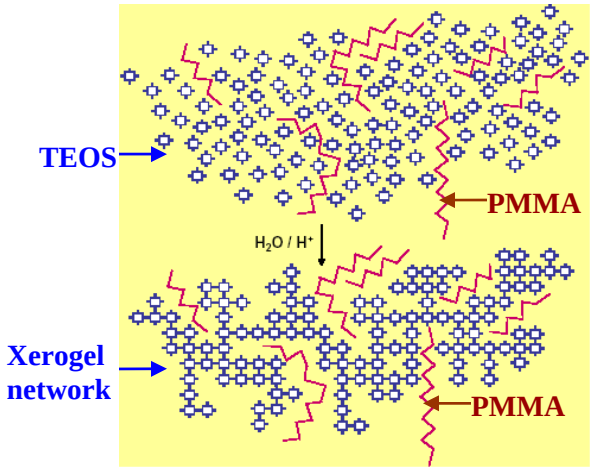

(b) TEOS (blue) forms network in the presence of PMMA polymer (red)

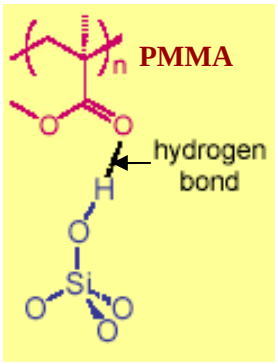

(c) Hydrogen bond forms between the organic and inorganic components

Fig. 4.1 The schematic of the polymerization of TEOS in the present of PMMA (http://www.icmcb-bordeaux.cnrs.fr/duguet/hoim-ed4.pdf).

The organic/inorganic hybrids have been investigated for many applications including optical devices, such as optical amplifiers, loss-less splitters and waveguides. Those structures are generally realized by spin coating (or dip-coating) and standard lithographic process[46,47] (shown in Fig. 4.2). It is very promising to fabricate those devices using direct-write techniques, which can greatly simplify the process, reduce the cost and be more environmentally friendly. The Micropen™ has been successfully applied to develop a wide variety of electronic devices such as capacitors, inductors and conductors, using ceramic powder-loaded materials. However, the feasibility of depositing hybrid sol-gel solutions for optical applications is an unexplored area.

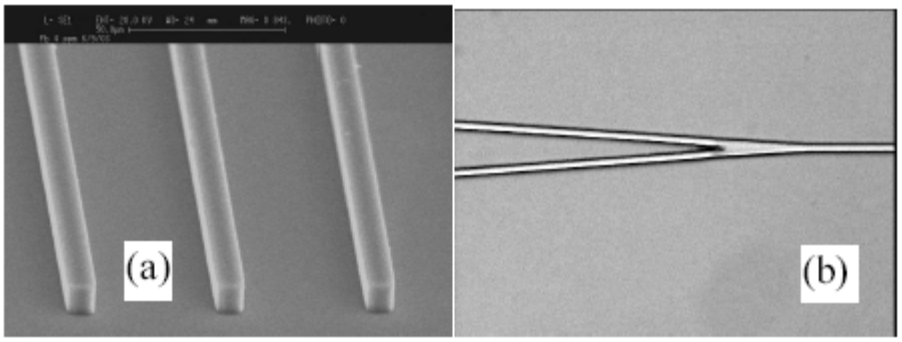

Fig. 4.2 (a) Waveguides and (b) Y-splitter fabricated by spin-coating and lithography process using sol-gel hybrids[46].

4.1.2 Objectives

The objectives of this chapter are:

(1) To synthesize PMMA/SiO_2 hybrid monoliths using a sol-gel approach based on the polymerization of TEOS in the presence of PMMA. Three organic/inorganic ratios will be prepared for the investigation.

(2) To fully characterize the PMMA/SiO_2 hybrid monoliths, including thermal stability, microstructure, as well as optical properties. In addition, energy dispersive spectroscopy (EDS) technique will be applied in this work to study the SiO_2 distribution in the hybrids, to further understand the phase separation and optical properties.

(3) To demonstrate the feasibility of direct writing of PMMA/SiO_2 lines using Micropen^{TM} technique, for potential optical applications.

4.2 Experimental Procedures

4.2.1 Synthesis and characterization of the PMMA/SiO_2 monoliths

In this study, tetraethoxysilane (TEOS, $Si(OCH_2CH_3)_4$) was used as the inorganic precursor, poly(methyl methacrylate), PMMA, $[-CH_2-C(CH_3)(COOCH_3)-]_n$ in powder form as the organic precursor, tetrahydrofuran (THF, C_4H_8O) as the solvent (boiling point ≈ 66 ºC), and hydrochloric acid (HCl) as the catalyst for hydrolysis and condensation of TEOS to prepare PMMA/SiO_2 hybrid materials. The average molecular weight ($\bar{M}_w$) of the PMMA used in this work is 120,000 g mol^{-1}, with 1.188 g/ml density, and a refractive index of 1.4900. Three PMMA/TEOS ratios by weight were prepared, namely PMMA/TEOS=80/20, 50/50 and 20/80 (w/w), which referred as P80, P50 and P20, respectively.

Fig. 4.3 is a simple schematic of the synthesis of PMMA/SiO_2 monoliths (in fume hood). Following the work of Silveira[48], PMMA powders were first dissolved in THF at a concentration of 15 wt%. TEOS was added drop by drop to the solution under continuous stirring to give three different organic/inorganic ratios (80/20, 50/50 and 20/80, w/w). A HCl (0.15M) aqueous solution was then slowly added to the solution to provide water and to catalyze the sol-gel reaction. The H_2O: TEOS molar ratio was 4:1. The solution was stirred for 48 h at room temperature and later transferred to closed glass Petri dishes. sAfter storing in hood for 2 weeks for the reactions to take place, the dishes were opened to allow the solvent to slowly evaporate at room temperature for 2 weeks. Relatively longer evaporation time was used to avoid phase separation in the hybrids, because the hybrids became less transparent when evaporated fast.

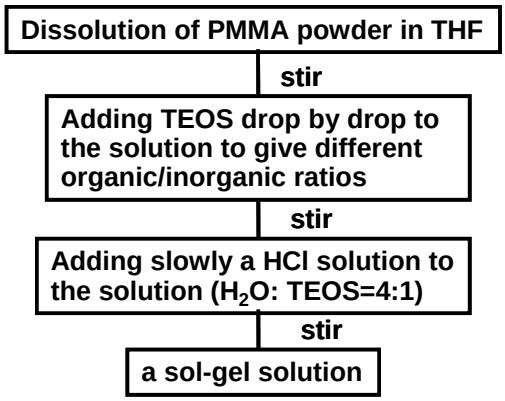

Fig. 4.3 The schematic of the synthesis of PMMA/SiO_2 sol-gel solution.

Thermogravimetric analysis (TGA) of the hybrids was carried out on a Perkin-Elmer TGA7 system from room temperature to 700°C, at a heating rate of 15°C/min in air. The infrared spectra were recorded at room temperature in the range of 400-4000cm^{-1} by using an infrared spectrometer (Thermo Nicolet Avatar 360 FT-IR). The FTIR samples were mixed with KBr, ground, dried at 90ºC overnight, and pressed into pellets.

The morphology and SiO_2 distribution were investigated using a scanning electron microscope (SEM, Amray 1400) equipped with an energy dispersive spectroscopy (EDS). Fracture surfaces were carbon coated before imaging.

Two measurements were carried out to study the hybrids' optical properties. The refractive index (n) of bulk samples was measured according to the Becke line method, using an optical microscope (Olympus, BH2 Japan). A small piece of a sample was immersed into oil with a known refractive index (n), and a bright line (Becke line) was formed on the sample boundary, which moved into the medium having a higher index[49]. The absorption spectra were recorded over the wavelength range 400-2000 nm by the UV/Vis/NIR spectrophotometer (Perkin-Elmer Lambda 9). No measurements could be made on P20 since it was opaque.

4.2.2 Deposition and characterization of the PMMA/SiO_2 lines

The sol-gel solution of P80 (PMMA/TEOS=80/20, w/w) was chosen for the Micropen™ deposition of line patterns. A solvent of N, N-dimethyl acetamide (DMAc, $CH_3 - CO - N - (CH_3)_2$) was used, instead of THF which was used for the preparation of P80 monoliths. The P80 sol-gel solution was put in an oven at ~85ºC for 7 h before the deposition, with the purpose of increasing the solution's viscosity.

In this study, a pen tip with inner diameter of 200 μm was used. The writing parameters were listed in Table 4.1. The cross section of deposited lines on glass slides were examined by a scanning electron microscope (SEM, Amray 1400).

Table 4.1 The Micropen™ parameters for the direct-write of PMMA/SiO_2 lines (using a 200-μm pen tip).

Cross section (mil^2)	Writing speed (mil/s)	Writing force (mg)	Trigger height (mil)	Lift force (mg)	Lift speed (mil^3/s)	Term volume (mil^3)	Term speed (mil^3/s)	Burst volume (mil^3)	Burst speed (mil^3/s)
15	200	60	0.06	100	400	2000	6000	2000	6000

4.3 Results and Discussion

4.3.1 Characterization of the PMMA/SiO_2 hybrid monoliths

4.3.1.1 Transparency

The transparency of the monoliths after evaporation are shown in Fig. 4.4, and listed in Table 4.2. Both P80 and P50 samples were intact, but the P20 sample broke after gelation (refer to section 4.2.1 for the definition of P80, P50 and P20). The P80 sample was transparent up to 0.7 mm thickness, while P50 became more translucent as the thickness gradually increased from 0.1 to 0.8 mm. P20 samples were opaque at all thickness studied.

It is known that optical transparency can be used as an initial criterion for the formation of a homogeneous phase in hybrids[50]. The difference in appearance indicates the different degrees of phase separation for P80, P50 and P20. Our observations showed that increasing TEOS content favored macroscopic phase separation in the PMMA/SiO_2 hybrids. Furthermore, the better transparency for the monoliths P80 and P50 indicated there was strong interfacial reaction between organic and inorganic components.

Table 4.2 Notation, appearance, TGA and refractive index results of the PMMA/SiO_2 samples.

Sample	**P80**	**P50**	**P20**
PMMA: TEOS (wt%)	80: 20	50: 50	20: 80
Transparency	intact, transparent	intact, transparent to translucent	broken, opaque
[(a)]TGA: residue (wt%) at 700ºC	5.7	15.1	43.3
[(b)]Calculated SiO_2 contents	6.7	22.4	53.5
[(c)]Refractive index (+/- 0.002)	1.484-1.486	1.480-1.482	1.474-1.476
[(d)]Refractive index	1.488	1.485	1.477

(a) Experimental results from TGA,

(b) Theoretical results assuming complete conversion of TEOS to SiO_2, according to the reaction: $Si(OC_2H_5)_4 + 2H_2O \rightarrow SiO_2 + 4C_2H_5OH$,

(c) Experimental results measured by the Becke line method,

(d) Theoretical values assuming ξ= " [(a)]Residue (wt%) at 700ºC " from TGA.

Fig. 4.4 The pictures of the three PMMA/SiO_2 hybrids.

4.3.1.2 Thermal and FTIR analysis

TGA curves of pure PMMA and the hybrid monoliths are shown in Fig. 4.5, and the results are listed in Table 4.2. First, the weight percent at 120ºC of the monoliths P80, P50 and P20 were 99.8%, 99.6% and 98.8%, respectively, indicating little water or solvent content left in the hybrids for the TGA measurements. This is due to the fact that these hybrids were left in hood at room temperature for 2 weeks to evaporate water and THF solvent (boiling point ≈ 66 ºC) (refers to section 4.2.1). Therefore, the evaporated samples can be used for the measurements and characterization. Second, the residue at 700 ºC increased with increasing TEOS content, from 6 wt% for P80, to 15 wt% for P50, and to 43 wt% for P20. The residue reflected the SiO_2 content in the hybrids, because essentially only inorganic components are present at 700 ºC. Comparing the experimental and calculated values of residue in TGA data, the similar trend suggested the successful formation of SiO_2 in the monoliths. The lower experimental values are probably due to TEOS evaporation during synthesis, incomplete conversion of TEOS to SiO_2 and residual THF. Third, the main weight loss of the hybrids took place at 270-450 ºC, corresponding to the random scission of PMMA main chains[51]. Furthermore, it was found that all the three hybrid monoliths have higher decomposition temperatures (~295 ºC) than that of pure PMMA (~270 ºC). The slightly improved thermal stability for the hybrids compared to the pure PMMA may be caused by the interactions between the polymer chains and SiO_2, and hydrogen bonding should be the main source of such interactions. Another possible reason could be the entrapping of PMMA chains within the SiO_2, thereby increasing the energy barrier for decomposition of the hybrids[52].

In the infrared spectra (Fig. 4.6), the presence of PMMA was shown by the absorption peaks for C-H at 2950 cm^{-1}, C=O at 1730 cm^{-1}, and C-O at 1149~1242 cm^{-1}, whose intensity increased with increasing PMMA content in the PMMA/SiO_2 hybrid monoliths. A broad band between 3200 and 3700 cm^{-1} was assigned to the hydroxyl groups. In contrast, P20 had the strongest absorption peaks at 1080 cm^{-1}, 950 cm^{-1} and 800 cm^{-1}, associated to the asymmetric stretch vibration of Si-O-Si, Si-OH, and symmetric stretch vibration of Si-O-Si, respectively. The intensity of those peaks increased with increasing TEOS content. The presence of Si-O-Si and Si-OH peaks confirmed the formation of SiO_2 network in the hybrid monoliths. In addition, the residual silanol groups (Si-OH) can play an important role in forming hydrogen bonds with the carbonyl groups (C=O) of PMMA, which suppresses phase separation[53].

4.3.1.3 Microstructures analysis

Fig. 4.7 show the typical SEM images of the fracture surfaces of the PMMA/SiO_2 hybrid monoliths and pure PMMA sample. It shows the morphological evolution of the hybrids with different organic/inorganic ratios. It was found that the morphology transformed from a relatively smooth and homogenous surface (P80), to an interconnected phase (P50), and to a discrete microstructure (P20). The roughness of the fracture surfaces also increased as increasing TEOS content. The FTIR analysis evidenced the possible formation of hydrogen bonding, while the SEM study provided a qualitative measure of miscibility in the hybrids. The smooth surface of P80 indicated more uniform mixing of organic and inorganic components than P50 and P20, resulting in the best optical transparency and lowest absorption (Fig. 4.9). The relatively smooth surface of P80 and P50 indicated a strong interaction between organic and inorganic

components. The morphological variations could be explained by the mechanisms of phase separation proposed by Silveira[48]. The similar relation between phase separation and gelation was also studied on poly(ethylene oxide)/TEOS hybrids[54].

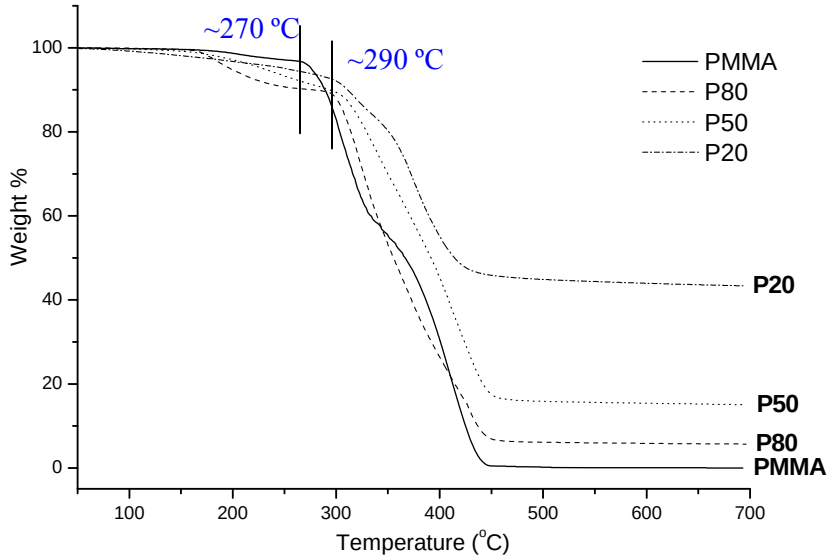

Fig. 4.5 TGA curves of the three PMMA/SiO_2 hybrids and pure PMMA.

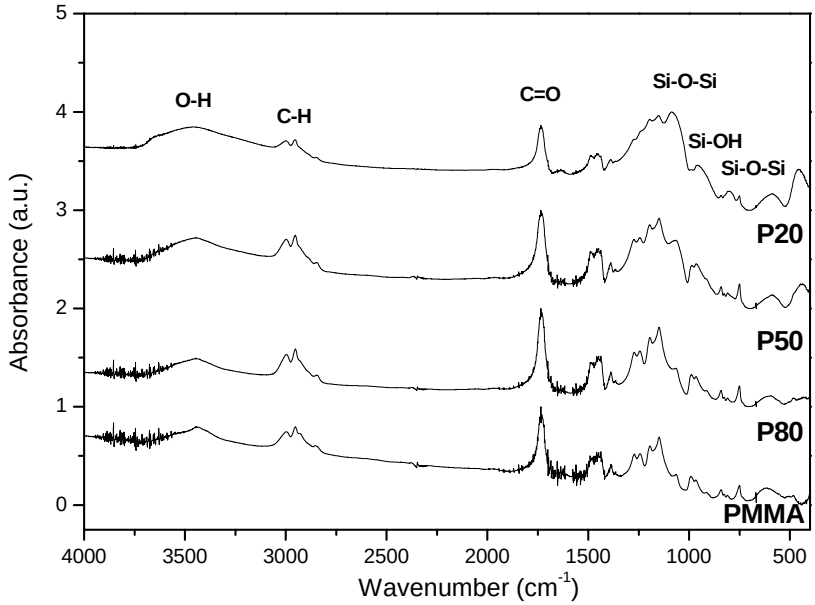

Fig. 4.6 FTIR spectra of the three PMMA/SiO_2 hybrids and pure PMMA.

Fig. 4.8 shows the EDS results, scanned along a horizontal line through the center of the corresponding SEM image shown in Fig. 4.7. Fig. 4.8 (a) gives an example of the spectrum analysis of the three hybrids. As can be seen, the only detected peak was attributed to element Si, confirming the presence of SiO_2 in the three hybrids. Fig. 4.8 (b)-(d) provided a qualitative analysis of the SiO_2 distribution in the hybrids. Based on the least variation of Si concentration in Fig. 4.8 (b), one can conclude that the SiO_2 distribution was most uniform in sample P80. While P20 possessed the biggest variation of SiO_2 concentration as well as the roughest fracture surface in the SEM results. The EDS results clearly revealed that silica distribution in the hybrid monoliths became more uniform with increasing PMMA content, which match quite well with the morphological changes observed in SEM. The homogeneity and phase behavior of hybrids are closely related to the organic/inorganic interfacial interaction[55]. The relative uniform dispersion of SiO_2 in P80 and P50 suggested improved miscibility between PMMA and SiO_2 as compared to P20. P80 exhibited the most uniform SiO_2 distribution, which not only contributed to its best transparency, but also indicated the strong interaction between the organic and inorganic components. The analysis above can be evidenced by FTIR, SEM and absorption results. In contrast, a nonuniform distribution of SiO_2 in the sample P20 was apparent, leading to its opacity caused by the macroscopic phase separation.

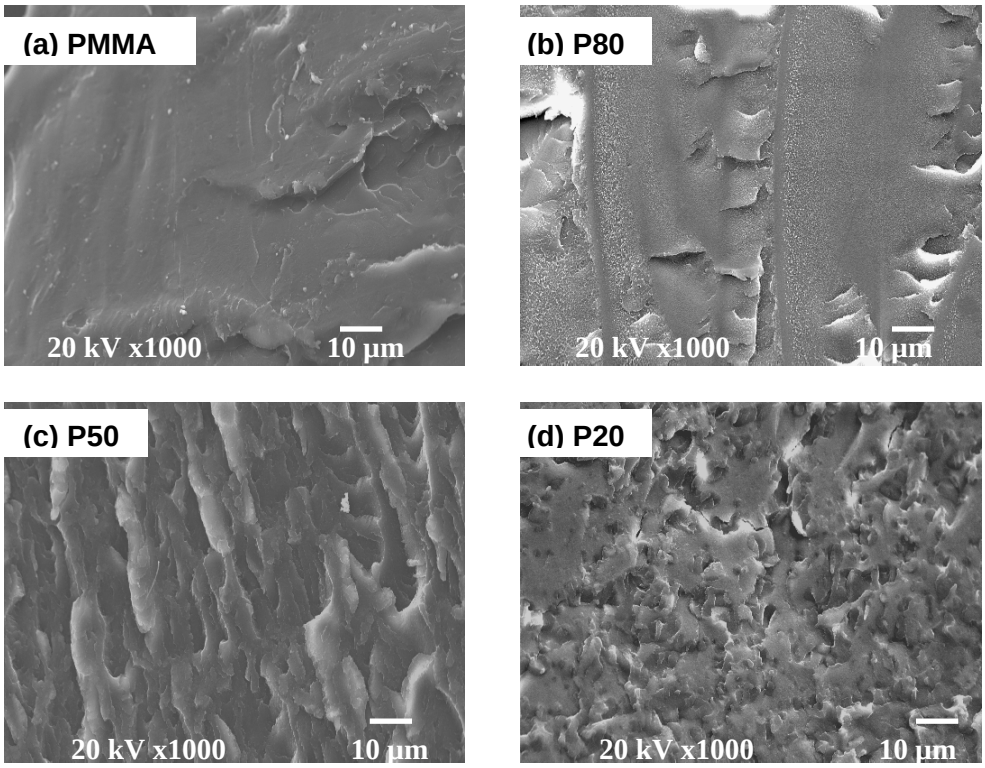

Fig. 4.7 (a)-(d) SEM images of fracture surfaces of the PMMA and PMMA/SiO_2 samples.

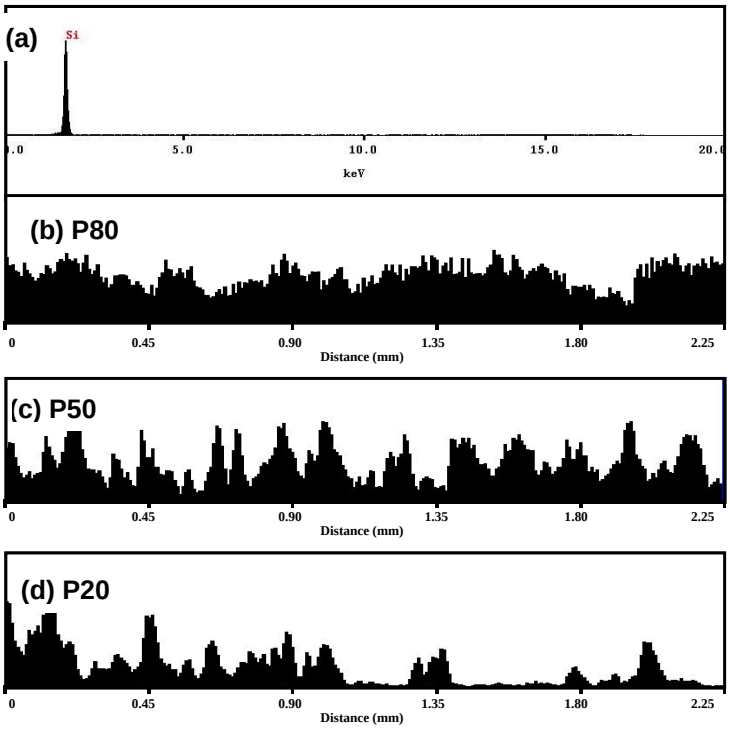

Fig. 4.8 EDS analysis of the PMMA/SiO_2 samples.

4.3.1.4 Optical properties

The refractive index (n) is one of the important factors for optical devices. Table 4.2 (in section 4.3.1.1) shows that with increasing inorganic content, the index decreased from 1.484-1.486 for P80, to 1.480-1.482 for P50, and to 1.474-1.476 for P20. The larger refractive index with increasing TEOS content has been observed in other hybrids[56]. Also listed in Table 4.2 are the theoretical values of n, calculated using a simple mixing rule: $n_{hybrid} = \xi n_{SiO_2} + (1-\xi) n_{PMMA}$, where ξ = the SiO_2 weight fraction in the hybrid. It is noted that the experimental values were close to the values from the mixing rule. This result not only suggested that the index of the hybrid monoliths was tunable by changing organic/inorganic ratio, but also indicated there was little porosity in the hybrids.

Optical transparency is another important characteristic for optical applications. Fig. 4.9 shows the visible and near infrared spectra of two hybrid monoliths and PMMA. The phase separation of the hybrids or the size of the phase separated features results in increased absorption. In detail, the following conclusions can be drawn:

(1) In the visible region (400-800 nm), the absorption coefficient of P80 was as low as that of PMMA. It should be due to the suppression of phase separation by hydrogen bonding, as well as the homogenous microstructure obtained through uniform SiO_2 distribution (shown in SEM and EDS). P50 had much higher absorption coefficient than P80 and PMMA. P50's microstructure showed more degree of phase separation and less uniform SiO_2 distribution, which may cause the stronger light scattering, thereby contributing to the higher absorption[57,58].

(2) In the near infrared region (800-2000 nm), it is noted that P80 had lower absorption coefficients than PMMA, while P50 had similar absorption to PMMA. The

absorption bands at about 1700 nm were attributed to the overtones of C-H bond vibration, whereas the bands at 1400 nm and 1900 nm were ascribed to O-H overtones. The absorption may result from the following reasons. On one hand, the optical loss from C-H overtones is lower due to the dilution of the organic by the inorganic component in the hybrids. On the other hand, the absorption is also related to the light scattering caused by phase separation and surface roughness, as well as the loss from O-H overtones. Because P80 exhibited more uniform microstructure and probably less O-H groups than P50, its absorption was lower than PMMA, while P50 had similar absorption to PMMA.

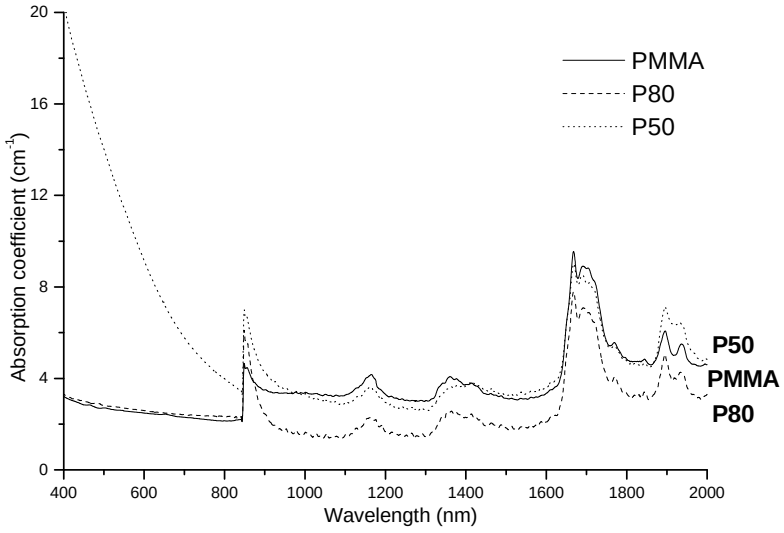

Fig. 4.9 Vis/NIR absorption spectra of the PMMA and PMMA/SiO_2 samples.

4.3.2 Deposition and characterization of the PMMA/SiO_2 lines

The composition of P80 was chosen for the deposition due to its better uniformity and optical properties shown in the investigation of P80, P50 and P20 monoliths. For the Micropen^{TM} deposition, at first, several of the following problems were encountered: (1) the material leaked from the pump block; (2) the sol-gel solution gelled at the pen tip as well as inside the pen tube; (3) The toxic THF evaporated and could be inhaled without the protection of hood. To solve these problems, a smaller pressure (30 decreased to 10 psi) was exerted on the syringe for the deposition. The solvent, DMAc, with a much higher boiling point (~165 $^{\circ}$C) than THF (~66 $^{\circ}$C) was used to prepare the P80 sol-gel solution, which was helpful to achieve lower volatility and prevent pen tip clogging. The P80 solution's viscosity was increased from ~0.2 to ~6 Pa·s (at shear rate=1 s^{-1}) by heating at ~85 ºC, in order to avoid leakage during the deposition. Under the modified condition mentioned above, no leakage or pen tip clogging was observed.

Fig. 4.10 (a)-(d) shows the SEM images of deposited lines using the P80 sol-gel solution on glass slides. Fig. 4.10 (a) is the image of five deposited lines at lower magnification, (b) is the cross section of an one-layer line, (c) is the cross section of a five-layer line, and (d) is the enlarged image of (c). It was found that the line width was ~220-240 μm, and the typical one-layer thickness was ~5-7 μm. Fig. 4.10 (b) shows that multilayers were bonded well and no delamination was observed. It is also noted that disc-shaped SiO_2 particles formed in the matrix (marked in the figure), which was not observed for the P80 monolith. This could be attributed to the different solvent used, and the faster solvent evaporation for the deposition (at ~85 ºC for 7 h) compared to the slow drying for preparing the P80 monolith (at room temperature for 2 weeks).

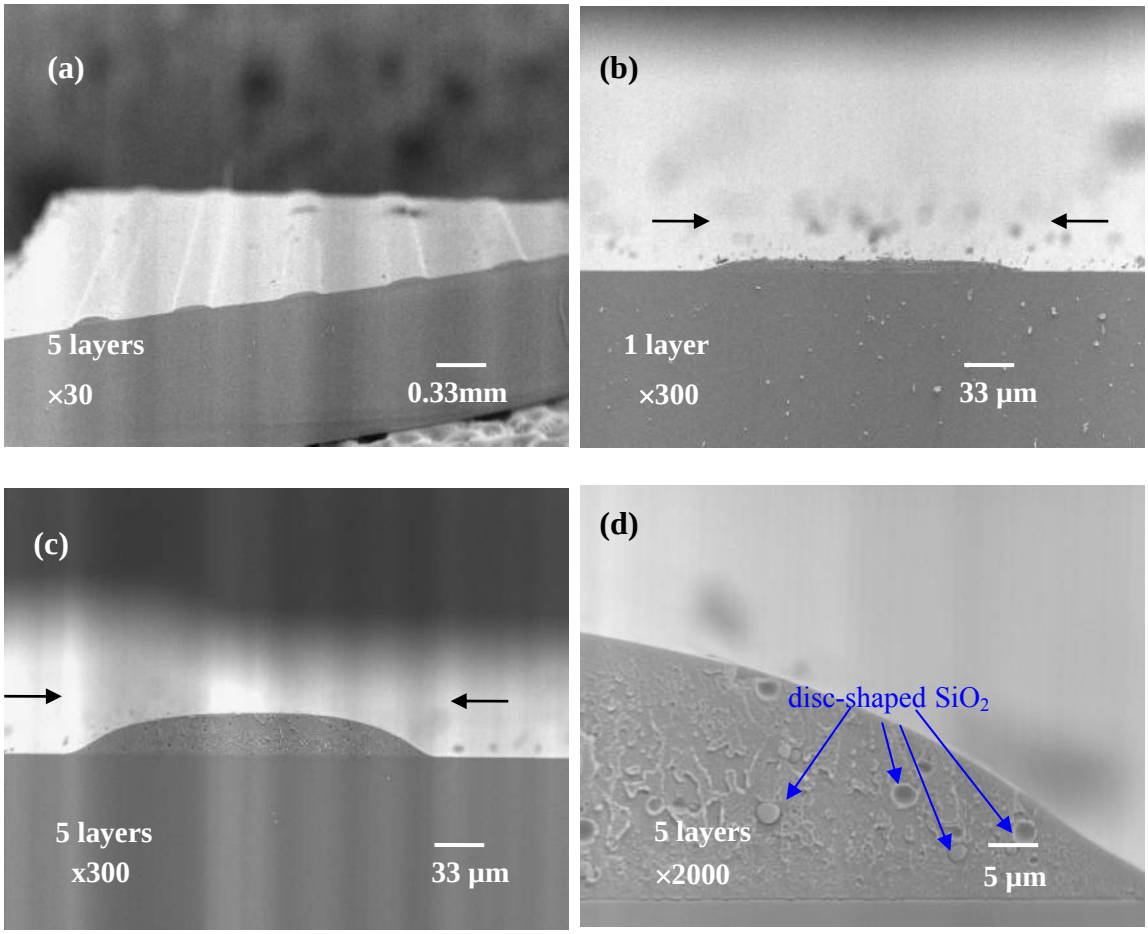

Fig. 4.10 SEM images of the deposited lines on glass slides using the P80 sol-gel solution.

4.4 Summary

PMMA/SiO_2 hybrid monoliths were successfully synthesized via the sol-gel process. Three different organic/inorganic ratios (P80, P50 and P20) were investigated. The optical transparency was better with increasing PMMA content. TGA results suggested the successful incorporation of SiO_2 in the synthesis and improved thermal stability for the hybrids. Infrared spectra indicated the formation of hydrogen bonding between the organic and inorganic components. SEM images showed the morphology evolution from P80 to P20. The EDS results clearly revealed the different SiO_2 distribution in the hybrids. The hybrids' refractive index could be adjustable and P80 had the lowest absorption both in the visible and near infrared regions among the three hybrids.

We have also demonstrated the feasibility of direct writing of the PMMA/SiO_2 lines using the Micropen^{TM} technique, which may have potential applications in optical devices. The deposition quality can be improved by choosing a solvent with higher boiling point, varying the solution's viscosity and adjusting writing parameters.

CHAPTER5 DIRECT-WRITE DEPOSITION OF PZT THICK FILMS DERIVED FROM A MODIFIED SOL-GEL PROCESS

5.1 Introduction and objectives

This chapter describes the fabrication of lead zirconate titanate (PZT) thick films by Micropen™ direct-write. The writing material was prepared by a modified sol-gel process to achieve low temperature heat treatment (700 ºC). This chapter is organized into three sections: (1) an introduction to the modified sol-gel process for the preparation of PZT thick films; (2) the experimental procedures to prepare and characterize the PZT sol-gel solution, pastes and films; (3) the discussion of the characterization, including the thermal analysis, the rheology study of the PZT pastes, and the microstructures and properties of the thick films.

5.1.1 Sol-gel process for the preparation of PZT films

Lead zirconate titanate (PZT) thin and thick films have many applications due to their excellent ferroelectric, pyroelectric and piezoelectric properties. For example, PZT thin films (<1 μm) have been extensively studied for non-volatile, high speed random access memories (FRAMs) based on ferroelectric properties. A further benefit of a thin film for the FRAM applications is that switching voltages required are decreased to standard logic level of 3-5 V [59]. Other applications for thin films include infrared detectors, surface acoustic wave devices, accelerometers, and microelectromechanical systems (MEMS) [60].

There are a variety of methods for the fabrication of high-quality and uniform thin films, such as sol-gel process, RF sputtering, metallorganic chemical vapor deposition (MOCVD) and pulsed laser deposition (PLD). Among them, the sol-gel method allows

the preparation of homogeneous compositions by molecular mixing in solution. The main advantages of this method are low temperature processing, good control of stoichiometry, better film homogeneity, deposition of large area thin films and low cost[61, 62]. The basic principle of the sol-gel process is that metal alkoxides precursors dissolved in an organic solution form a sol and then a gel by hydrolysis and condensation reactions. In the sol-gel process, the variables affecting the characteristics of final films are the reactions between alkoxides, the nature and amount of solvent, the profiles of heat treatments, the choice of substrates, and so on[63,64,65].

Thick films fill an important technological gap between thin films and bulk ceramics. Many potential applications require PZT thick films (1-100 μm), such as high-frequency transducers in medical imaging, fiber optic modulators and self-controlled vibrational damping systems [66] . PZT thick films can also be used for microelectromechanical systems (MEMS) for large strain and displacement[67,68].

A conventional method to prepare thick films is screen-printing[69]. It normally requires high temperature heat treatment (> 850 ºC) to achieve adequate sintering of the PZT particles. A conventional sol-gel process can be adapted to prepare thick films for low-temperature annealing, but multiple layers have to be deposited which is time-consuming[70]. The main challenge of the conventional sol-gel is to prepare crack-free single layer films thicker than 1 μm. Also multilayer deposition will promote crack above a critical thickness (~10 μm) due to mechanical stress[71,72].

A modified sol-gel approach for PZT thick films was first reported by Barrow *et.al.* in 1995[73]. In their work, PZT powder was dispersed in a PZT sol-gel matrix to form a 0-3 ceramic/ceramic composite. The resulting solution was then spin-coated on

substrates, fired and annealed in the same manner as conventional sol-gel. The fired film is made up of two phases: ceramic particles and fine grains surrounding them which are the sol-gel matrix. This novel approach has all the benefits of a conventional sol-gel. In addition, by varying the concentration of ceramic powder in sol-gel solution, the thickness of an individual layer in the range of 0.5-10 μm was easily achievable. Also, the PZT thick films were fabricated in the 5-60 μm thickness range by depositing multiple layers[71]. An appropriate analogy proposed by the authors is that the sol-gel makes up the mortar and the ceramic particles make up the bricks in a wall. The fact that films do not crack during processing can be attributed to two factors: (1) strong bonds between the sol-gel and ceramic powder due to the surface hydroxyl groups (-OH); (2) less shrinkage due to a significant amount of ceramic powder which decreases the percentage of sol-gel solution in the film. Fig. 5.1(a) shows the SEM cross-section of a 20-μm PZT thick film in their work[73]. This film was spin-coated on a silicon substrate by depositing 10 layers, and each layer was fired at 500 ºC, and the overall film was annealed at 650ºC for 30 min. This film had a dielectric constant (K) of 900, remnant polarization (P_r) of 35 μC/cm^2, and coercive field (E_c) of 20 kV/cm.

Using the similar modified sol-gel approach as that developed by Barrow *et. al.*, a number of groups has successfully fabricated PZT thick films[74]. Table 5.1 lists some of the results in those studies. Fig. 5.1(b) shows the SEM cross-section of a 16-μm PZT thick film in the work of Zhou *et. al.*, which was spin-coated on silicon, and each layer was heat treated at 150 ºC followed by another at 400 ºC, and the overall film was annealed at 700 ºC for 1h.

The modified sol-gel process has been applied successfully to prepare PZT thick films at low temperatures, thus compatible with the existing silicon technology. However those films were deposited mainly using spin-coating technique. In recent years, the fabrication of thick films by direct-write technologies has received increasing attention. Micropen^{TM} direct-write technique has been used to write thick films of PZT, barium strontium titatnate (BST) and zinc oxide (ZnO) by Lewis's group and Electroceramics group (ECG) at Rutgers University (refer to Chapter 1). The materials for those thick films were prepared by mixing ceramic powders, solvents and binders. Consequently, a high temperature sintering (900-1200ºC) was required. For the first time, we have chosen the combination of the modified sol-gel process and Micropen^{TM} technique to prepare PZT thick films, in order to integrate direct writing with silicon technology.

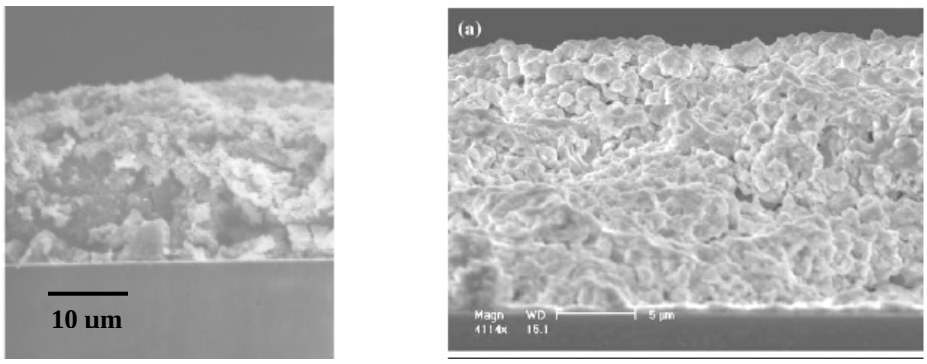

(a) (b)

Fig. 5.1 SEM cross-sections of (a) a 20-µm PZT thick film in the work of Barrow *et. al*[73]., and (b) a 16-µm PZT thick film in the work of Zhou *et. al.*[76],

Table 5.1 The summary of thick films prepared by the modified sol-gel process.

Studies	**Film thickness (µm)**	**Dielectric properties (at 1 kHz)**	**Ferroelectric properties**	**Reference**
D. Xia	50	K=860 loss =0.03	P_r=25 µC/cm^2 E_c=40 kV/cm	75
Z. Wang	13	K=540 loss =0.02	P_r=16 µC/cm^2 E_c=45 kV/cm	72
Q.F. Zhou	16	K=780 loss =0.04	P_r=12 µC/cm^2 E_c=30 kV/cm	76

5.1.2 Objectives

The objectives of this chapter are:

(1) To apply the Micropen^{TM} direct-write technique for the deposition of PZT thick films (10-100 μm in thickness) on silicon and alumina substrates. A modified sol-gel process will be designed to prepare the materials for the deposition, with the purpose of achieving low temperature annealing (~700 °C) of PZT thick films for MEMS, high frequency medical imaging and other applications.

(2) To study processing parameters, such as powder concentration in PZT pastes, Micropen^{TM} writing parameter and substrates, to obtain crack-free thick films with good dielectric and ferroelectric properties.

(3) To characterize the resulting PZT thick films, including the studies of the crystallization, microstructure, dielectric and ferroelectric properties.

5.2 Experimental Procedures

5.2.1 PZT sol synthesis

A PZT sol was prepared by a modified version of the approach followed by C. Livage *et al.*[77]. The main modifications were that all handling operations were performed under Ar inert atmosphere and the titanium and zirconium precursor solution was prepared in glove box.

The starting materials were lead acetate trihydrate ($Pb(CH_3COO)_2{\cdot}3H_2O$), titanium isopropoxide ($Ti[(CH_3)_2CHO]_4$) and zirconium propoxide ($Zr[O(CH_2)_2CH_3]_4$) (in 1-propanol, 70 wt%). Ethylene glycol ($HOCH_2CH_2OH$) was chosen as the solvent and stabilizing agent, instead of 2-methoxyethanol ($CH_3OCH_2CH_2OH$) which is more toxic. Fig. 5.2 is the flow diagram for the synthesis of the PZT sol-gel solution. The composition of the precursor designed in this work was $Pb(Zr_{0.52}Ti_{0.48})O_3$, which is near the morphotropic phase boundary (MPB) of PZT having optimum electromechanical properties. Lead acetate trihydrate was first dissolved in ethylene glycol, and 5 mol% excess lead was added to compensate for the lead loss during annealing. After distillation of water at 105 ºC, an amber-color solution was obtained. Separately, titanium isopropoxide and zirconium n-propoxide were mixed in 2-propanol in glove box, with Zr/Ti molar ratio of 52/48. Then, the titanium-zirconium solution was added dropwise to the lead solution under rapid magnetic stirring. Although a small amount of white precipitate formed at this point, it could be quickly dissolved by stirring at 80 °C. After adding concentrated acetic acid (CH_3COOH) as reaction catalyst, the solution was refluxed for 2 h at 80 °C and then stirred overnight at room temperature. A transparent

amber-color sol (PZT 0.7 M ca.) was obtained. The PZT sol exhibited high stability for several months.

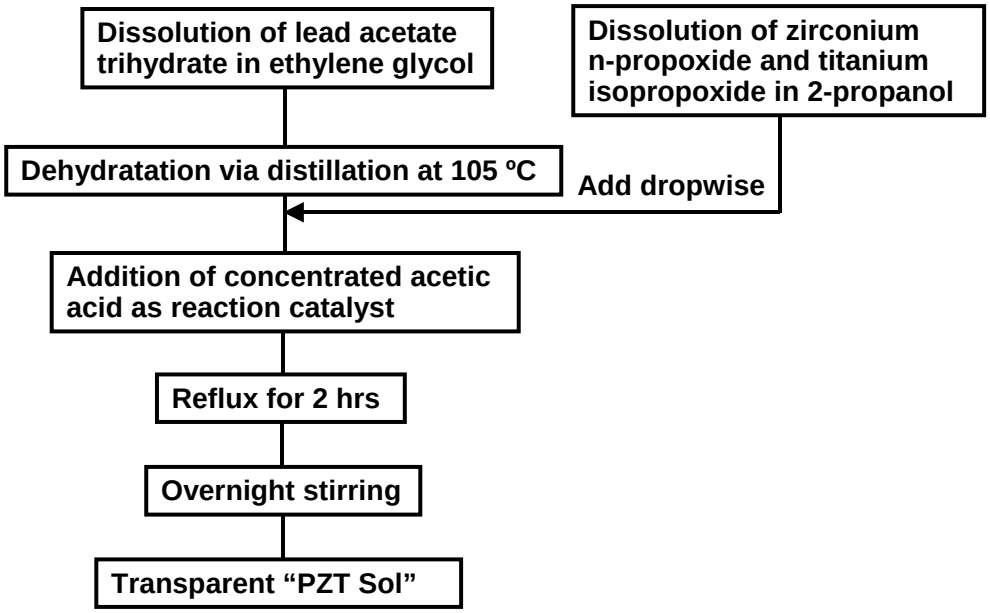

Fig. 5.2 Flow diagram for the PZT sol synthesis.

5.2.2 Thick film deposition

The PZT paste for the deposition of thick films was prepared by taking a modified sol-gel process, in which PZT ceramic powder was dispersed in the PZT sol. Commercial PZT powder (PZT-5H, *TRS Ceramics, Inc.*) with an average particle size of 1.2-1.5 μm was dry milled with a 8000M Mill® system (*SPEX CertiPrep, Inc.*). Powder with sub-micron particle size (0.4-0.6 μm, measured by particle size measurement) was achieved after milling. Then, the milled powder was dispersed in PZT sol by magnetic stirring and ultrasonication. The resulting slurry was a PZT paste, which was used a writing material for the Micropen™ deposition. It is important to note that in the preparation of the PZT paste, the sol solution was used as a binder, and no additional binder was added.

In the following, the PZT paste derived from the modified sol-gel process is referred to as "paste" or "P", and the pure PZT sol solution is referred to as "sol" or "S".

For example, “S-P-P-P-P” represents a five-layer film, consisting of the first layer deposited using a PZT sol and the next four layers deposited using the PZT paste. The bottom sol layer was used to promote the adhesion between the paste layer and the substrates.

The vol% and wt% of PZT powder in the PZT pastes are reported in Table 5.2. The value of “designed vol%” only included PZT powder added to the paste. The value of “actual wt%” included both the added PZT powder and the PZT residue converted from the sol as measured by TGA. The value of “actual vol%” was simply calculated based on the value of “actual wt%”. In the calculation, it was assumed that the densities of the sol and of the PZT powder were 1 g/cm^3 and 7.6 g/cm^3, respectively.

The flow diagram of the preparation of PZT thick films is shown in Fig. 5.3. Several layers of PZT sol and paste with different concentrations or combination of both were deposited by Micropen^{TM} on silicon and alumina (deposited with Pt bottom electrode) substrates. After depositing each layer, samples were allowed to rest on the Micropen^{TM} stage for 30 min to stabilize the flow of the deposited pastes for more uniform surface. Then samples were transferred to a hot-plate for a two-step pyrolysis sequence to remove the solvent and decompose the organic compounds. The sequence consisted of a heat treatment at 200 ºC for 10 min, followed by heating at 400 ºC for 10 min (refers to section 5.3.1 for the reasons of choosing the two-step heat treatment). The procedure above was repeated for every additional layer. The final heat treatment (annealing) for crystallization of the resulting thick films was carried out at 700 ºC in air for 30 min (referred as “normal annealing”) or for 2 min (referred as “fast annealing”, only for using silicon substrates). “Fast annealing” was done by placing the samples in a

furnace which was pre-heated at 700 ºC. The main purposes of "fast annealing" are to limit lead loss during heat treatment and the unwanted reactions between the film and substrates.

In this study, a pen tip with inner diameter of 250 μm was used for the Micropen^{TM} deposition. The writing parameters using the PZT sol and PZT pastes were listed in Table 5.3. The main difference between the deposition using a sol and a paste was the "cross section" value. A smaller "cross section" (CS) of 1 mil^2 (=645 μm^2) was used for the sol deposition. Larger CS values of 2, 5, 10 or 15 mil^2 (=1290, 3226, 6452, 9677 μm^2) were chosen for the paste deposition to obtain films with different thickness.

5.2.3 Substrates and electrodes

The substrates used in this study were alumina (CoorsTek Inc., CO, US) and silicon (Inostek Inc., Gyeonggi, Korea). The alumina substrates are widely used in the electronic industry, and silicon is an important substrate in microelectromechanical systems (MEMS) and other integrated circuit applications.

Prior to the film deposition on alumina substrates, a commercial platinum paste (CL11-5100, Heraeus Inc., PA, US) was diluted using α-terpineol to make a slurry and then deposited by the Micropen^{TM} as bottom electrode, and fired at 1100 ºC for 15 min. The writing parameters for the deposition of Pt bottom electrode were listed in Table 5.3. After firing, the Pt electrode layer was ~7 μm thick with a surface roughness of ~ 0.4 μm. The silicon substrates used were commercially available platinum coated silicon Pt/Ti/SiO_2/Si (100), thus no Pt layer was deposited by the Micropen^{TM}. The thicknesses of each layer on the 525-μm thick silicon substrate were 300 nm (SiO_2), 10 nm (Ti) and 150 nm (Pt, <111>), respectively.

Table 5. 2 Composition of the PZT pastes.

PZT powder dispersed in the PZT sol (g/ml)	Designed vol%	Actual wt%	Actual vol%
1.3	15	67	17
1.9	20	73	22
2.5	25	78	27
3.3	30	82	32

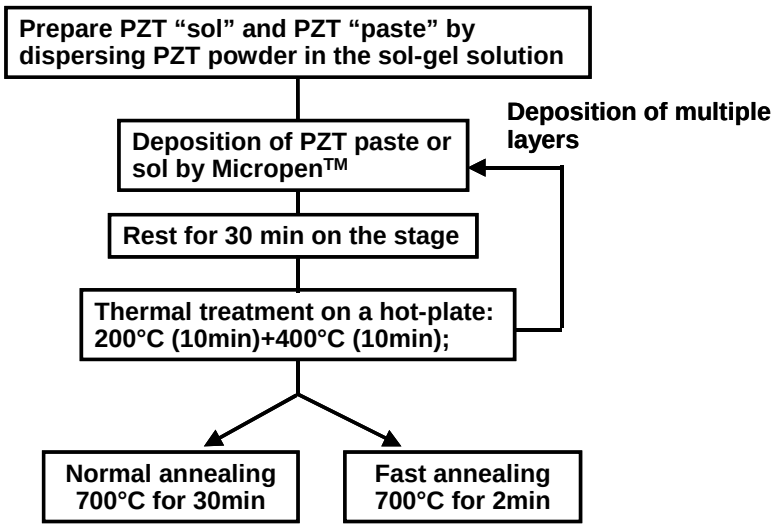

Fig. 5.3 Flow diagram for the preparation of PZT thick film.

Table 5. 3 The Micropen™ parameters for the direct-write of PZT sol, PZT pastes and Pt paste (using a 250-μm pen tip).

	Cross section (mil^2)	Writing speed (mil/s)	Writing force (mg)	Trigger height (mil)	Lift force (mg)	Lift speed (mil^3/s)	Term volume (mil^3)	Term speed (mil^3/s)	Burst volume (mil^3)	Burst speed (mil^3/s)
PZT sol	1	50	5	0.04	10	1000	300	3000	500	1000
PZT pastes	5-15	50	15	0.05	10	1500	1000	3000	800	1500
Pt paste	15	200	25	0.15	25	5000	6000	40000	0	500

5.2.4 Materials and films characterization

Rheological measurements of the PZT sol and pastes were performed at 20 ºC using an AR1000-N rheometer (TA instruments) fitted with a concentric cylinder with conical end geometry. Thermogravimetric analysis (TGA) and differential thermal analysis (DTA) were measured with Perkin-Elmer TGA7 and DTA7, in the range 50-800ºC at a heating rate of 10 ºC/min in air, for a PZT sol, a PZT paste and a xerogel. The crystalline phase of a PZT thick film was characterized by X-ray diffraction, using CuK_{α} radiation. The thickness and surface roughness of thick films were measured using a profilometer (Alpha-Step 200, TENCOR Instruments). The fracture surface of thick films was examined by field emission scanning electron microscopy (LEO-ZEISS, Gemini 982) to study the film's microstructure.

Gold electrodes (~ 2 mm in diameter) were sputtered on top of the thick films through a home-made mask for dielectric and ferroelectric measurements. The dielectric constant and dielectric loss were measured with an impedance grain/phase analyzer (HP4194A, Hewlett Packard) in the range of 1 kHz-1 MHz at room temperature. The polarization versus electric field measurements were carried out by using a Radiant Precision LC system (Radiant Technologies Inc, NM).

5.3 Results and Discussion

5.3.1 Thermal analysis of the PZT sol and PZT paste

Thermal analysis of a PZT sol, paste and xerogel were carried out to determine the proper heat treatment process. Fig. 5.4 (a) shows the TGA profiles of the PZT sol and of a representative PZT paste with 20 vol% PZT powder loading. The solid residues at 800 ºC for the PZT sol and the 20 vol% PZT paste were 22 wt% and 73 wt%, respectively. Such results showed that in a conventional sol-gel, staring materials had a big amount of weight loss (~78 wt%), resulting in large shrinkage during heat treatment. In contrast, for the PZT paste derived from the modified sol-gel process, the weight loss decreased dramatically to ~ 27 wt%, leading to much less shrinkage. In addition, the first observable weight loss occurred well below 200 ºC for the PZT sol and paste corresponding to the removal of organic solvents (ethylene glycol). A second gradual weight loss took place between 200 ºC and 400 ºC, which was attributed to the decomposition of methyl and acetate groups. The small weight losses (~ 2 wt%) for both samples in the range of 400-600 ºC were probably associated to the removal of the remaining carbon in the compound during the PZT crystallization process[77]. Fig. 5.4 (b) shows the DTA spectrum of a PZT xerogel obtained from the PZT sol after 2-days heat treatment at 70 ºC and 1 day at 120ºC. The DTA spectrum exhibited two main exothermic peaks at approximately 370 ºC and 450 ºC, due to the pyrolysis of carbonyl groups and PZT perovskite phase crystallization, respectively[78]. The overall thermal analysis of the PZT sol, PZT paste and xerogel provided the guidelines for the heat treatment of as-deposited films. It suggested a two-step procedure, consisting of heating at 200 ºC first and then at 400 ºC, to remove the solvents and organic groups, respectively.

5.3.2 Rheological characterization of the PZT sol and PZT pastes

Because the Micropen^{TM} is a deposition technique based on extrusional method, it is important to determine the rheological properties of writing materials. Fig. 5.5 depicts the viscosity as a function of shear rate (1-200 s^{-1}) for the PZT sol and the PZT pastes with 20, 25 and 30 vol% solids loadings within the PZT sol. It was found that all the PZT pastes exhibited shear thinning behavior, and the sol showed nearly Newtonian behavior. As proposed by Dimos et al., the "writing range" of Micropen^{TM} corresponds to higher shear rates (20-85 s^{-1}), and the "settling range" corresponds to lower shear rates (<1 s^{-1}). Fig. 5.5 shows that the PZT pastes and sols exhibited viscosities < 3 Pa·s in the "writing range", and < 20 Pa·s in the "settling range". The relatively low viscosities in both two ranges indicated that the PZT pastes and sols were more suitable for the deposition of films instead of high definition patterns. Because the latter one requires writing materials with higher viscosity, higher degree of shear thinning and higher elasticity, which spread less on substrates after deposition.

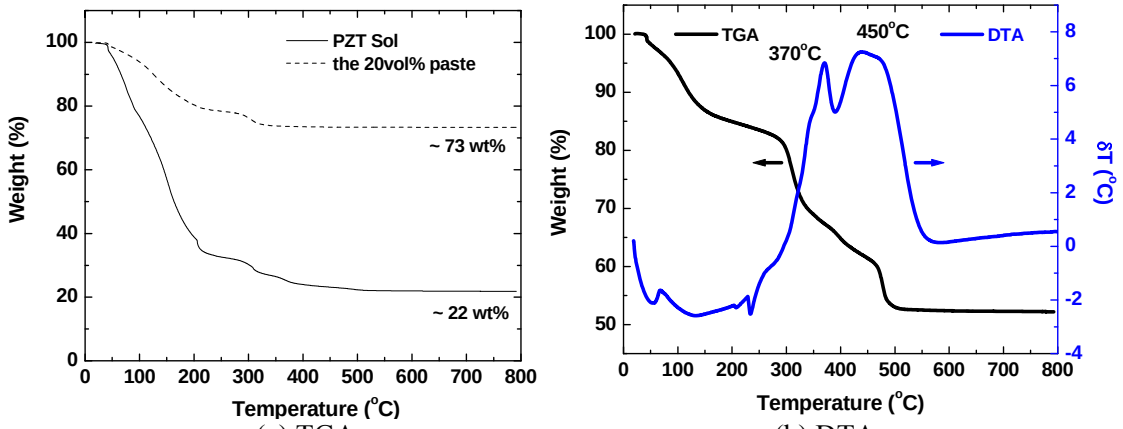

(a) TGA (b) DTA

Fig. 5.4 (a) TGA curves of the PZT sol and a representative PZT paste, and (b) DTA curve of a PZT xerogel (in air).

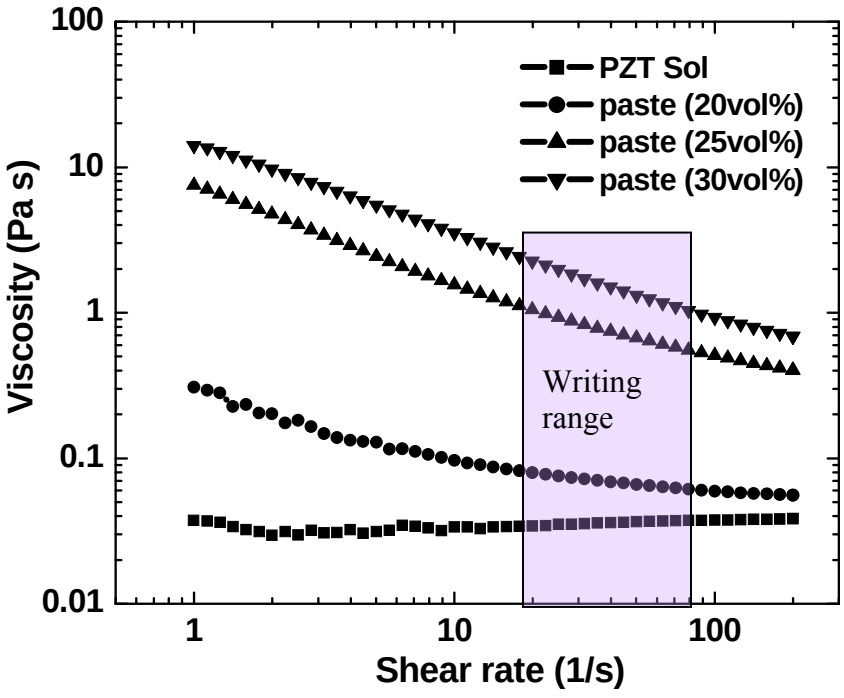

Fig. 5.5 The viscosity as a function of shear rate for the PZT sol and selected PZT pastes.

5.3.3 Crystallinity of the PZT films

Fig. 5.6 shows the XRD patterns of a representative PZT film on an alumina substrate and of commercial PZT powder as a reference. The 15-μm thick film was deposited of six layers in a sequence of "S-P-P-S-P-P", using the PZT sol and 20 vol% PZT paste, and annealed at 700 ºC for 30 min (normal annealing). A single perovskite phase was present in the film, and the peaks associated with pyrochlore phase ($2\theta \approx 29^{o}$) or other secondary phases were not detected within the XRD resolution limit. This result indicates that single phase PZT films can be obtained at low temperature heat treatment, due to using the modified sol-gel process.

5.3.4 Effect of "Cross Section" on the film thickness

As discussed in Chapter 3, the important Micropen^{TM} writing parameter, "cross section", allowed for a precise control of the amount of PMMA solutions dispensed. The similar conclusion can be drawn for the deposition of PZT pastes. The thickness variations as a function of "cross section" for the PZT pastes with 15, 20 and 25 vol% solids loadings are listed in Table 5.4, and also plotted in Fig. 5.7. The films were four-layer films deposited in a sequence of "P-P-P-P" on silicon substrates, and annealed at 700 ºC for 30 min (normal annealing). First, the approximate linear relationship between the film thickness and "cross section" (CS) indicated that CS was crucial for controlling film thickness. Second, at a same value of CS, the film thickness increased as the vol% of PZT powder in the PZT sol increased. In addition, for a specific powder concentration, the film thickness increased by 3-5 times when increasing CS from 2 to 15 mil^2 (from 1290 to 9677 μm^2). By changing the paste concentration and CS values, the thickness of

single-layer film was varied in a wide range from 1.5 to 17.5 μm, and up to 70-μm thickness films can be achieved consisted of four layers.

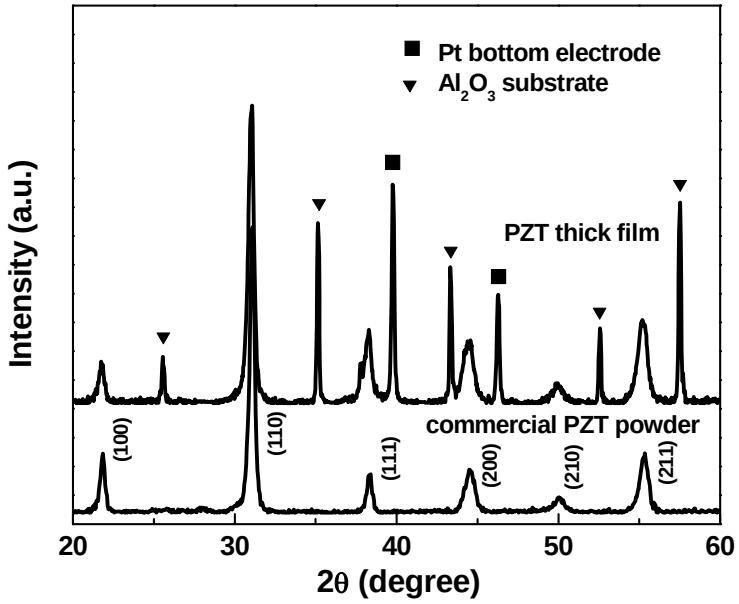

Fig. 5.6 X-ray patterns of a representative PZT film on Al_2O_3 substrate in comparison with commercial PZT powder.

Table 5.4 The film thickness for three PZT pastes deposited using different values of "cross section" (CS).

CS (mil^2)	**2**	**5**	**10**	**15**
CS (μm^2)	1290	3226	6452	9677
15 vol%	6 μm	13 μm	18 μm	31 μm
20 vol%	10 μm	20 μm	35 μm	/ (did not write)
25 vol%	20 μm	40 μm	51 μm	70 μm

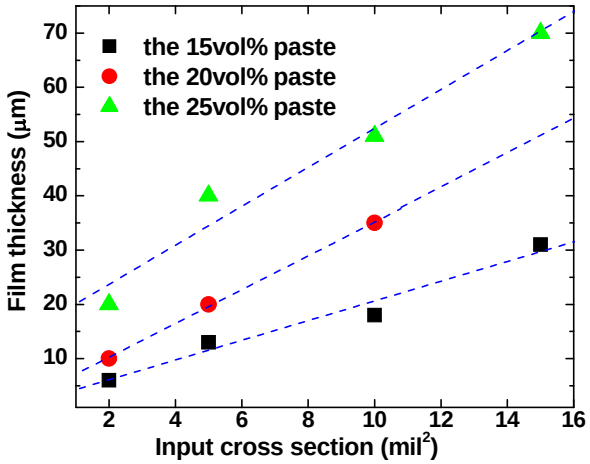

Fig. 5.7 Film thickness as a function of "cross section".

5.3.5 Surface roughness and microstructure of the films

Fig. 5.8 (a)-(c) show the optical pictures of three representative films on silicon substrates. They were five-layer films with 1 cm^2 area deposited in a sequence of "S-P-P-P-P" using the PZT sol and PZT pastes with 15, 20 and 25 vol% ("cross section"=5 mil^2), and annealed at 700 ºC for 30 min (normal annealing). The films' surface roughness was measured by a profilometer (refers to section 5.2.4). It was found that the films' surface roughness increased from ~ 1.0 to 2.2 and to 4.1 μm, as the PZT powder concentration increased from 15 to 25 vol%. It indicated that the paste uniformity decreased, which was probably due to more agglomeration of PZT powder in the sol-gel matrix with increasing powder concentration. The similar trend was also observed in the PZT pastes derived from the modified sol-gel process by Barrow *et. al.*[71]. The surface roughness of the films increased from 2 μm at low powder concentrations (20 wt%) to ~5 μm at higher concentrations (~65 wt%). To improve film uniformity, other approaches, such as adding surfactant to better disperse PZT powder in the system can be taken.

Fig. 5.9 show the FESEM images of a representative film on a silicon substrate. It was a four-layer film deposited in a sequence of "P-P-P-P" using the 15 vol% PZT paste ("cross section"=5 mil^2), and under "fast annealing". Fig. 5.9 (a) shows that the film was crack-free, homogeneous and dense, which was comparable to the films deposited by spin coating using a modified sol-gel process[72, 73, 76]. The film thickness was ~12 μm. The detailed microstructure of the film can be revealed at higher magnification in Fig. 5.9 (b). It was found that the film basically consisted of two regions: the bigger grain region (~0.6 μm) should come from the milled commercial PZT powder (~0.4-0.6 μm), and the smaller grain region (marked by circles, <0.2 μm) surrounding the bigger grains should come from the crystallization particles derived from the sol-gel matrix.

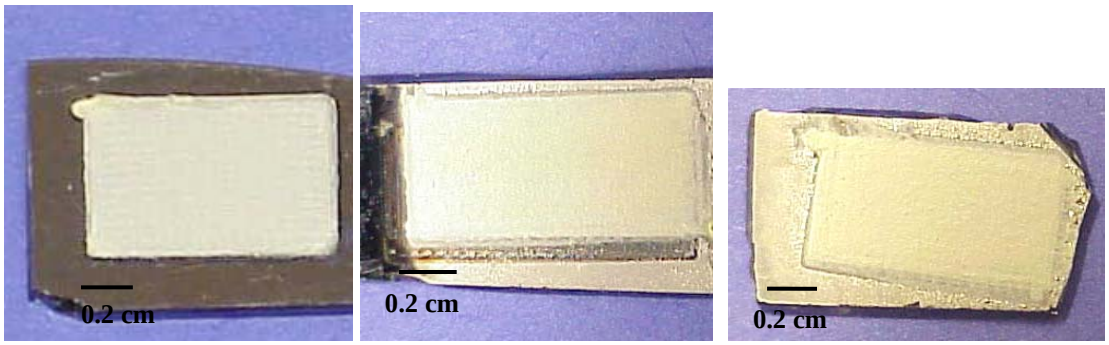

(a) 15 vol% (b) 20 vol% (c) 25 vol%

Fig. 5.8 Optical pictures of the annealed PZT thick films of three concentrations.

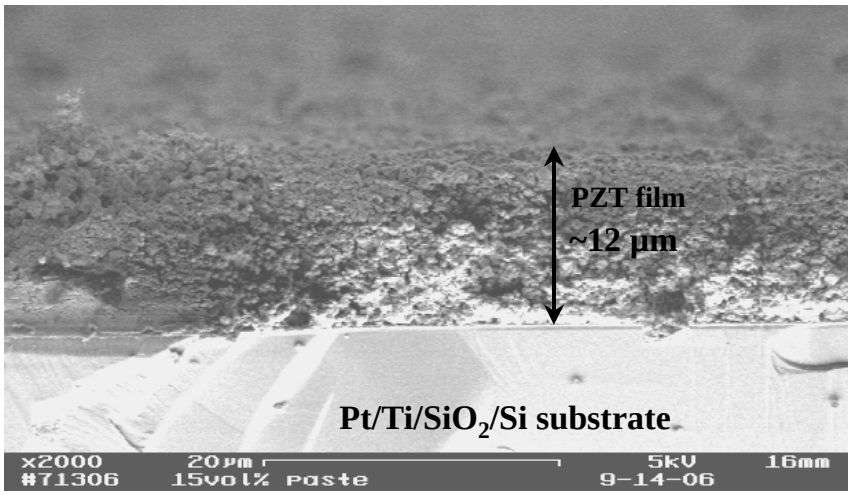

(a)

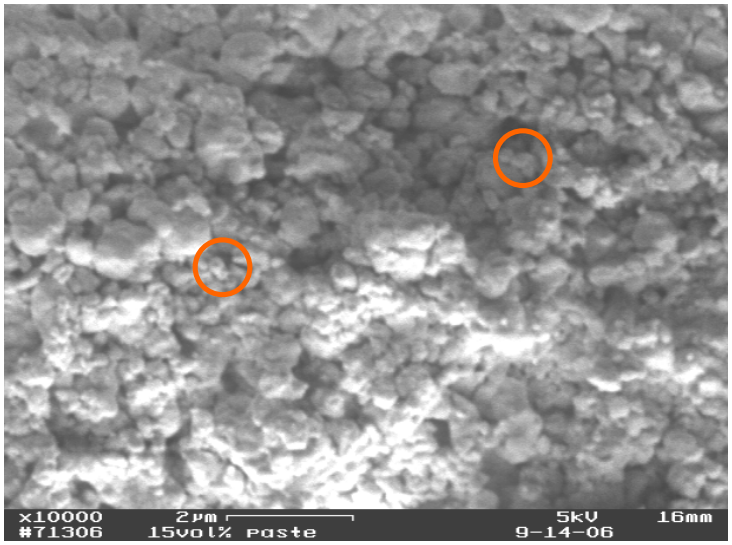

(b)

Fig. 5.9 FESEM images of a PZT thick film (a) at low and (b) at high magnification.

The bigger grains were bound by the smaller grains, showing a vivid picture of the "bricks (ceramic particles) and mortar (sol-gel)" analogy proposed by Barrow (refer to section 5.1.1). Therefore, Fig. 5.9 revealed that a dense and crack-free thick film derived from the modified sol-gel process can be fabricated by the Micropen^{TM} technique.

5.3.6 Dielectric and ferroelectric properties

Fig. 5.10 shows the frequency dependence of dielectric constant and dielectric loss of a 16-μm film on a silicon substrate. It was a four-layer film deposited in a sequence of "P-P-P-P" using the 15 vol% PZT paste (CS = 10 mil^2), and annealed at 700ºC for 2 min (fast annealing). It was found that the dielectric constant and dielectric loss were 870 and 4.1% at 1 kHz, respectively. The dielectric properties of the film deposited by Micropen^{TM} were comparable with that of films fabricated by spin coating (refer to Table 5.1).

Fig. 5.11 gives the values of remanent polarization (P_r) and coercive field (E_c) for three representative films on silicon substrates. They were four-layer films deposited in a sequence of "P-P-P-P" using the 15 vol% PZT paste, and annealed at 700ºC for 2 min (fast annealing). These films were deposited with different "cross section" values to obtain different thickness. It was found that the film thickness increased from 6 to 12, and to 16 μm as "cross section" increased from 2 to 5 and to 10 mil^2 (i.e. 1290 to 3206 and to 6452 μm^2), respectively. The three films had similar E_c of ~27 kV/cm, but the P_r values increased from 6.7 to 11.5 and to 12.2 μC/cm^2, with increasing the film thickness. The P_r and E_c values of the film deposited by Micropen^{TM} were comparable with that of films fabricated by spin coating (refer to Table 5.1). In addition, the trend that thicker films had higher P_r values has been observed for PZT films. This can be explained on the basis of

several factors including the diffusion between the films and the substrates, lead loss, and the residual stress on the films. For example, the lead loss is less significant for thicker films, and the diffusion is limited to the interface area, thus the overall properties of thicker films are normally better than thinner films[79].

Furthermore, some other general trends were observed in our investigation (listed in Table 5.5), which may be helpful for the future work in this direction:

(1) The films on alumina substrates exhibited lower properties (such as lower dielectric constant, lower remanent polarization and higher coercive field) than the films on silicon substrates. The main reason could be more diffusion between the films and Pt bottom electrode on alumina substrates. Because the Pt bottom electrode was deposited by Micropen^{TM} and therefore it was inevitably much thicker (several μm) than the Pt layer (~150 nm) sputtered on commercial silicon substrates.

(2) The films deposited on silicon substrates using the 15 and 20 vol% PZT pastes showed much lower dielectric loss (tanδ=4-6%) and less porosity than the films deposited using the 25 and 30 vol% pastes (tanδ=10-15%). These results were probably due to less uniformity of the films when powder concentration was higher than a certain level.

(3) The films consisting of bottom and intermediate sol layers as compared to paste layer only films, exhibited slightly lower dielectric loss and higher resistance to electrical breakdown in the hysteresis loop measurements. This can be explained by the enhanced adhesion between the film and substrate for the film having a bottom sol layer, and increased density for the film with intermediate sol layers. In this case, the sol infiltrated into the pores of paste layers and enhanced the sinterability and density.

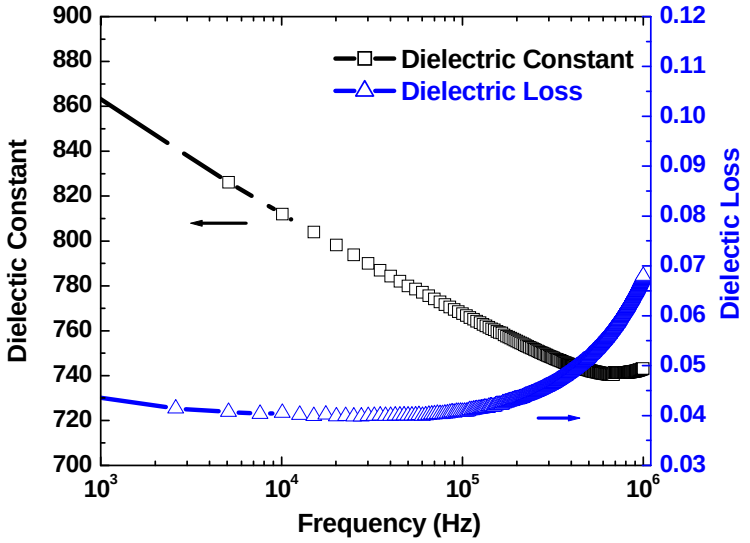

Fig. 5.10 Dielectric properties of a 16-μm film on a silicon substrate (CS = 10 mil^2).

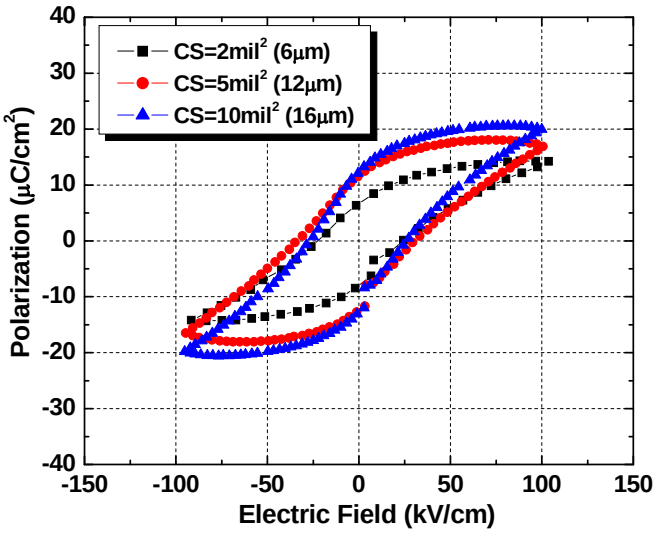

Fig. 5.11 Hysteresis loops for three films deposited with different "cross section" on silicon substrates.

Table 5. 5 Comparison of some representative films ("Cross section"=5 mil^2).

Films	K & loss	P_r (μC/cm^2), E_c (kV/cm)
20 vol% paste, on Al, normal annealing	470, 5%	P_r=11, E_c=50
15 vol% paste, on Si, normal annealing	580, 6%	P_r=9, E_c=33
20 vol% paste, on Si, normal annealing	530, 4%	P_r=12, E_c=35
25 vol% paste, on Si, normal annealing	-, 11%	-,-
30 vol% paste, on Si, normal annealing	-, 15%	-.-
15 vol% paste, on Si, fast annealing	580, 5%	P_r=11, E_c=27

"-" means these samples have not been measured.

5.3.7 Preliminary work on the deposition of small circles and dots

We have demonstrated Micropen^{TM}'s capability of writing line patterns, but its ability of writing small circles and dots has not been explored. The main purpose of this part of work is to explore the Micropen^{TM}'s potential of direct writing of small circles and dots with the smallest dimension and best continuity.

The preliminary work is shown in Fig. 5.12. These circles were deposited on silicon substrates using a 250-μm pen tip and the 25 wt% PZT pastes derived from the modified sol-gel process. The circles were ~ 2 mm in diameter, with 6, 5, 4 and 3 layers (from left to right). Fig. 5.12 also shows the surface of these circles were not uniform, which was probably due to the relatively high solid loading of the 25 wt% paste. To achieve better surface uniformity, PZT pastes with less solid loadings can be used, and the Micropen^{TM} writing parameters should be carefully adjusted.

Direct-write of small circles and dots is a very interesting direction, and can be referred to chapter 9 for the discussion of future work.

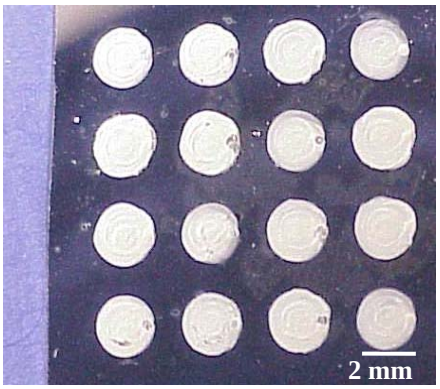

Fig. 5. 12 Optical pictures of small circles deposited by the Micropen^{TM}.

5.4 Summary

PZT thick films (6-70 μm in thickness) on alumina and silicon substrates have been fabricated by Micropen^{TM} direct-write technique for the first time. The thick films were annealed at low temperature (700 ºC), due to using a modified sol-gel process. In this process, commercial PZT powder was dispersed in a PZT sol-gel solution with different solids loading (~15, 20, 25, 30 vol%). The Micropen^{TM} writing parameter, "cross section", was crucial for the control of film thickness. The increment of powder concentration in the pastes increased film surface roughness. The microstructure revealed the film consisted of two different grains which came from the original commercial ceramic powder and the crystallized so-gel derived powder. The best dielectric and ferroelectric properties were obtained for a 16-μm film deposited using the 15 vol% paste on a silicon substrate. It had a dielectric constant of 870, dielectric loss of 4.1%, P_r of 12.2 $\mu C/cm^2$ and E_c of 27 kV/cm.

CHAPTER6 DEVELOPMENT OF 2-2 PIEZOELECTRIC CERAMIC/POLYMER COMPOSITES BY DIRECT-WRITE TECHNIQUE

6.1 Introduction and objectives

This chapter describes the direct-write of ceramic skeletal structures by Micropen™ for the development of ceramic/polymer composites. The writing material was a ceramic/binder based paste. This chapter is organized into three sections. The first section is an introduction to some topics relevant to the work of this chapter. The second section is the experimental procedures used in this work, including the preparation of pastes, the deposition of skeletal structures by Micropen™, the fabrication of composites, and the characterization of composites. The third section is the discussion of experimental results, such as the viscosity analysis of the pastes, the effects of writing parameters, and the properties of the composites.

6.1.1 The principle of medical ultrasound imaging

Piezoelectric transducers are devices capable of converting mechanical energy to electrical energy and vice versa[80]. They have various applications, such as hydrophones, non-destructive testing, energy harvesting, and medical ultrasound imaging.

The phenomenon utilized in these transducers is called “piezoelectricity”. The prefix “piezo” comes from the Greek word for pressure or mechanical force. Piezoelectricity refers to the linear coupling between applied mechanical stress and electric polarization (the direct piezoelectric effect), or between mechanical strain and applied electric field (the converse piezoelectric effect)[81]. Piezoelectricity was first discovered by Jacques and Pierre Curie in 1880 when they examined the generation of

electrical charge of quartz crystals under applied pressure. The direct and converse (indirect) effects can be defined by the equations in tensor notation and shown in Fig. 6.1 (a) and (b), respectively[81].

$$P_i = d_{ijk} T_{jk} \quad \text{(direct effect)} \tag{6.1-a}$$

$$S_{jk} = d_{ijk} E_i \quad \text{(converse effect)} \tag{6.1-b}$$

where P_i is the component of polarization, T_{ij} are the stress components, S_{jk} are the strain components, E_i is the applied electric field, and d_{ijk} are the piezoelectric tensor components, which is numerically identical for both effects. i, j and k represent the axes

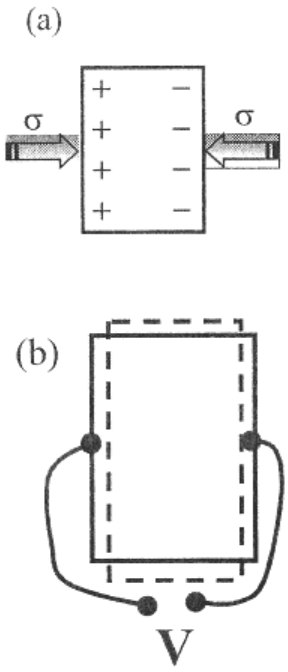

Fig. 6.1

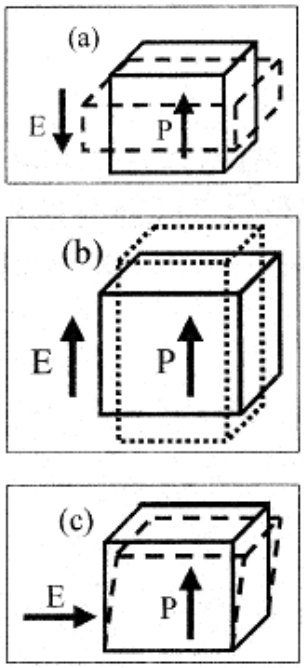

Fig. 6.2

Fig. 6.1 Schematics representing the piezoelectric effects: (a) direct and (b) converse[81].

Fig. 6.2 Schematic of piezoelectric effects in poled piezoelectric ceramics, where E and P represent electric field and polarization, respectively[81].
(a) transverse (b) longitudinal and (c) shear mode deformations.

of the coordinate system and vary from 1 to 3. Since the mechanical stress matrices are symmetrical, the third-rank tensor d_{ijk} can be simplified to d_{ij} by using matrix notation. In this form, d_{ij} is simply known as the piezoelectric charge coefficient. The equations become[80]:

$$P_i = d_{ij} T_j \text{ (direct effect)} \tag{6.1-c}$$

$$S_j = d_{ij} E_i \text{ (converse effect)} \tag{6.1-d}$$

where i varies from 1 to 3, and j varies from 1 to 6.

Three basic deformation modes of a piezoelectric material are illustrated in Fig. 6.2 [82].

The efficiency of a transducer is described by the electromechanical coupling factor, which is defined as following[80]:

$$k^2 = \frac{\text{mechanical energy converted to electrical energy}}{\text{input mechanical energy}} \tag{6.2-a}$$

or

$$k^2 = \frac{\text{electrical energy converted to mechanical energy}}{\text{input electrical energy}} \tag{6.2-b}$$

A very important application of transducers is in medical ultrasound imaging. Compared to other medical imaging techniques, such as X-ray, computed tomography (CT) and magnetic resonance imaging (MRI), the ultrasound imaging produces non-invasive, real-time, high resolution images of internal soft body tissue without use of potentially hazardous electromagnetic radiation, and this technique is also cost-effective and portable[83].

The ultrasound imaging transducers operate in a pulse-echo mode, in which both direct and converse piezoelectric effects are utilized. As shown in Fig. 6.3, the transducer transmits ultrasonic pulse into the body and also receives the faint echoes produced by the reflections from the internal structures. The reflection and transmission of acoustic signals at an interface between two media is the basis for the ultrasound imaging[84].

To detect smaller images, higher frequencies (f) are required to increase the lateral resolution, based on the relation between the wavelength (λ) and the velocity of sound (c)[85]:

$$c = \lambda f \qquad (\text{c} \approx 1500 \text{ m/sec in the human body}) \tag{6.3}$$

When the frequency of ultrasound is increased, the wavelength decreases, thus increasing the lateral resolution of transducers. Diagnostic ultrasound for common medical imaging uses frequencies between 2 - 20 MHz. Lower frequencies show poorer resolution but penetrate deeper into tissue. On the other hand, higher frequency ultrasound displays more detail with better resolution but less depth penetration. The operating frequency ranges for ultrasound imaging is listed in Table 6.1, depending on the organs to be diagnosed[86, 87]. The clinical applications are expanding from the range of 1-30 MHz to higher frequencies (20-200 MHz).

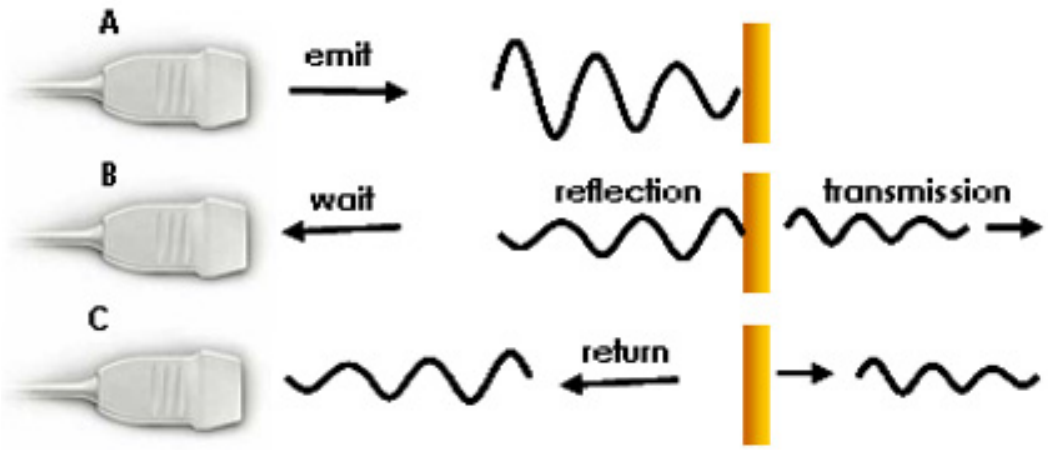

Fig. 6.3 Medical ultrasound transducers operate in a pulse-echo mode[88].

Table 6.1 The operating frequency ranges for different ultrasound imaging applications[86,87].

Frequency range	Clinical applications
2-5 MHz	abdominal, obstetrical, cardiological studies
5-7.5 MHz	pediatric, peripheral vascular studies
10-30 MHz	intravascular, intracardiac and eye studies
20-200 MHz	dermatology, gastrointestinal tract, the arterial walls, anterior chamber of the eye

6.1.2 Material aspects for medical ultrasound transducers

The overall performance of an ultrasonic system is mainly determined by the transducer characteristics. A transducer normally consists of three parts: active layer, matching layer and backing layer. The active layer is generally made of piezoelectric materials, which play an important role in transducer performance.

The primary requirements for the piezoelectric materials in ultrasound transducers are illustrated in the following[89]: (a) High longitudinal electromechanical coupling to efficiently converting the transducer's electrical energy to mechanical energy, and low planar coupling (k_p) to avoid energy dissipation in the planar direction. Since in the diagnostic applications, only longitudinal ultrasonic waves are used, the thickness mode coupling factor (k_t) should be high. (b) Acoustic impedance close to that of tissue ($Z \approx 1.5$ MRayls). Thus the acoustic waves in the transducer and tissue couple well during transmission and reception. (c) High piezoelectric charge coefficient (d_{33}) to have a good transmission (sending) capability. (d) Reasonably large dielectric constant ($K \geq 100$) to obtain electric impedance compatible with the driving and receiving electronics. (d) Low dielectric loss ($\tan\delta$) to minimize signal energy loss. (e) Low mechanical quality factor (Q_m=2-10) to obtain a good sensitivity and a broad bandwidth. A lower value of Q_m indicates a higher mechanical loss, which decreases the ringing of the transducer, thus increasing the axial resolution.

The normal four choices of piezoelectric materials available for medical imaging transducers are: polycrystalline ceramics, piezoelectric polymers, ceramic/polymer composites and single crystals. The advantages and disadvantages of these materials are presented in Table 6.2[90].

As shown in the Table 6.2, the conventional polycrystalline ceramics only partially meet these requirements for medical imaging transducers. For example, lead zirconate titanate (PZT) is a widely used piezoelectric ceramic for transducers due to its excellent electromechanical properties. However, its major drawback is the high acoustic impedance (Z>30 MRayls). PZT is also brittle and non-flexible as a ceramic material. Also, lead-based materials are unhealthy. In contrast, piezoelectric polymers provide low acoustic impedance (Z≈4 MRayls), and are flexible and conformable to any shape. But their low electromechanical coupling (k_t<0.3) and high dielectric loss degrade transducers sensitivity, and their low dielectric constants (K≈10) places severe demands on the transmitter and receiver electronics.

The main advantages of single crystals (such as $Pb(Zn_{1/3}Nb_{2/3})O_3$-$PbTiO_3$ (PZN-PT) and $Pb(Mg_{1/3}Nb_{2/3})O_3$-$PbTiO_3$ (PMN-PT)) over polycrystalline ceramics are the very high longitudinal electromechanical coupling factor (k_{33}=0.90-0.95) and piezoelectric charge coefficient (d_{33}>2200 pC/N). In contrast, the commonly used piezoceramic PZT has d_{33} of ~600 pC/N and k_{33} of ~0.75. The single crystals with those superior properties can provide better sensitivity and bandwidth for medical imaging applications. Large PZN-PT single crystal was initially reported by Kuwata in 1982, and the first commercial single crystal transducers was released by Philips in 2004[91]. During the past several years, scientists have made big progress in crystal growth techniques, optimizing material properties and fabrication various types of single crystal devices. However, the fabrication of those materials is still expensive, and one of the drawbacks is the large wafer-to-wafer variation of dielectric constant and d_{33}. Further investigation is still ongoing to develop cost-effective mass production for single crystals.

Since the early 80s, a new type of materials, PZT ceramic/polymer composites, has drawn increasing attention in the field of medical imaging. Because they combine the advantages of both ceramics and polymers, including higher k_t than those of the ceramics, much lower acoustic impedance, a wide range of dielectric constants and low dielectric and mechanical losses, which lead to higher transducer sensitivity and improved image resolution[92]. In addition, there are also investigations on single crystal/polymer 1-3 composites, in order to take advantage of the high k_{33} of single crystals. Those composites had k_t of ~0.8-0.85, mechanical quality factor (Q_m) of 10-20, and d_{33} similar to the d_{33} of single crystal (listed in Table 6.2)[93,94,95].

In addition to the above four types of materials, the relatively new study directions for high-frequency medical imaging (20-200 MHz) are: fine-grain ceramics, lead free materials[96,97,98] and PZT thick films[99].

Table 6.2 Comparison of materials parameters for piezoelectric ceramic, polymer, composites and single crystal [90,93,94,95].

Parameter	Polycrystalline ceramic (PZT)	Polymer (PVDF)	Single crystal (PZN-PT)	PZT ceramic/polymer composite	PMN-PT single crystal/polymer composites
Acoustic impedance (MRayls)	30 (-)	4 (+)	30 (-)	4-25 (can be tailored) (+)	Can be tailored (+)
Coupling factor	0.5-0.7 (+)	0.1-0.3 (-)	0.9-0.95 (+)	0.5-0.7 (+)	0.8 (+)
d_{33} (pC/N)	500-600 (+)	30-50 (-)	>2000 (+)	500-600 (+)	>2000 (+)
Dielectric constant	200-5000 (+)	6-10 (-)	4000-7500 (+)	Proportional to ceramic vol% (+)	1000-5000 proportional to single crystal vol% (+)
Dielectric loss	0.02 (+)	0.25 (-)	0.02 (+)	0.02-0.03 (+)	0.01 (+)
Cost and ease of fabrication	Cheap (+)	Expensive (-)	Very expensive (-)	Medium (+)	Very expensive (-)

A (+) sign means the property is an advantage, a (-) sign means the property is a disadvantage when used for medical imaging transducers.

6.1.3 Composite design considerations

One important advantage of piezoelectric ceramic/polymer composites is that their properties can be easily tailored by changing the connectivity of the two phases, the ceramic volume fraction in the composite and the aseptic ratio of ceramic element. The main design considerations for medical ultrasound transducers are as following:

6.1.3.1 Connectivity patterns

The concept of connectivity, or microstructural arrangement of the component phases in a composite, first developed by Newnham *et. al.*, is a critical parameter for the electromechanical performance of the composites[100]. Fig. 6.4 illustrates the basic ten ways of connecting the two phases. The first digit refers to the number of self-connected (or continuous) directions for the piezoelectric phase, and the second digit is used for the polymer. For example, 2-2 connectivity means the ceramic and polymer phases are both continuous in two dimensions. 1-3 composites consist of piezoelectric rods embedded in a polymer phase. For medical imaging, the most commonly used composites are 2-2 and 1-3 composites, due to their good electromechanical properties and feasibility to fabricate.

6.1.3.2 Ceramic volume fraction

The volume fraction of ceramic in a composite plays an important role in determining the properties of composites. Fig. 6.5 (a) indicates the transmit/receive responses for varying ceramic volume fractions in 1-3 composites evaluated by finite element analysis[101]. The modeling results show that higher volume fractions produce a higher transmission response, while higher reception occurs at lower volume fractions. For the medical ultrasound transducers, which act both as transmitters and receivers

operating in pulse-echo mode, the volume fraction is generally kept between 20-60 vol% in order to maintain a good transmitting output and receiving sensitivity[102].

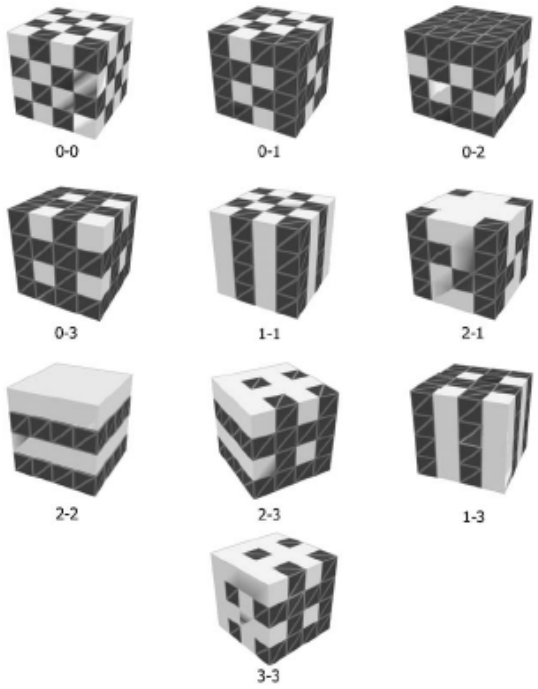

Fig. 6.4 Connectivity families for composites[100].

6.1.3.3 Aspect ratio

Aspect ratio of thickness to width of ceramic element plays a key role in the electromechanical properties of composites. In the following some examples are given supporting this fact.

The thickness coupling factor (k_t) is related to the interaction between the thickness and lateral vibrational modes. The lateral resonance waves (called "lamb waves") generate from the periodicity of the composite structure. W.A. Smith has done extensive studies on 1-3 composites and the general criterion is the periodicity of the composite structure must be sufficiently fine compared to the composite thickness[103]. It

was suggested that to avoid lateral resonance waves between the ceramic phases, the composite thickness should be larger than the pitch (the distance between the center of two adjacent ceramic elements), namely the sum of the widths of one ceramic and one polymer phases. Generally, the thickness-to-width aspect ratio of the ceramic pillars in 1-3 composites should be approximately greater than 3 to keep the ideal shape of the pulse response when used as transducers[104].

For 1-3 composites, D. Hall's studies showed that for volume fractions greater than 40 vol%, there was no obvious effect of the aspect ratio on k_t; for volume fractions less than 40 vol%, k_t started decreasing for lower aspect ratios[101].

For 2-2 composites, k_t was calculated for the first time by Y. Shui as a function of both ceramic volume fraction and aspect ratio[105]. Fig. 6.5 (b) demonstrates that in their study, k_t fell dramatically for a small aspect ratio (t/d) on decreasing ceramic volume fraction, and for t/d >4, the drop would be negligible. Here, t is the composite thickness, and d is the pitch. It was also found that k_t reached its maximum value when the thickness mode was completely decoupled from any lateral modes.

The theoretical studies by R. Lerch gave less strict requirement on aspect ratio that the thickness-to-width ratio of PZT bars (t/w) needs to be larger than 1.7 to keep high electromechanical coupling and pure longitudinal resonance[106].

6.1.3.4 Composite thickness

The resonant frequency of a transducer (f_r) is determined by its thickness (t) given by the equation[90]:

$$f_r = \frac{v}{2t} \tag{6.4}$$

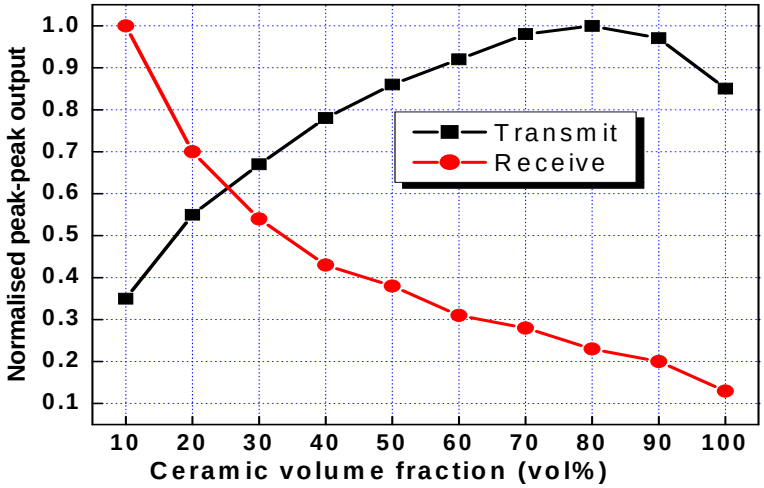

(a)

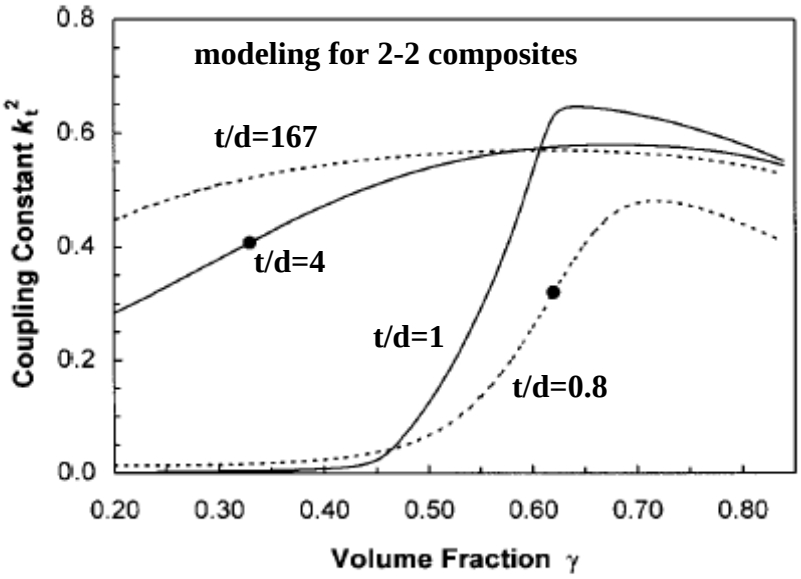

(b)

Fig. 6.5 (a) Transmit/Receive responses as a function of ceramic volume fraction (modeled for 1-3 composites)[101]. (b) Magnitude of k_t^2 as a function of ceramic volume fraction at four aspect ratios (modeled for 2-2 composites)[105].

where v is the sound velocity in the composite transducer. It is clear that the higher the frequency, the thinner the composites. For example, a 110-μm thick 2-2 composite had a resonance frequency of 20 MHz, while an 80-μm thick composite had a resonance frequency of nearly 30 MHz [107]. Therefore, for higher-frequency medical imaging applications, thinner composites with small ceramic elements width are desirable.

6.1.4 Composite fabrication techniques

Currently, PZT/polymer composites for medical ultrasound imaging are commercially fabricated by "dice and fill", injection molding and lost mold techniques[104,108]. In addition, PZT fibers (5-200 μm in diameter) extruded from spinneret holes have also been used a lot to fabricate fiber/polymer composites in industry[87].

Fig. 6.6 (a) shows the basic principle of the "dice-and-fill" approach, where ceramic elements are cut from a plate of piezoelectric ceramic or single crystal and then back-filled with a polymer. Recently, for high-frequency applications (>20MHz), several modified dicing techniques have been developed[109, 110]. Fig. 6.6 (b) shows a method called "interdigital pair bonding (IPB)" for fabricating 2-2 or 1-3 composites[111, 112]. Identical parallel grooves are diced on a pair of ceramic sheets, and the grooves are slightly wider than the ceramic stripes. The two ceramic sheets are then impregnated with epoxy and interdigitally inserted. Finally, the epoxy is cured and the top and bottom surfaces are lapped away to form the 2-2 composites. IPB method allows fabricating a composite structure with a pitch on the order of the blade thickness. Another more complicated method, "interdigital phase bonding" (IPhB), allows fabricating a composite structure with a pitch less than a dicing saw blade thickness[113]. In addition, based on the dicing technique, a sophisticated 180-element 30-MHz linear array was manufactured

using 1-3 composites with a dicing width less than 12 μm[114], and a 64-element 35-MHz linear array was developed using 2-2 composite with a 25 μm pitch made by 2-step dicing[115]. Another available fabrication method for finely featured composites is tape casting[107]. This method involves screen printing carbon black ink on thin sheets of green PZT tapes (20-50 μm in thickness). Followed by stacking tapes to form composites, the carbon is removed by heat treatment and backfilled with polymer. The ceramic dimensions achieved by the above composite processing methods for high-frequency medical imaging applications (>20 MHz) are summarized in Table 6.3. Other possible manufacturing techniques include laser cutting[116], thermoplastic green machining[117], micromaching[118], and so on.

The disadvantages of the above techniques are not suitable for building novel and complex designs within a short period of time. For example, for injection molding, it is difficult to modify the design of composites because the molds are expensive and require a long time to fabricate. In recent years, the fabrication of composites by direct-write techniques has received increasing attention. Extensive research has been devoted to fused deposition of ceramics (FDC) [119,120], robocasting[121], stereolithography[122] and ink-jet printing[123]. These techniques allow depositing materials only where needed, eliminate processing steps such as cutting and mold-making, and enable rapid-prototyping of novel or complex patterns for cost-effective small-lot production[124].

Another promising direct-write approach is the Micropen™ technique, which has been described in detail in the previous chapters. Although the Micropen™ direct-write has proven to be well suited for the deposition of thick films and multilayer devices, its capability of creating micro-scale three-dimensional (3D) structures has not been reported.

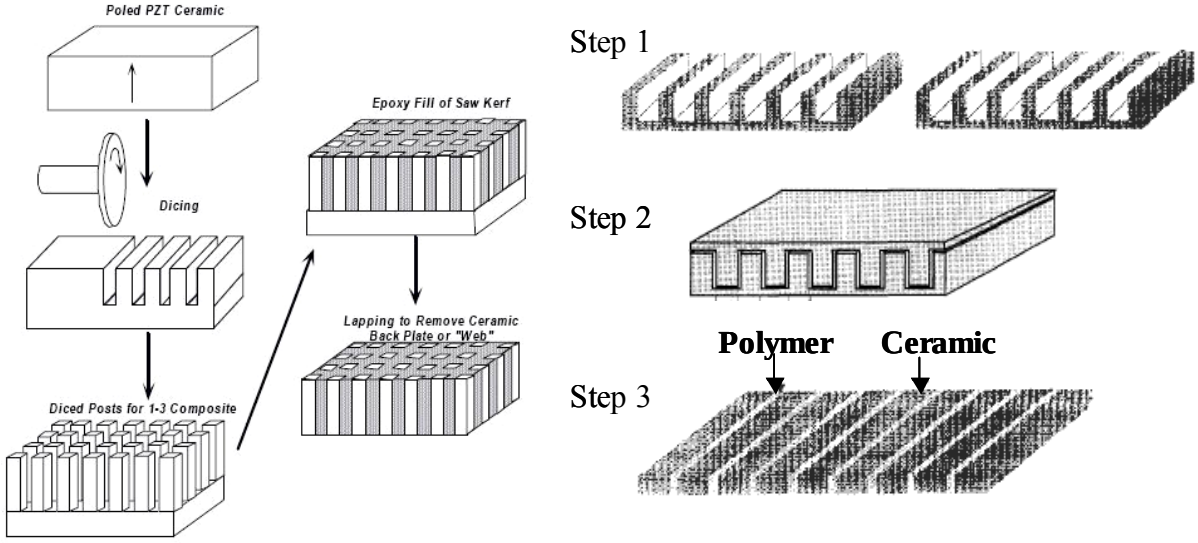

(a) (b)

Fig. 6.6 (a) Schematic drawing of "dice-and-fill" method[109]. (b) Schematic drawing of IPB method[111].

Table 6.3 The dimensions achieved by different methods for high-frequency medical imaging applications (>20 MHz).

Fabrication Method	Dicing saw blade width (μm)	Ceramic phase width (μm)	Polymer phase width (μm)	Composite thickness (μm)	Resonance frequency (MHz)
IPB[111]	40	36	4	53	32
IPhB[113]	50	15	10	~50	>30
Dicing[114]	~12	~45	~12	47	30
Dicing[115]	13	11	14	50	35
Tape casting[107]	/	22	5	80	25

6.1.5 Objectives

The objectives of this chapter are the following:

(1) To demonstrate the feasibility of fabricating PZT/polymer 2-2 composites (300-400 μm in thickness) using Micropen^{TM} direct-write, for transducers including medical imaging applications.

(2) To design composites with different volume fractions.

(3) To study the effects of Micropen^{TM} deposition parameter on writing quality and line dimensions.

(4) To use the smallest possible pen tip which can be written with a suitable paste having the highest ceramic loading.

(5) To fully characterize the microstructure, dielectric, piezoelectric and electromechanical properties of the fabricated composites.

6.2 Experimental Procedures

6.2.1 PZT pastes preparation

6.2.1.1 Powder Coating

The PZT powder used in our experiments was commercial TRS 610 powder (TRS Ceramics, Inc., PA), which exhibits an average particle size of ~1.5 μm, and a surface area of ~1.5 m^2/g. The PZT powder was coated with a surfactant, stearic acid (Fisher Scientific, PA, laboratory grade), in order to increase ceramic powder loading with lower paste viscosity[125]. The coating procedure was as follows: first, the commercial PZT powder was dried in an oven at 90ºC overnight. Then, 3 g of stearic acid powder was dissolved in 100 ml of toluene. Afterwards, 100 g of dried PZT powder and the acid solution were poured into a Nalgene bottle (250 ml), with 8 pieces of ZrO_2 milling media (1 cm in diameter) added to improve mixing, ball milled for 4 hours. The mixture was then filtered in hood under vacuum, using fine filter paper (Fisher Scientific, PA). The powder was dried in the fume hood overnight, and finally dried in an oven at ~100ºC for 3-4 h.

6.2.1.2 Pastes preparation

As mentioned in the introduction, in order to obtain high aspect ratio of PZT line (height/width), high-concentration as well as high-viscosity pastes are required for Micropen deposition. Thus, a PZT paste was prepared in a similar method to that used in the work of S.L. Morissette, V. Tohver, and M. Allahverdi[22-24]. PZT pastes with 35, 40 and 45 vol% solids loading were prepared for the viscosity measurements. In this chapter, only the 35 vol% paste was used for preparing composites. To prepare the paste, 5 vol% ethyl cellulose powder (Sigma Chemical Co., MO) was first dissolved in α-terpineol

(Sigma Chemical Co., MO), and then the coated PZT powder was gradually added into the terpineol-ethyl cellulose solution. The 35 vol% PZT paste contained 24.87 g coated PZT powder, 5.30 g α-terpineol and 0.34 g ethyl cellulose (as binder). After magnetic stirring for 20 min, the mixture was three-roll milled for 20 min to break agglomerates, by which the paste uniformity was improved. Then, the paste was transferred into a syringe and centrifuged for 2-5 min to eliminate air bubbles generated during the preparation and handling. Finally, the syringe was loaded to the Micropen™ for deposition.

6.2.1.3 PZT discs preparation

The pressed green PZT discs were used as base for the deposition of the desired skeletal structures by Micropen™. A 20wt% polyvinyl alcohol (PVA) (Celanese Ltd., Texas) water solution was prepared as the binder system for pressing PZT discs. The commercial PZT powder was ground using a mortar and pestle while gradually adding the PVA solution dropwise. 0.14 g of PVA solution was added for 1 g of PZT powder (uncoated). The amount of binder (2.6 wt%) in the discs was about the same as that in the PZT paste prepared for the Micropen™ deposition. Then the powder was sieved through a No.70 sieve (USA standard testing sieve, opening micron 212 μm) to remove large agglomerates. Finally, 3 g of sieved powder was pressed as a disc using a 1-inch diameter die, at a force of 3 tons (~ 58 MPa pressure). Higher pressure was not applied here, in order to allow the PZT discs to shrink ~ 20% in the radial direction, which is similar to the shrinkage of the PZT paste prepared for the Micropen™ deposition with the 35vol% ceramic loading.

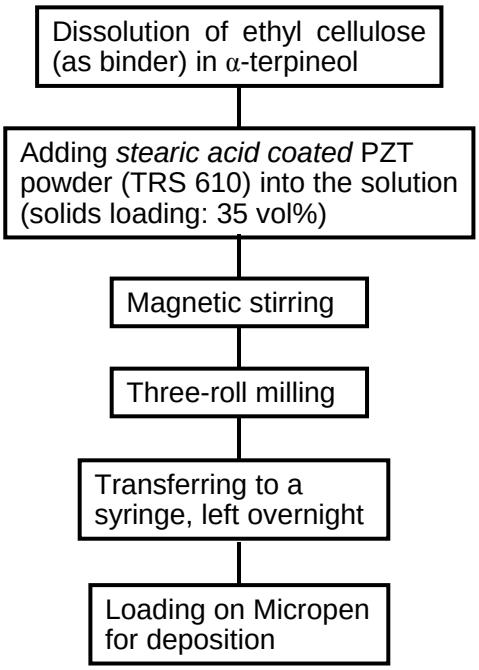

Fig. 6.7 Flow diagram for the PZT paste preparation.

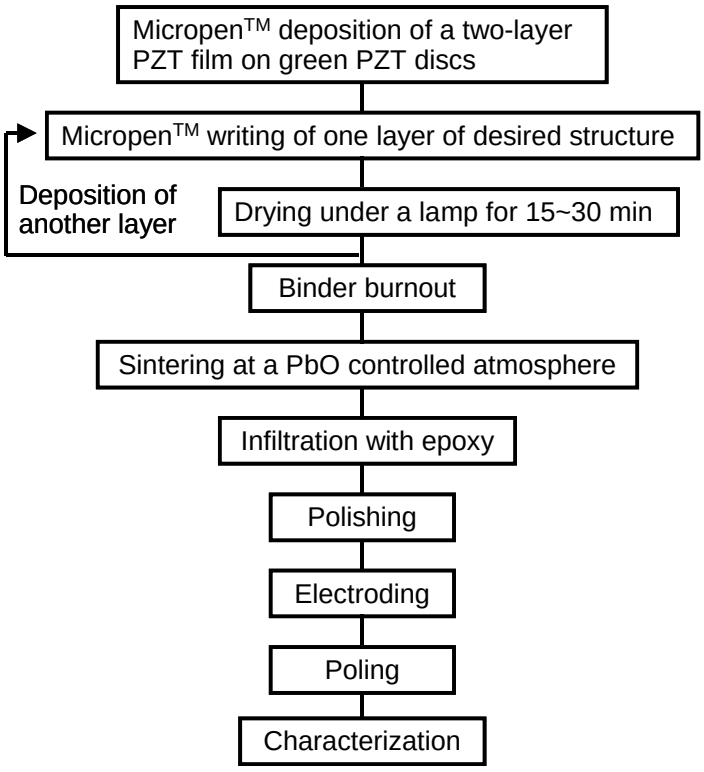

Fig. 6.8 Flow diagram for the Micropen™ deposition and composite fabrication.

6.2.2 Deposition of the ceramic skeletal structures

The PZT paste was used as a writing material for the Micropen^{TM} direct-write technique. As shown in the flow diagram in Fig. 6.8, prior to depositing the PZT skeletal structures, a two-layer film (~60 μm thick) was deposited on the green PZT disc in order to enhance the attachment between the deposited structure and the disc and to promote co-densification during sintering.

The PZT skeletal structure was designed by AutoCAD software, and deposited in a layer-by-layer build sequence to obtain the desired thickness. Underlying layers were dried under a normal table lamp (120 V, 100 W) for 15-30 min before direct-writing on top of them. During this time, the pen tip was kept within a few drops of PZT pastes to avoid drying or blocking. Before writing the next layer, the pen tip was first gently cleaned by fine tissue, and then its height and position were carefully re-adjusted.

Different sizes of pen tips have been used in this study (250, 150 and 100 μm in inner diameter), to obtain different PZT line widths and aspect ratios. The sizes of different pen tips were obtained from the OhmCraft company, and were also confirmed using an optical microscopy (ZEISS, Axioskop 40, Hitech Instruments, Inc., PA). For a specific pen tip, the Micropen^{TM} writing parameters were adjusted accordingly to achieve the required dimensions for the structures of interest. For example, using a 100-μm pen tip, the writing parameters optimized for the 35vol% paste are presented in Table 6.4.

Table 6.4 The Micropen™ parameters for the direct-write of skeletal structures (using three pen tips and the 35vol% paste).

Pen size (μm)	Cross section (mil^2)	Writing speed (mil/s)	Writing force (mg)	Trigger height (mil)	Lift force (mg)	Lift speed (mil^3/s)	Term volume (mil^3)	Term speed (mil^3/s)	Burst volume (mil^3)	Burst speed (mil^3/s)
250	40	25	5	0.5	5	10000	50000	100000	0	500
150	15	50	2	0.3	5	10000	40000	50000	0	500
100	20	25	2	0.8	10	10000	150000	200000	0	500

6.2.3 Composite fabrication

6.2.3.1 Binder Burnout (BBO) and sintering

As shown in the Fig. 6.8 flow diagram, after deposition, the green PZT skeletal structures were debinded in air at 550°C for 1 h, with 1°C/min heating rate and 3°C/min cooling rate. The setup was as follows: a deposited structure was put in an alumina crucible on top of a coarse ZrO_2 powder bed, which can ease the binder removal from the bottom of the sample. Relatively less holding time and faster heating rates were applied here, mainly because of less amount of binder in the paste and a finer structure deposited by Micropen™.

After binder removal, the ceramic parts were sintered at 1250°C for 1 h with 3.5°C/min heating rate and the same cooling rate, in an excess-PbO atmosphere. The sintering setup was as follow: the sample was placed on an alumina sintering disc with lead source underneath the disc. A Platinum (Pt) sheet was placed between the sample and alumina disc, in order to avoid reaction between PZT and alumina. 4 g of lead source ($PbO+ZrO_2$, 1:1 molar ratio) was used for a crucible (~101 cm^3 in volume) to control lead loss of samples.

6.2.3.2 Polymer infiltration

After sintering, the ceramic structures (including the PZT discs) were infiltrated with polymer. The epoxy used was Epotek 301 (Epoxy Technology, Inc., MA). Two different components of the epoxy were mixed in the weight proportion recommended by the manufacturer. After magnetic stirring for 20 minutes, the epoxy was poured into a small plastic dish containing the sintered PZT skeleton. Vacuum de-airing was performed by cycling between atmospheric pressure and ~ -10 kPa several times until no bubbles generated from the samples. Then the samples were left in the vacuum chamber for 30 minutes under ~ -10kPa, followed by curing the epoxy at room temperature overnight.

6.2.3.3 Polishing

Upon curing the polymer, the next step was to polish the samples to the desired thickness. There were two challenges here: one was to reach a much smaller thickness (300-400 μm) compared to that of the composites fabricated by FDC or Robocasting techniques (1-2 mm); another one was to achieve flat and parallel top and bottom surfaces with minimal thickness variation, which is crucial to eliminate spurious thickness mode vibration for the composites. Therefore, more careful polishing and handling were required for the samples deposited by the Micropen^{TM}.

The samples were polished in the following way. A polishing die system was used, and the sample was glued to the die using a thin layer of dental wax. Coarse SiC paper (LECO Corporation, MI, 400 grit) was first used to remove the PZT base and the excess polymer on the ceramic surfaces. Then, fine SiC paper (1200 grit) was used to further polish the samples until the ceramic phase was exposed on both sides. Careful observation of the ceramic exposure and good control of the pressure on the die during

polishing were helpful to achieve polished samples with uniform thickness. In addition, gentle handling was required because the samples were easy to break along the ceramic-polymer interface when the thickness decreased.

6.2.3.4 Electroding and poling

Electroding the composites was done by gold sputtering for 4 min on both sides. The edges of electroded samples were slightly polished to remove the excess gold. Poling was accomplished in a silicon oil bath at 50 °C with 30 kV/cm electric field intensity for 15 min. Higher poling temperatures and longer duration did not improve the properties, but may soften the polymer in the composites.

6.2.4 Characterization of the pastes and deposited structures

The viscosities of the 35, 40 and 45 vol% PZT pastes were measured with an AR1000-N rheometer (TA instrument) with a concentric cylinder, having conical end geometry.

Thermogravimetric analysis (TGA) of the coated PZT powder and the 35 vol% PZT paste was performed on Perkin-Elmer TGA7, in the range of 50-600ºC at a heating rate of 10ºC/min in air. For the coated PZT powder, the purpose of TGA was to check the adsorption of the stearic acid on the powder surface; while for the paste, was to check the amount of ceramic solids loading and the temperature ranges of the heat treatment process.

Line width and height of one-layer as-deposited PZT skeletal structure were measured with a profilometer (alpha-step 200, TENCOR Instruments). The purposes were to gain an idea of the deposited dimensions by the Micropen^{TM} technique, as well as to study the effects of writing parameters on the dimensions.

The dimensions of one-layer deposition of PZT structure after binder burnout (BBO) and after sintering were measured by the profilometer, with the purpose of studying the sintering shrinkage. And an optical microscopy (ZEISS, Axioskop 40, Hitech Instruments, Inc., PA) was also used to observe the PZT structures.

The fracture surface of sintered ceramic structures was examined by field emission scanning electron microscopy (LEO-ZEISS, Gemini 982) to study the sample's microstructure.

6.2.5 Composites characterization

The densities of the composites and PZT discs were evaluated by the Archimedes method. The volume fraction of ceramic in the composites was calculated using the mixing rule and the following equation:

$$\text{PZT vol\%} = \frac{\rho_{composite} - \rho_{polymer}}{\rho_{PZT} - \rho_{polymer}} \tag{6.5}$$

where $\rho_{composite}$, $\rho_{polymer}$, and ρ_{PZT} are the densities of composites, polymer and pure PZT, respectively. The densities of bulk PZT ceramic and polymer were referred as 7.77 g/cm^3 and 1.08 g/cm^3, respectively.

The relative dielectric constant (K) and dielectric loss (tanδ) of composite samples were determined with an impedance grain/phase analyzer (HP4194A, *Hewlett Packard)* at a frequency of 1 kHz at room temperature.

The piezoelectric charge coefficient (d_{33}) was measured with a Berlincourt d_{33}-meter at 100 Hz (Model CPDT 3300, Channel Products Inc., Chesterland, Ohio). The reported d_{33} values were an average of the composites since the probe covered the entire area of the samples.

The electromechanical coupling factors (k_t, k_{31}, k_p) were determined by the IEEE standard [126], calculated from the series (≈resonance) and parallel (≈anti-resonance) frequencies of the impedance. The equations are as following:

$$k_t^2 = \frac{\pi}{2}\frac{f_s}{f_p}\tan\left(\frac{\pi}{2}\frac{f_p - f_s}{f_p}\right) \tag{6.6}$$

$$k_p^2 = \frac{f_p - f_s}{f_s}\left[\frac{R_1^2 - (1-\sigma^2)}{1+\sigma}\right] \quad \text{(for a PZT disc)} \tag{6.7}$$

$$\frac{k_{31}^2}{1-k_{31}^2} = \frac{\pi}{2}\frac{f_p}{f_s}\tan(\frac{\pi}{2}\frac{f_p - f_s}{f_s}) \quad \text{(for a composite sample)} \tag{6.8}$$

$$k_{31}^2 = \frac{k_p^2(1-\sigma)}{2} \quad \text{(for a PZT disc)} \tag{6.9}$$

where f_s and f_p are the series and parallel resonance frequency, respectively. k_t and k_p are the thickness and planar coupling factor, respectively. σ is Poisson's ratio (for PZT $\sigma \approx 0.31$), and R_1 is a constant proportional to σ (here $R_1 \approx 2.05$). In addition, the 31 mode coupling factor (k_{31}) of a rectangular composite sample was calculated from the f_s and f_p of the lowest frequency resonance mode. The k_{31} of a PZT disc was calculated from the k_p using the equation (6.9).

The mechanical quality factor (Q_m) of the devices was evaluated by the bandpass method[127], using the relation:

$$Q = \frac{f_L}{\Delta f} \tag{6.10}$$

where f_L is the frequency having the highest admittance ($|Y|_{max}$), and Δf is the width of frequency curve at $0.707|Y|_{max}$.

The resonance method was also used to evaluate d_{33} using the following relation[128]:

$$d_{33} = \sqrt{\frac{\varepsilon_{33}^T k_{33}^2}{4\rho f_p^2 l^2 (1-k_{33}^2)}} \tag{6.11}$$

where ρ, l and ε_{33}^T are the density, thickness and permittivity of the composite, respectively, and k_{33} is longitudinal coupling factor, here assume k_{33} approximately equals to k_t for the composite samples.

6.3 Results and Discussion

6.3.1 Viscosity study and thermal analysis of the PZT pastes

Fig. 6.9 depicts the apparent viscosity as a function of shear rate for the 35, 40 and 45 vol% PZT pastes. It is clear that all three pastes exhibited shear thinning behavior, and the viscosity increased with increasing solids loading in the shear rate range studied here. Shear thinning (or likewise shear thickening) behavior can be described by an empirical power law equation as[129]:

$$\eta_a = K\dot{\gamma}^{m-1} \tag{6.12}$$

where η_a is the apparent viscosity, $\dot{\gamma}$ is the shear rate, K is the consistency index, and m is the power-law index, which indicates the departure from Newtonian behavior. If $m<1$, the equation describes shear thinning. From Fig. 6.9, it is seen that K increased from 13.3 to 77.3 and to 741.3 with increasing solids loading, while m values were approximately 0.5, 0.4 and 0.6 for the 35, 40 and 45 vol% pastes, respectively. The closeness of m values indicate that the degree of shear thinning for the three pastes were similar. In addition, as proposed by Dimos et al., the typical Micropen^{TM} writing range corresponds to high shear rates (20-85 s^{-1}), while the "settling range" corresponds to low shear rates (<1 s^{-1})[130]. For the 35 vol% PZT paste used in the Micropen^{TM} deposition, the viscosities were 45 and 2 Pa·s in the "settling range" (0.1 s^{-1}) and "writing range" (85 s^{-1}), respectively. The relative high viscosity values in the "writing range" and "settling range" indicate that this paste can be used for writing high definition patterns. For the pastes with higher solids loading (e.g. 40 and 45 vol%), although they exhibited higher viscosities, problems such as pen tip clogging were encountered. Therefore, the 35 vol%

paste was used in our current work, and the deposition using higher solids loading pastes was deferred to a future study (refer to Chapter 7).

TGA curves of the coated PZT powder and the 35 vol% paste are plotted in Fig.6.10. For the coated powder, it is found that approximately 1.3 wt% stearic acid (as a dispersant) was adsorbed onto the powder surface, which helped to avoid agglomerates. For the paste with 35 vol% loading, the 84 wt% residue at 600ºC was close to the calculated value (~81 wt%). In addition, the weight losses below 200ºC (~13 wt%) and between 200-400ºC (~3 wt%) were attributed to the solvent removal and the decomposition of the dispersant and binder, respectively.

6.3.2 Effects of "Cross Section" on PZT line dimension

To achieve uniform and consistent writing quality, various Micropen^{TM} writing parameters need to be optimized. For example, "cross section" of a printed line is one of the important parameters. It determines the amount of material delivered by a pen tip at a given writing speed, or can be simply defined as "cross section=line width × line height" for an ideally rectangular cross-sectional line.

Fig. 6.11 plots the variations of line width (LW), line height (LH) and actual cross section (ACS) as a function of "input cross section"(CS) (CS=5, 10, 15, 20, 25 and 30 mil^2, i.e. CS=3226, 6452, 9677, 12903, 16129 and 19355 μm^2). The test samples were one-layer deposition on glass slides, using a 100-μm diameter pen tip and the 35 vol% paste (writing speed=50 mil/s, writing force=10 mg). The actual cross section (ACS) was automatically calculated for the cross section of deposited lines by the profilometer.

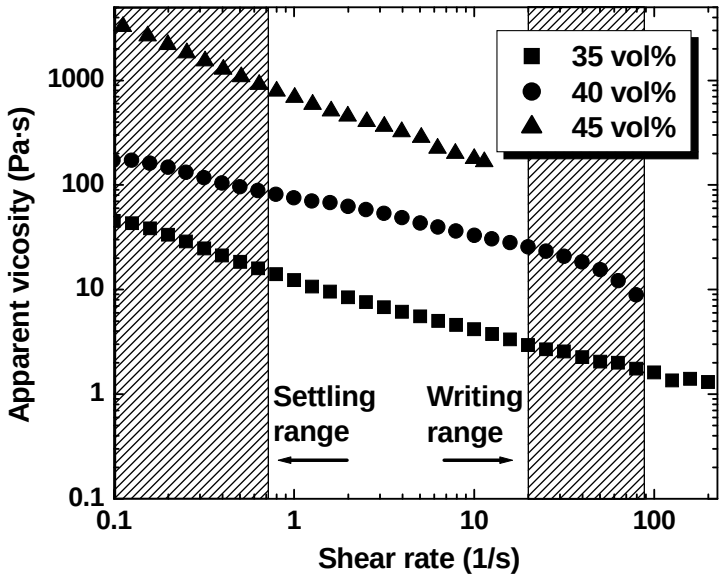

Fig. 6.9 The apparent viscosity as a function of shear rate for the three PZT pastes.

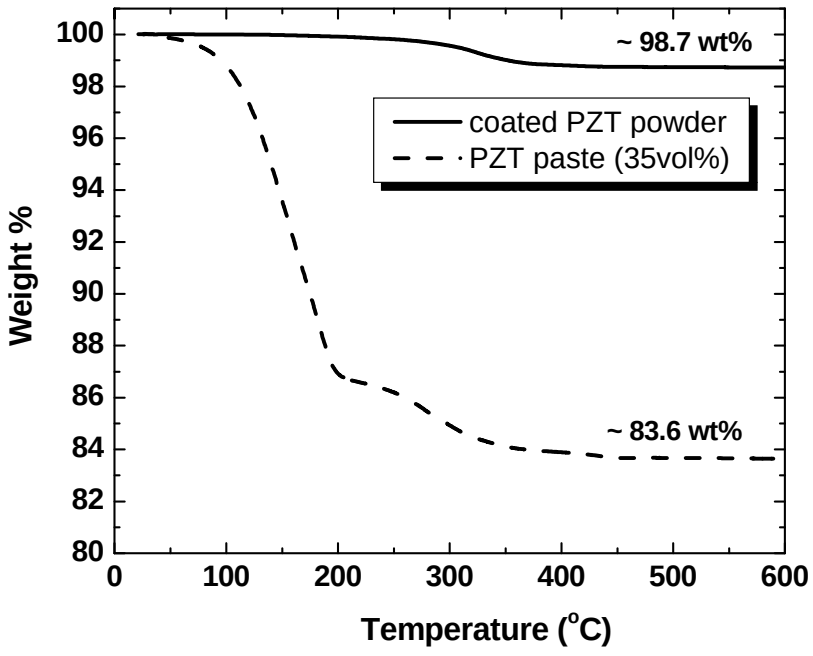

Fig. 6.10 TGA curves of the coated PZT paste and the 35 vol% PZT paste.

From Fig. 6.11, it is clear that LH, LW and ACS increased with increasing "input cross section" (CS). In addition, the results could be fitted using a linear model. The linear relationship can be expressed as $y = A + Bx$, where A and B give the slope and intercept values, respectively. In order to evaluate the validity of such linear models, correlation coefficient (R) was also calculated (the more R is closer to "1", the more the linearity). Using the method of least squares, the values of A, B and R for the three relationships were calculated and are listed in Table 6.5.

The nearly linear relation has been observed previously for thick films deposited by the Micropen^{TM} (refer to Chapter 5), namely the film thickness linearly increased with "cross section". It should be noted that the purpose of plotting Fig. 6.11 is to qualitatively analyze the effects of "input CS" on the line dimensions. Thus the values of A, B and R are not important. However, the significance of Fig. 6.11 is that the "cross section" in the line dimensional control in the Micropen^{TM} deposition is very important. In addition, line height (LH) increased at the expense of increasing line width (LW), which indicates that an optimal cross section should be chosen for a desired aspect ratio of PZT skeletal structures.

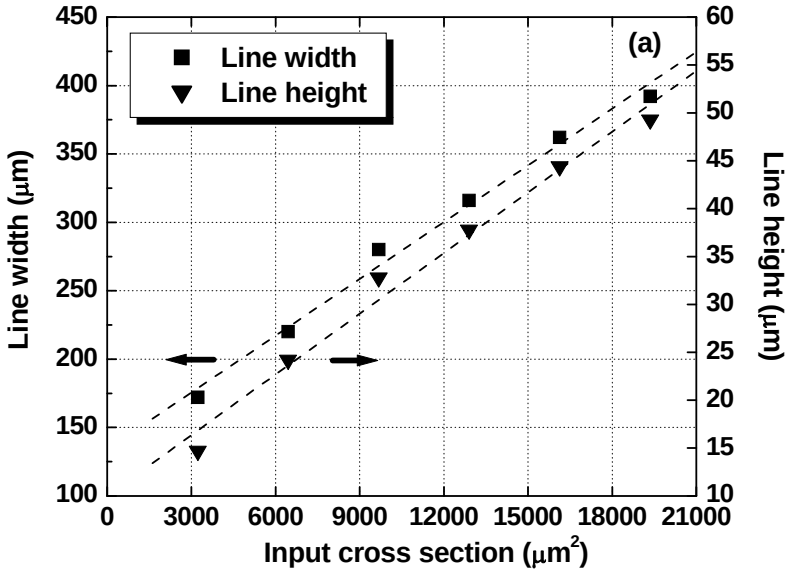

(a)

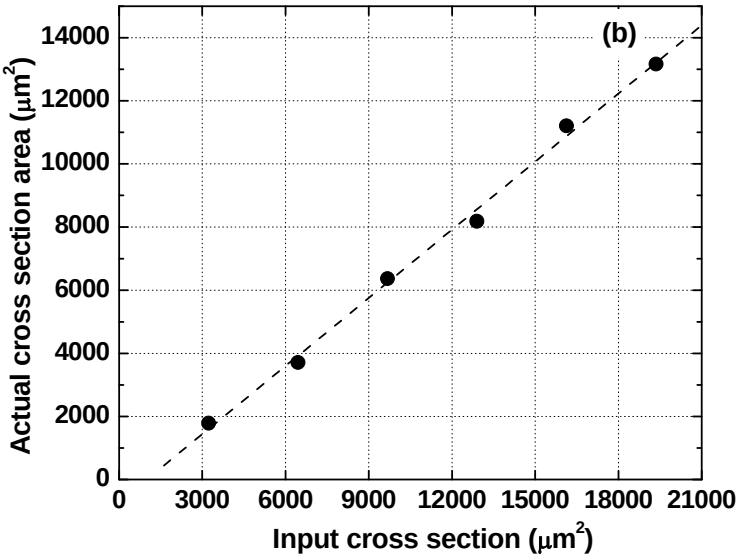

(b)

Fig. 6.11 The variations of (a) line width, line height and (b) actual cross section as a function of "input cross section".

Table 6.5 The values for A, B and R in the linear fitting for the three relationships (using a 100-μm pen tip and the 35 vol% paste).

Relationship	A (μm^{-1})	B (μm)	R
Input CS-LH	10.00	0.0021	0.9919
Input CS-LW	134.13	0.014	0.9953
Input CS-ACS	-716.47	0.72	0.9982

6.3.3 Microstructure of the sintered ceramic structure

Fig. 6.12 (a) and (b) show the FESEM micrographs of a representative sintered ceramic structure, which was a 5-layer PZT skeleton deposited using a 250-μm pen tip (main writing parameters were: "cross section"=20 mil^2, "writing speed"=25 mil/s). First, FESEM reveals the typical cross section of ceramic structures in Micropen^{TM} deposition. Similar to other solid freeform fabrication techniques, such a feature originates from the layer-by-layer direct writing of cylindrical materials. Secondly, layers were found to be sintered well with adjacent layers and no delamination was observed among layers after sintering. Thirdly, a fully densified ceramic microstructure was obtained with grain size of 2-3 μm. Finally, for this sample, the average values for one-layer thickness, the maximum line width and minimum line width were about 60 μm, 185 μm and 160 μm, respectively. The variations for the one-layer thickness, the maximum line width and minimum line width were about 6%, 7% and 6%, respectively. In general, deposited line dimensions are determined by a specific pen tip, paste viscosity and writing parameters.

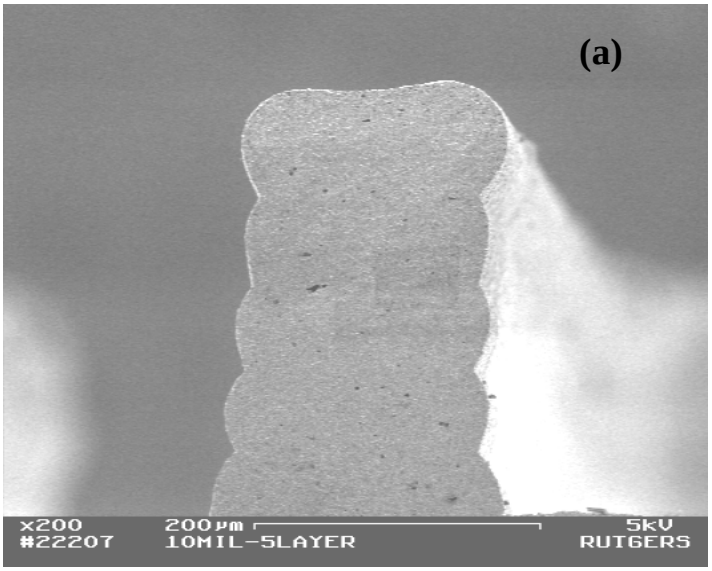

(a)

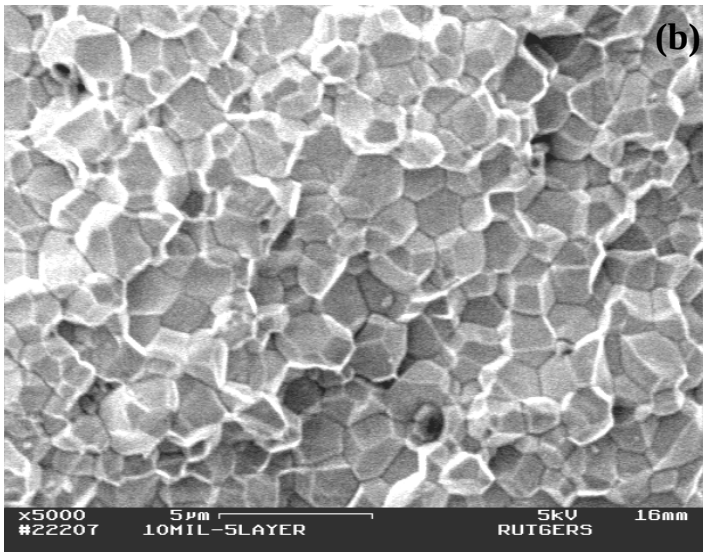

(b)

Fig. 6.12 FESEM micrograph of fracture surface of a sintered PZT plate (a) at low magnification and (b) at high magnification.

6.3.4 Deposition of the ceramic skeletal structures

Fig. 6.13 (a)-(c) show the optical pictures of as-deposited PZT skeletal structures of 2-2 composites, using three pen tips of 250, 150 and 100 μm, respectively. Smaller pen tips were used to achieve finer features and equal (or higher) aspect ratio (height/width), which are helpful to avoid lateral resonance waves (discussed in section 6.1.3). However, the dimensional variations of green PZT ceramic bars may become problematic when using smaller pen tips. This is mainly due to the clogging of pen tips, which could be improved by optimizing paste processing to reduce PZT powder agglomeration in pastes.

For the skeletal structures, a serpentine pattern was designed instead of separated lines, thus only having one line start and one end for the whole pattern. Because the Micropen^{TM} deposition exhibits relatively good consistency and uniformity during writing in the "stationary" state, but it is challenging to fully control material flow at line starts and ends in the "transient" state. The same design strategy has been used in FDC and robocasting techniques.

Compared to the deposition of thick films by Micropen^{TM} (Chapter 5), the following are important considerations for the deposition of 3D structures: (a) good control of line dimensions, (b) good control of line starts and ends, (c) higher height-to-width aspect ratio, and (d) writing more layers (e.g. 10-14 layers). To meet those requirements, it is important to optimize the writing parameters for high quality writing, especially for high quality line starts and ends. It is important to note that those parameters are interactive with each other and other variables such as the paste viscosity and uniformity are also affecting deposition conditions.

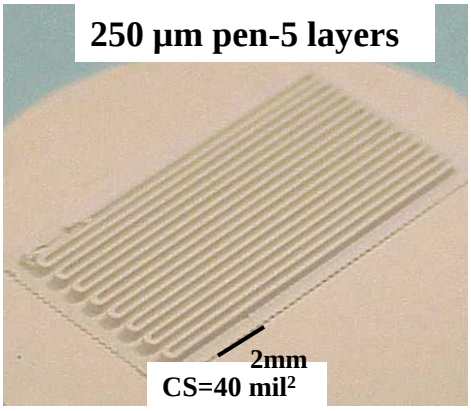

(a)

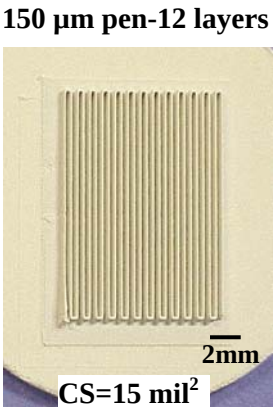

(b)

(c)

Fig. 6.13 Optical pictures of the as-deposited PZT skeletal structures using three pen tips (250 µm, 150 µm and 100 µm).

The writing parameters optimized for the deposition of the skeletal structures for composite A and B are listed in Table 6.4. "Cross section (CS)" is a parameter which should be set first, and is used during the entire writing process. "Cross section=20 mil^2" was chosen based on the required dimensions using a 100-μm pen tip. In detail, to obtain a 600-μm thick PZT structure after deposition, if 10 layers with one-layer height of ~ 60 μm (=3.2 mil) and width of ~ 150 μm (=6.0 mil) were written, then the cross section was calculated as $3.2 \times 6 \approx 20$ mil^2. Higher values of CS will increase PZT line height, but as discussed in section 6.3.2, line width will become bigger at the same time, which will result in lower aspect ratio (height/width) at a desired composite thickness.

In addition, a relatively slow "writing speed" (WS=25 mil/s) was chosen for writing fine structures. A small "writing force" (WF=2 mil) was used to obtain narrower lines with larger height. After choosing the above three parameters, other writing parameters (e.g. "trigger height", "lift force", "term volume") were optimized for high quality line starts and ends (please refer to the Micropen^{TM} manual for how to adjust those parameters).

Similar to other direct-write techniques, an attractive advantage of the Micropen^{TM} direct-write is the design flexibility using AutoCAD software, thus desired volume fractions can easily be created for the prototyping of composites. Another similarity is the layer-by-layer build sequence for depositing. However, a disadvantage for Micropen^{TM} is that the underlying layers have to be dried before depositing another layer. This is mainly because the liquid-based material needs to be dried to gain enough strength before writing on top of it. In contrast, in the FDC or robocasting techniques, the extruded materials become solid as soon as deposited and additional layers can take place

with no delay. Another difference for the Micropen^{TM} is that the pen tip needs to be readjusted before the deposition of next layer, because the automated motion in the z direction is not allowed. Associated with the above two features, the main problems encountered during deposition were: (a) the blocking of a pen tip during the waiting period for drying deposited layers, (b) the destruction of underlying layers when a pen tip moves on not fully dried layers, (c) misalignment between layers due to a slightly shift of pen tip when it moves to the next layer.

Furthermore, to achieve a successful deposition, a few other issues to which we should pay attention are: (a) to completely clean the three-roller mill to avoid contamination with other materials, (b) to avoid the switch of two chambers of Micropen^{TM} during deposition to maintain the writing continuity. In other words, a minor mistake will put the efforts of writing previous layers in vain. Therefore, not only the better control of processing procedures, but also great patience and carefulness were crucial for high quality of the 3D structures deposited by Micropen^{TM} direct-write.

6.3.5 Sintering shrinkage of the ceramic structure

Fig. 6.14 (a) and (b) show the ceramic skeletal structures after BBO and sintering of a representative composite (composite A), respectively. Composite A was deposited using a 100-μm pen tip, with "cross section"=20 mil^2 (as-deposited picture is shown in Fig. 6.13 (c)).

The study for a one-layer deposition showed that the sintering shrinkage of the ceramic line width (~17%) was close to that of line height (~19%). The slight difference may be caused by the shrinkage of the PZT disc (as a substrate) during sintering, which affects the shrinkage of line width more than line height. The similar trends were also

observed for the composites fabricated by thermoplastic green machining and FDC[117,119]. Such shrinkage needs to be incorporated into the AutoCAD design in order to obtain required composite dimensions.

The optical image of the final composite A after polymer infiltration, polishing and electroding is shown in Fig. 6.15.

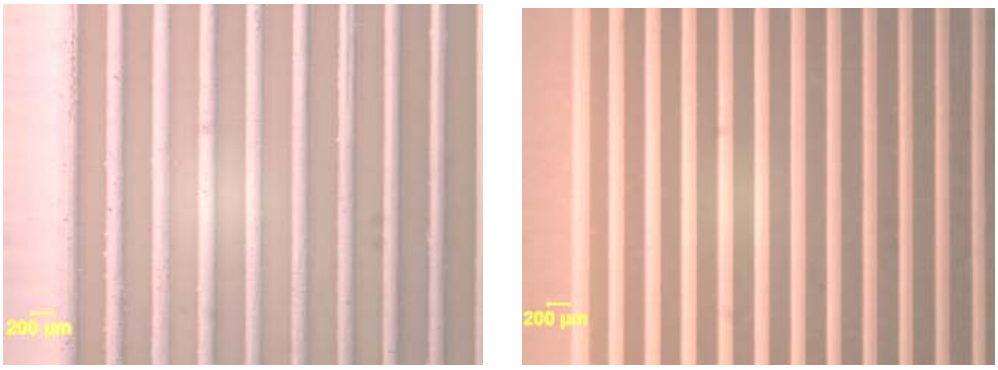

(a) after BBO (b) after sintering

Fig. 6.14 Optical images of a representative PZT structure of composite A.

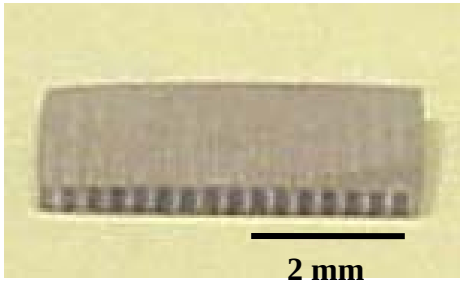

Fig. 6.15 Optical image of the composite A after polymer infiltration, polishing and electroding.

6.3.6 Dielectric, piezoelectric and electromechanical properties

After adjusting the Micropen^{TM} writing parameters, ~120 μm in maximum ceramic line width and ~50 μm in one-layer thickness were achieved for the sintered PZT structures using a 100-μm pen tip. For the composites A and B, the thicknesses were about 360 and 380 μm, respectively, indicating 7-8 layers after polishing. The width of polymer phase of composite A was about 250 μm, and that of composite B was 170 μm. Therefore, the thickness-to-width aspect ratios of the ceramic phase were about 3.0 and 3.2, for A and B, respectively. As discussed in section 6.1.3, these ratios should be sufficient to obtain a clean thickness mode with weak coupling between thickness and other vibrational modes.

Table 6.6 summarizes the dielectric, piezoelectric and electromechanical properties of the two representative composites A and B, along with a pressed PZT disc for comparison which was prepared under the same condition as the Micropen^{TM} deposited samples. The planar mode coupling factors (k_p) of the composites could not be measured due to the rectangular geometry.

The ceramic fractions were ~30 vol% for composite A and ~45 vol% for composite B. As discussed in section 6.1.3, the ceramic volume fraction plays an important role in determining optimum efficiency both in transmitter and receiver modes for ultrasound transducers. The values of 30 and 45 vol% for the two composites fall in the general range of 20-60 vol% to achieve good sending output and receiving sensitivity.

Table 6.6 also shows that the dielectric constants (K) of the composites were proportional to the ceramic volume fractions, as expected, because K does not depend on coupling between ceramic and polymer phases[131]. In addition, the dielectric losses for the

composite A and B were 2.1% and 2.4%, respectively. Such small values of loss are comparable to those found in literature.

As mentioned in section 6.1.2, k_t is one of the important properties of the composites for medical imaging applications. Fig. 6.17 and Fig. 6.17 illustrate the impedance and admittance spectra of the fundamental thickness mode resonance for the composite A and B, respectively. It is shown that the composite A had a clean thickness mode resonance with a resonance frequency of 4.1 MHz, and the thickness mode coupling factor (k_t) of ~0.60 was calculated. For the composite B, using the same method, a k_t of ~0.62 was calculated. However, small humps were observed in the impedance and admittance spectra, which could be due to the misalignment between deposited ceramic layers. The values of k_t for the two composites are comparable to what reported in literature using other techniques. Compared to the bulk sample, the enhancement of k_t for the composites should be mainly caused by the partial relief of the lateral clamping in the polymer environment[132]. Furthermore, it was found that the Q_m values for the composite A and B were 7 and 6, respectively. The lower Q_m values obtained should be due to the partial damping of the ceramic plate's vibration by the surrounding polymer, indicating that such composites are suited for the broad bandwidth applications[133].

The d_{33} values were found to be 210 and 320 pC/N for the two volume fractions, and the calculated d_{33} values were approximately 265 and 330 pC/N, which were close to the measured ones. It indicated an increase with increasing ceramic volume fraction in our study. Other trends such as no obvious dependence of the ceramic volume fraction on d_{33} have also been observed[116, 121]. Because the d_{33} of composites is influenced by a combination of many factors such as the thickness of composites, the aspect ratio of the

ceramic phase and the bonding between the ceramic and polymer phases, which all affect the stress transfer between the two phases[134]. In addition, the choice of polymer and the control of lead loss during sintering will also affect d_{33} values.

Table 6.6 Comparison of the dielectric, piezoelectric and electromechanical properties of a pressed PZT disc and the two composites fabricated by Micropen™.

Sample	V_{PZT} (vol%)	Thickness (mm)	K	tanδ (%)	d_{33} (pC/N)	k_t	k_{31}	Q_m	Density (g/cm^3)
Bulk	100	0.91	2880	1.8	630	0.56	-0.43	20	7.77
Composite A	30	0.36	650	2.1	210	0.60	-0.36	7	3.18
Composite B	45	0.38	940	2.4	320	0.62	-0.34	6	4.20

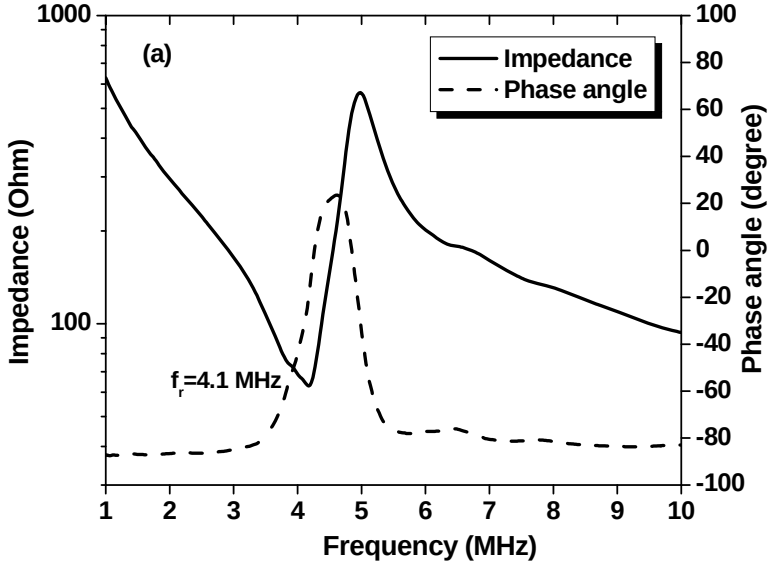

(a)

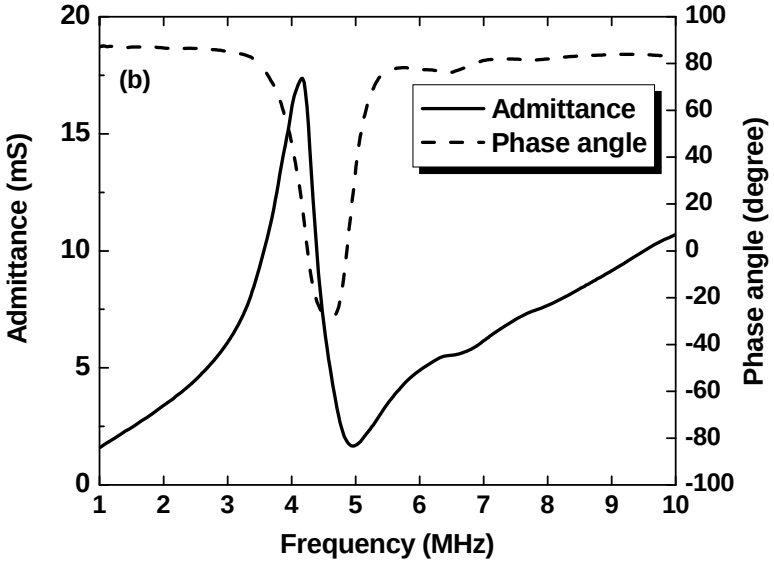

(b)

Fig. 6.16 (a) Impedance and phase angle spectra and (b) admittance and phase angle spectra of the composite A.

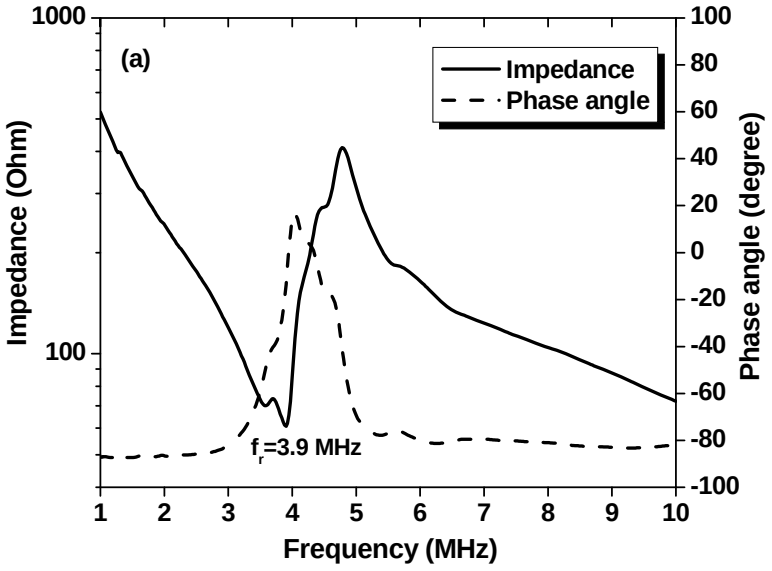

(a)

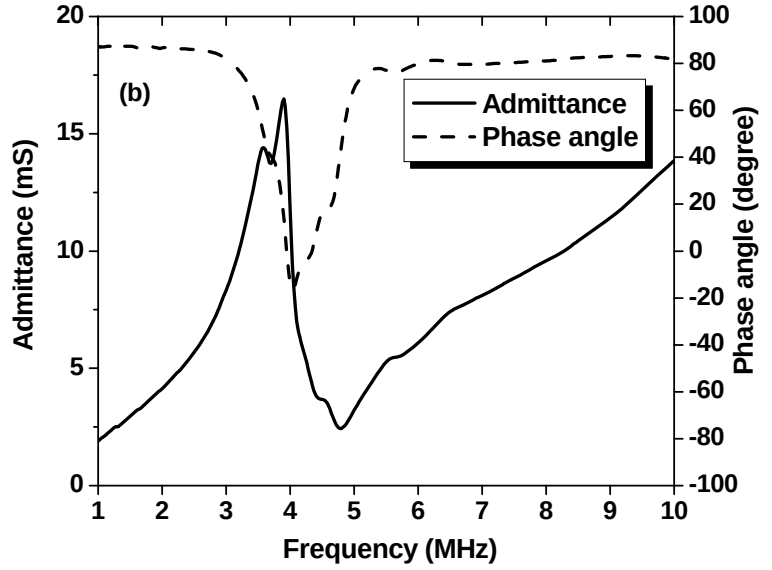

(b)

Fig. 6.17 (a) Impedance and phase angle spectra and (b) admittance and phase angle spectra of the composite B.

6.4 Summary

PZT ceramic/polymer composites with 2-2 connectivity have been fabricated using Micropen^{TM} direct-write technique for the first time. A 35 vol% PZT paste was prepared for the Micropen^{TM} deposition, which exhibited shear thinning behavior with a viscosity of ~ 45 Pa·s at low shear rate (0.1 s^{-1}).

Among writing parameters, it was found that the "cross section" was crucial for the dimensional control in deposition by Micropen^{TM}. After sintering, the ceramic skeletal structures were fully densified, with good bonding among layers after sintering.

The composites (thickness=300-400 μm) had resonance frequencies at ~4 MHz, and good dielectric and electromechanical properties (K=650-940, tanδ=2.1-2.4%, k_t=0.60-0.62, Q_m=6-7 and d_{33}=210-320). Such results indicate that Micropen^{TM} direct-write has the potential to fabricate miniaturized 2-2 composites and composites with novel designs for medical imaging transducers.

CHAPTER7 DESIGN AND DEVELOPMENT OF VOLUME FRACTION GRADIENT COMPOSITES BY DIRECT-WRITE TECHNIQUE

7.1 Introduction and objectives

This chapter describes the fabrication of ceramic/polymer composites with volume fraction gradient (VFG) design using Micropen^{TM} direct-write. This chapter is organized into three sections. The first section is an introduction to the basic types of medical ultrasound transducers and the previous study on VFG composites. The second section is the experimental procedures used in this work. The third section is the discussion focusing on the Micropen^{TM} deposition and the characterization of the VFG composites' properties.

7.1.1 Basic types of medical ultrasound transducers

The basic types of medical ultrasound transducer devices are single-element transducers and array transducers which include annular arrays, linear arrays, and phased arrays. Each type of devices has different features and applications.

The simplest type of transducers is single-element transducers. Fig. 7.1 (a) is a typical single-element transducer, mainly consisting of a piezoelectric element, matching layer(s) and backing layer. The matching and backing layers are normally polymer-based materials. The matching layer is used to obtain impedance matching with human organs for higher energy transfer efficiency, and the backing layer is used to decrease ringing for better lateral resolution. The available active materials can be piezoelectric ceramics, ceramic/polymer composites, piezoelectric polymers and single crystals[135]. The main advantage of single-element transducers is the design and simplicity of fabrication. Thus,

the most successful commercial transducers for high-frequency (>20 MHz) applications are single-element transducers. However, this type of transducers can only produce beams with a fixed focus, meaning the spatial resolution is best only within the depth of focus. Another disadvantage is that the transducers have to be mechanically moved to form an image.

The above problems can be overcome by using arrays transducers. In general, array transducers have the similar basic structure as single-element transducers, except that each array element is designed to act as a single isolated transducer. The level of interactivity (or cross talk) between array elements is of particular concern, and the mechanical and electrical coupling between elements should be avoided. Fig. 7.1 (b) is a representation of a typical linear array structure. The piezoelectric material is slotted to separate individual array elements, in order to be electrically and acoustically decoupled from each other. All elements are connected with a common ground plane electrode, but are separated with individual positive electrodes (called “electronic channels”). And an individual array element may be slotted again to form sub-elements. The matching layer is also often slotted to improve acoustic isolation between elements. A phased array has a similar construction as a linear array, but smaller and requires fewer elements. For example, linear arrays usually contain 128 to 512 elements, and phased arrays contain 64 to 256 elements. For both linear and phased arrays, the focal point can be varied through the depth of field (called “dynamic focusing”). The major difference between them is the way that beamforming is implemented. In a linear array, a small group of neighboring elements is excited sequentially by multiplexing to move the beam from one end of the transducer to the other end. In this way, the sound beam is moved electronically (called

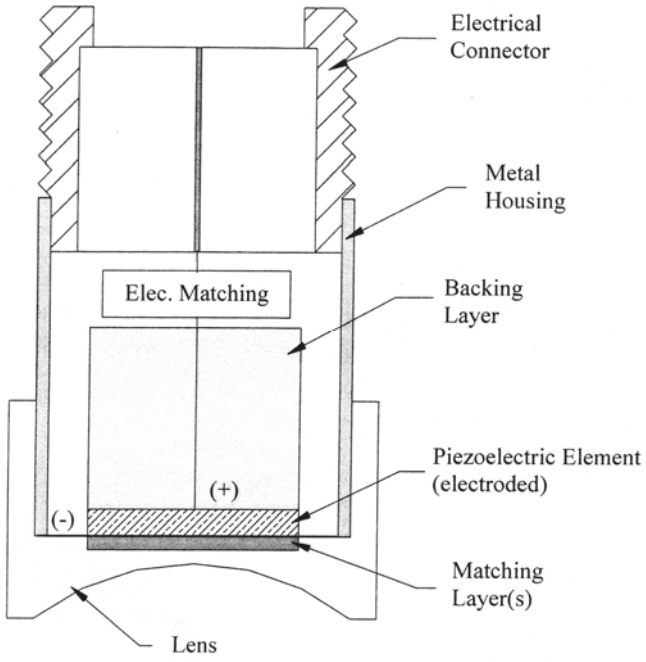

(a)

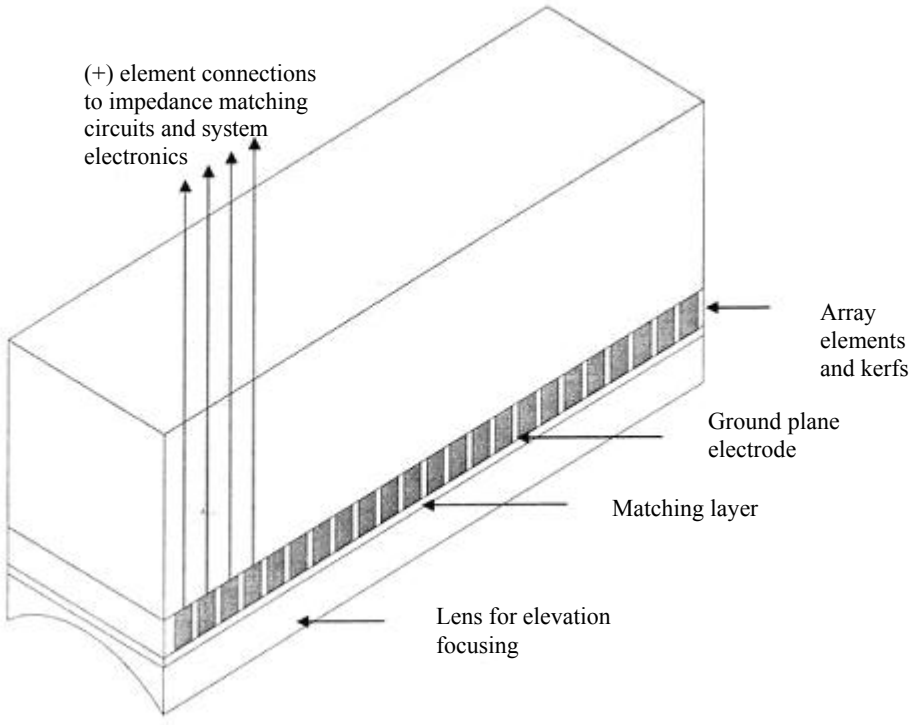

(b)

Fig. 7.1 Cross sections of (a) a single-element transducer and (b) a linear array transducer[136].

"electronic scanning"), producing a picture similar to that obtained by scanning a single-element transducer manually. While a phased array can sweep a sound beam through a range of angles ("steering") excited by all the elements based on electronic delays. Therefore, linear arrays are suitable when the imaging window is large, providing easy access to the explored media. Phase arrays with steering capability are ideal for imaging large organs like a human heart through small anatomic window such as the gap between rib bones[137].

Another type of array transducers is annular arrays, which provide a viable alternative to single-element and linear array transducers[138]. Annular arrays are made of concentric piezoelectric rings which surround a central aperture. These arrays provide an axisymmetric beam pattern like single-element, while providing the "dynamic focusing" at multiple depths by electronic delays. Their drawback is that a mechanical device is still required to scan the ultrasonic beam, as the single-element transducers. However, for high-frequency applications (>20 MHz), the design of annular arrays provide significant benefits compared to linear arrays, due to less complex beamforming, simpler fabrication, and a fewer number of elements. Therefore, annular arrays bridge the gap in performance and complexity between single-element and linear (or phased) arrays. The features of the above four types of transducers are listed in Table 7.1.

Table 7. 1 The features of four types of transducers.

	Focusing	**Scanning methods to form an image**
Single-element	fixed (-)	mechanical scanning (-)
Annular arrays	varied (+)	mechanical scanning (-)
Linear arrays	varied (+)	electronic scanning (+)
Phased arrays	varied (+)	steering (+)

A (+) sign and a (-) sign mean the feature is an advantage and a disadvantage, respectively.

Recently, there has been an increase in interest for high-frequency (>20 MHz) annular arrays. In general, the two considerations for annular arrays design are: (1) Design equal-area elements to obtain approximately the same electrical impedance for beamforming, and more importantly, to obtain an equal phase shift across each element. (2) The outer array elements normally are three times wider than the thickness of transducer substrate, in order to eliminate lateral mode vibrations[139]. For the high-frequency annular arrays, the conventional fabrication is laser micromachining, since a mechanical dicing saw can not create concentric annuli[140]. For example, K.A. Snook *et al.* developed a six-element, 41 MHz annular array using laser micromachining[141]. The active material was a submicron lead titanate (PT) ceramic, which exhibits much lower planar coupling (k_p=0.07) than traditional PZT ceramics (k_p>0.45). Fig. 7.2 (a) shows the annular design and solder connections between wires and the PT elements. The 6-mm diameter PT disc was used, and the individual elements were created by a commercial laser micromaching system. The width of the outermost element was 113 μm, and the narrow gaps between the elements were cut by the laser. The details can be seen from the SEM image in Fig. 7.2 (b), showing the thickness of the ceramic disc was lapped to ~60 μm, and the kerf widths (spacing between the ceramic elements) were ~25 μm.

In addition to the conventional design above, another design for high frequency (>50 MHz) annular array transducers is a kerfless design[142, 143]. The kerfless design is based upon using a thin layer of ceramics (~40 μm thick) or polymers (~9 μm thick), and the individual active elements were defined by the electrode patterns using photolithography or flexible circuit traces, instead of laser cutting. The advantage of this design is simplicity of fabrication, but the device performance may be sacrificed. Because

the array elements are not separated by grooves, it is expected that the array may suffer from large electrical and mechanical coupling between the elements, or the flexible circuit may bring spurious resonances. Table 7.2 summarized the array design and transducer performance for the above three annular array transducers.

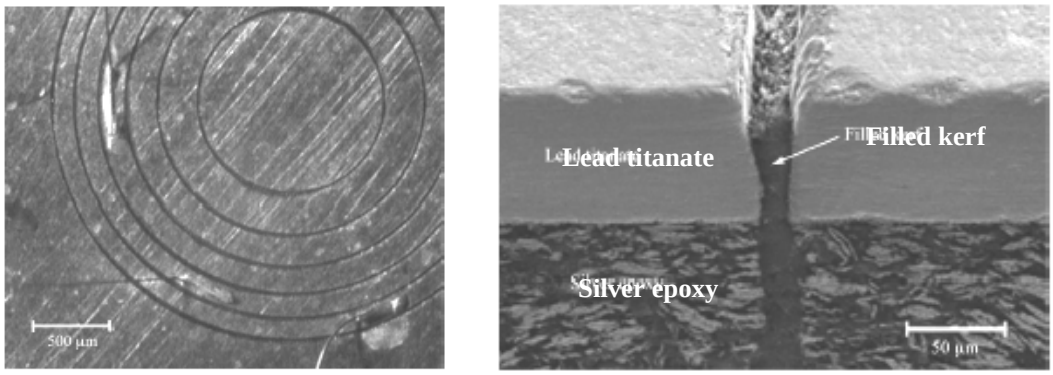

(a) (b)

Fig. 7.2 (a) Image of a six-element annular array created by laser micromaching and (b) SEM image of the kerf after laser micromaching and filling with epoxy.

Table 7. 2 The summary of the array design and transducer performance for the three annular array transducers.

	Array design factors	**Transducer performance**
Laser micromaching (K.A. Snook)	Active material: PT 6-element Thickness: ~60 μm Center aperture diameter: 1.1 mm Kerf width: ~25 μm	Center frequency: ~43 MHz Bandwidth: 30% Average insertion loss: 31 dB Maximum cross talk: -27 dB (in water)
Kerfless design (J.A. Ketterling)	Active material: PZT 7-element Thickness: ~40 μm Center aperture diameter: 0.7 mm Separation between electrodes: ~10 μm	Center frequency: 55 MHz Bandwidth: 50% Average insertion loss: 16 dB Cross talk: very high (due to not-separated array elements)
Kerfless design (E.J. Gottlieb)	Active material: copolymers (P(VDF-TrFE) 8-element Thickness: ~9 μm Center aperture diameter: ~1.0 mm Kerf width: ~ 30 μm	Center frequency: 55 MHz Bandwidth: 47% Average insertion loss: 33.5 dB Cross talk: <-29 dB

7.1.2 Volume fraction gradient (VFG) composites

In ultrasonic medial imaging, it is desirable to have the maximum beam sensitivity along the transmission axis. However, the presence of side lobes and grating lobes produces off-axis sensitivity and thus greatly affects the image quality. As shown in Fig. 7.3 of a linear array transducer, the side and grating lobes refer to the energies in an acoustic beam pattern that fall aside the main lobe. With high intensity side and grating lobes, the receiver is sensitive to echoes coming from these angles in addition to the main axial direction. Thus, phantom objects will be generated, reducing the imaging clarity[144].

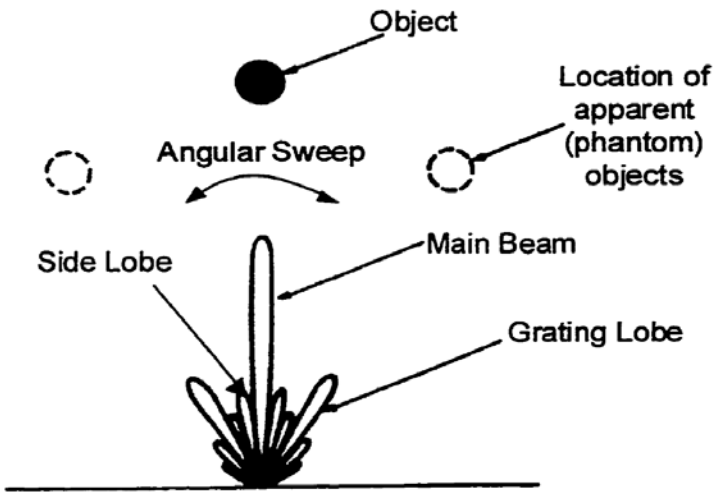

Fig. 7.3 A typical beam pattern obtained for an ultrasonic transducer showing the side and grating lobes[90].

The grating lobes are caused by the constructive interference when the rays from adjacent array elements are in phase with each other. To eliminate grating lobes, it is found that the pitch should be shorter than one wavelength[136]. Other methods such as varying the width of ceramic poles or kerf width in a 1-3 composite can also reduce grating lobes[145].

The finite width of piezoelectric array elements causes the edges of those elements to move freely. This motion generates lateral waves propagating through the piezoelectric elements and the matching layer, which in turn may excite an undesirable secondary wave. Such a wave creates side lobes in the acoustic beam profile. The direction of the side lobes in an external medium (human body) is given by the expression[146]:

$$\sin\theta = \frac{v_0}{v_1} \tag{7.1}$$

where v_0 is the velocity of the wave in the acoustic medium (~1500 m/s), and v_1 is the velocity of the lateral wave in the piezoelectric elements (~3000 m/s). Consequently, a side lobe is around 30° to the main beam.

The intensity of the side lobes depends on the amplitude of the element edge vibration. For a transducer using piezoelectric composite, one of the approaches to suppress the side lobes is to introduce a ceramic volume fraction gradient (VFG) along the width of the composite. Because the pressure output for a composite transducer is proportional to the ceramic volume fraction. Therefore, a decrease in the ceramic content from the center towards the edges produces a decrease in the sensitivity along the same direction[147].

It is challenging to fabricate novel ceramic/polymer composites including volume fraction gradient (VFG) design using the traditional dice-and-fill technique. Because the kerf width increases from the center to the edges while a saw blade with a single thickness is used in a dicing machine. Previous work on the VFG 2-2 composites in rectangular geometry has been reported by R.K. Panda at Rutgers[148]. In his work, the VFG composites were fabricated by one of the solid freeform fabrication (SFF)

techniques, Sanders prototyping (SP), by an indirect lost mold route. Briefly, wax sacrificial molds having a negative of the desired structures (shown in Fig. 7.4 a) were first designed and built using the SP technique; then a aqueous PZT ceramic slurry infiltrated the molds. After infiltration, the green parts were debindered and sintered, followed by embedding in an epoxy to make composites. The modeling studies shown in Fig. 7.4 (b) predicted that on the acoustic beam pattern the side lobe level would decrease for the VFG composites, and the composite with linear distribution had better result than that with Gaussian distribution.

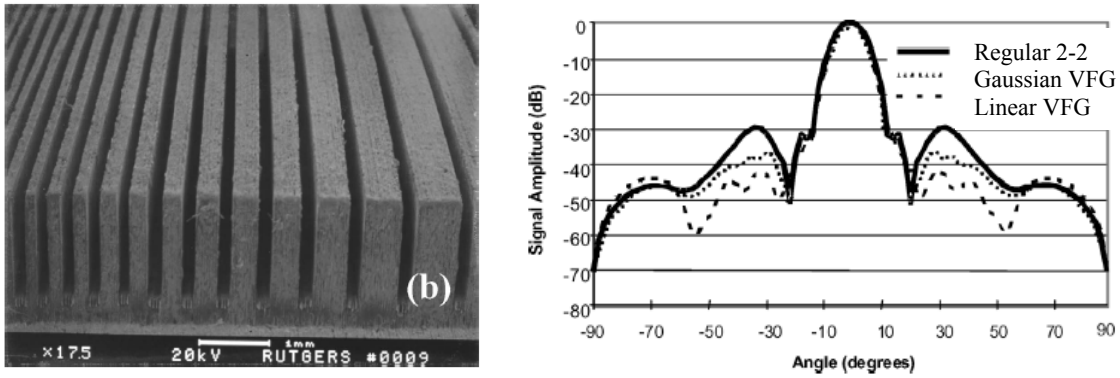

(a) (b)

Fig. 7.4 (a) SEM photograph of the Sanders-built wax sacrificial mold for a linear distribution and (b) Modeling studies of the beam pattern for two VFG composites[148].

7.1.3 Objectives

The Micropen™ technique, as a direct route, provides greater design flexibility and requires fewer processing steps, compared to the dice-and-fill technique. Therefore, the objectives of this chapter are:

(1) To demonstrate the feasibility of fabricating volume fraction gradient (VFG) composites using the Micropen™ technique. Composites with Gaussian and linear volume fraction gradients in rectangular and annular geometries will be designed and fabricated.

(2) To fully characterize the dielectric and piezoelectric properties of the VFG composites including vibration amplitude measurements, and to study the effects of different volume gradients and geometries on the electromechanical properties of the composites.

The purposes of designing rectangular and annular geometries are the following: (1) These configurations can be utilized for ultrasound transducers with different geometric requirements, such as single-element, linear or annular array transducers; (2) Annular composites, in particular, are designed to obtain reduced planar coupling factor (k_p) and weaker coupling between thickness and lateral vibrational modes to maximize transduction efficiency, compared to a PZT ceramic disc.

7.2 Experimental Procedures

7.2.1 The VFG composites design

In this study, two types of volume fraction gradient (VFG) composites, Gaussian and linear distributions were designed. Those VFG composites were constructed on the basis of the following mathematical functions: $f(x) = kx + b$ (for the linear composites), and $f(x) = ae^{-b(x-1)^2}$ (for the Gaussian composites). Here, $f(x)$ is the local ceramic volume fraction, and x is the sequence of PZT lines from center to edge in a composite. For example, for a rectangular VFG, to deposit 11 lines on each side from the center, the variable x will be 1, 2, 3 … to 11.

Fig. 7.5 shows the designed ceramic volume fractions from center to edge for the two VFG composites. The figure represents that the mathematical functions were based on the assumptions that 60 vol% ceramic contents were designed at the center and 20 vol% were designed at the edges of the composites, respectively. Such designs were made by taking the effects of ceramic volume fraction on the transmitting/receiving sensitivity and k_t into consideration (discussed in section 6.1.3). For example, a high ceramic fraction (60 vol%) was chosen at the center to achieve a high transmitting output and a high k_t. A further increase in the ceramic content would decrease the receiving sensitivity of a transducer. It would also increase the acoustic impedance difference between the center and edge regions, thus a more complex matching layer would be needed for good energy transfer across the whole composite. Fig. 7.5 also shows that from center to edge, the ceramic contents gradually decreased at different rates following Gaussian or linear distributions.

For the VFG composites, the local ceramic volume fractions and the distances between two adjacent ceramic elements were calculated from the mathematical functions above using Matlab software. Then, the ceramic skeletal structures for the Micropen™ deposition were designed using AutoCAD software based on the calculated results.

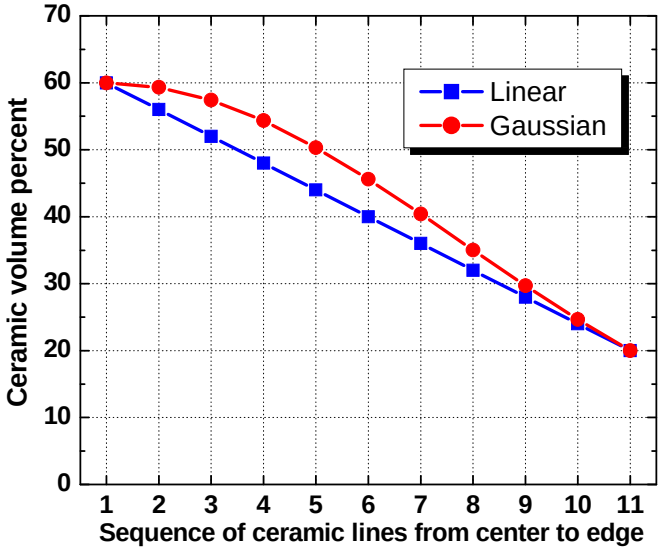

Fig. 7.5 The designed variations of ceramic volume fraction from center to edge for the two VFG composites.

7.2.2 Paste preparation and the deposition of ceramic skeletal structures

A 45 vol% PZT paste was used for the Micropen^{TM} deposition, instead of the 35 vol% paste, in order to obtain higher aspect ratios (t/w) and faster drying after the deposition. The 45 vol% paste contained 37.8 g stearic acid-coated PZT powder, 5.30 g α-terpineol and 0.34 g ethyl cellulose (as binder). The details of paste preparation were described in Chapter 6. To avoid pen tip clogging due to a higher ceramic solids loading compared to the 35 vol% paste, an additional processing step was added. The coated PZT powder was ground by a mortar and pestle, and then sieved through a No. 100 sieve (opening size 150 μm) to break agglomerates before mixing with the terpineol solution.

In this study, a 175-μm pen tip was used for the deposition. Because a 100-μm pen tip was easily clogged and also was difficult to clean when using the 45 vol% paste. This is probably due to a higher solids loading which is easier to clog the small pen tip.

The deposition procedures were similar to those adopted in Chapter 6. The optimized writing parameters for the 45 vol% PZT paste and the 175-μm pen tip are listed in Table 7.3.

Rectangular and annular composites without volume fraction gradients were also deposited for the comparison with the VFG composites. Two types of geometries, rectangular and annular geometries, were designed for the composites. For the skeletal structures in rectangular geometry, the numbers of deposited layers for the Gaussian, linear and the sample without VFG were 11, 11 and 12, respectively. For the structures in annular geometry, the numbers of layers for the Gaussian, linear and the sample without VFG were 11, 11 and 10, respectively.

The procedures of composite fabrication were similar to that in Chapter 6. Briefly, after deposition, the green PZT skeletal structures were debinded at 550 ºC, followed by sintering at 1250 ºC for 1 h. The ceramic structures were then infiltrated with epoxy to form composites. After polishing and electroding, the composites were poled at 30 kV/cm for 15 min at 50 ºC.

7.2.3 Vibration amplitude profile

Most of the characterization methods for the composites were also similar to that in Chapter 6, except that vibration amplitude measurement was applied in this study. The purpose of the measurement was to observe the variations of pressure output as a function of the ceramic volume fraction gradient of the composites. The following is the details of the measurement:

The electric-field induced displacements of a composite sample were measured by a fiber-optic fotonic sensor (MTI-2000, Mechanical Technology Inc., Albany, NY). The vibration amplitude profile of a composite was calculated from the displacement results using the equation of $20\log_{10}(\frac{a_1}{a_0})$, where a_1 is the displacement at different positions of a sample, and a_0 is the displacement at the sample's center which is used as a reference.

This technique is one of the promising non-contact techniques to measure small displacements induced by electric field. The MTI-2000 fotonic sensor offers non-contact measurements of displacement and vibration of a reflecting surface, with a resolution of 5-10Å[149]. The fiber-optic probe consists of adjacent pairs of light-transmitting and light-receiving fibers located in the close proximity to a moving surface. As illustrated in Fig. 7.6, the principle of operation is based on the interaction between the field of illumination

Table 7.3 The Micropen™ parameters for the direct-write of PZT skeletal structures (using a 175-μm pen tip and the 45 vol% paste).

Cross section (mil^2)	Writing speed (mil/s)	Writing force (mg)	Trigger height (mil)	Lift force (mg)	Lift speed (mil^3/s)	Term volume (mil^3)	Term speed (mil^3/s)	Burst volume (mil^3)	Burst speed (mil^3/s)
30	25	10	0.6	80	25000	100000	150000	0	500

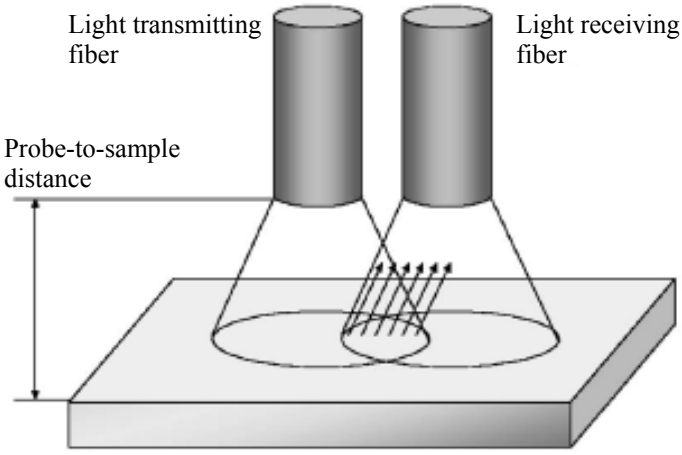

Fig. 7.6 Schematic drawing of the displacement sensing mechanism in the MTI-2000 fotonic sensor[149].

of the transmitting fibers and the field of view of the receiving fibers[150]. The output signal captured by the receiving fibers changes as a function of the probe-to-sample distance. In detail, at zero distance, the output signal is nearly zero because most of the light from the transmitting fibers is reflected directly back into the same fibers, providing little light to the receiving fibers. When increasing the probe-to-sample distance, reflected light captured by the receiving fibers will increase until the entire face of the receiving fibers is illuminated. Further increase in the distance will decrease the output, because the diverging field of reflected light will exceed the field of view of the receiving fibers.

In order to measure displacements as a function of position for a gradient composite, the fotonic probe was mounted on a manual micropositioner, providing motion in both horizontal (x, y) and vertical (z) directions. The outer diameter of the probe used was about 3.1 mm, and the probe was moved in steps of 1 mm based on sample's dimension. Therefore an average displacement response of a composite was investigated. In addition, an electric field of 20 kV/cm was applied by a Radian Precision LC system (Radiant Technologies Inc, NM) and the displacements were measured in monopolar mode by using the software Vision.

7.3 Results and Discussion

7.3.1 Thermal study of the PZT Paste

As shown in Fig. 7.7, the TGA result showed ~ 88 wt% residue at 600ºC for the 45 vol% paste designed, which was in agreement with the calculated value (~86 wt%). Similar to the TGA result of the 35 vol% paste, a major weight loss of ~10.5 wt% below 175 ºC was be due to the solvent removal, and a minor weight loss of 1.5 wt% between 175-400 ºC was attributed to the binder and dispersant decomposition.

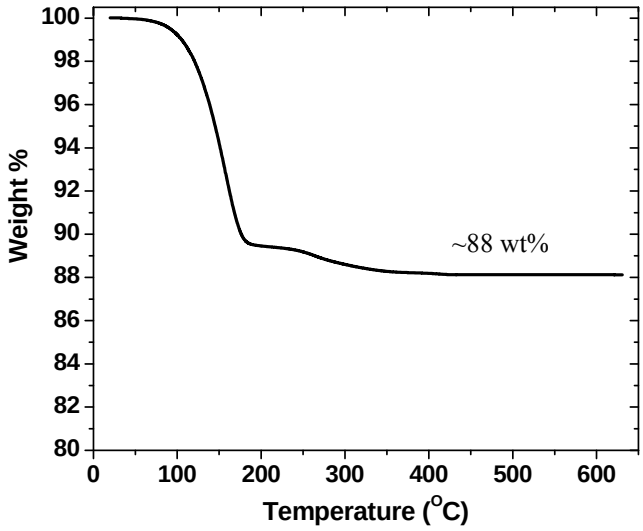

Fig. 7.7 TGA curve of the 45 vol% PZT paste.

7.3.2 Effects of "cross section" on PZT line dimension

As we have discussed in the previous chapters, the writing parameter, "cross section" (CS) plays an important role in controlling the line dimension deposited by the Micropen^{TM} direct-write. Similarly to the study carried out in section 6.3.2, it is helpful to plot the variations of line width (LW), line height (LH) and actual cross section (ACS) as a function of "input CS" (CS=5, 10, 15, 20, 25 and 30 mil^2, i.e. CS=3226, 6452, 9677,

12903, 16129 and 19355 μm^2), shown in Fig. 7.8 (a) and (b). The test samples were one-layer deposition on glass slides, using a 175-μm pen tip and the 45 vol% paste (writing speed=50 mil/s, writing force=20 mg). Linear fitting ($y = A + Bx$) was also done for the three relationships (shown in Fig. 7.8), and the values of A, B and R (correlation coefficient) are listed in Table 7.4.

It is clear that in the range of "input cross section (CS)" studied, LW, LH and ACS increased almost linearly with increasing CS, showing the same trend as that in section 6.3.2. In addition, compared to the results using a 100-μm pen tip and the 35 vol% paste, it was possible to obtain a smaller line width and a bigger line height at a same "CS" value. For example, for an "input cross section"=12900 μm^2 (i.e. 20 mil^2), the line heights for the 35 and 45 vol% pastes were 38 and 61 μm, respectively; and the line widths for the 35 and 45 vol% pastes were 316 and 270 μm, respectively. The smaller line width obtained using the 45 vol% paste is most likely due to its higher viscosity. At a shear rate of 0.1 s^{-1}, the viscosity was ~3280 Pa·s for the 45 vol% paste, and that for the 35 vol% paste was ~45 Pa·s (shown in Fig. 6.9). Therefore, a paste with higher solids loading is desirable to obtain a higher aspect ratio (t/w).

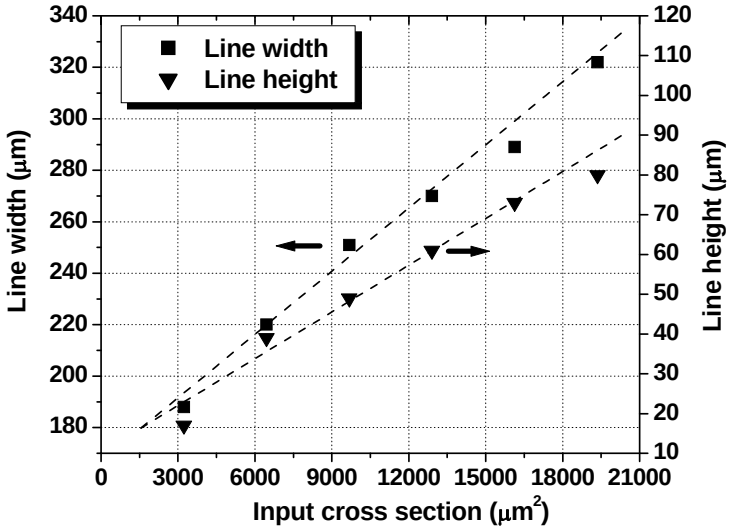

(a)

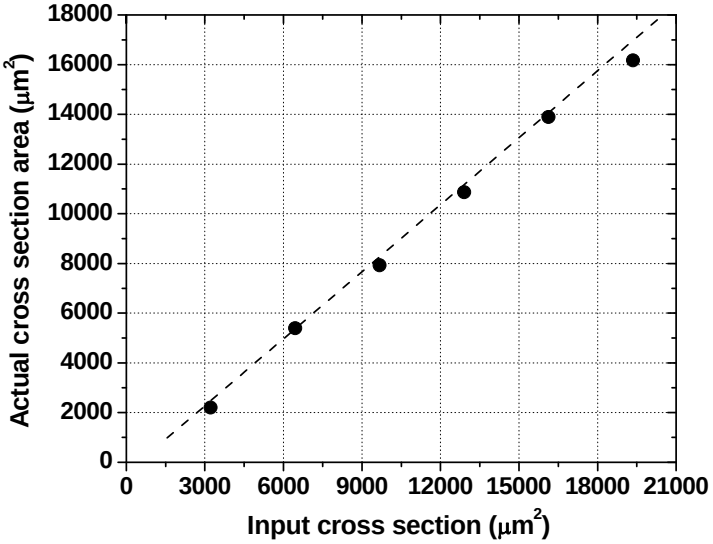

(b)

Fig. 7.8 The variations of (a) line width, line height and (b) actual cross section as a function of "input cross section" using a 175-μm pen tip and the 45 vol% paste.

Table 7.4 The values for A, B and R in the linear fitting for the three relationships (using a 175-μm pen tip and the 45 vol% paste).

Relationship	A (μm^{-1})	B (μm)	R
Input CS-LH	10.27	0.0039	0.9866
Input CS-LW	167. 07	0.0082	0.9950
Input CS-ACS	-419.70	0.90	0.9992

7.3.3 Deposition of the ceramic skeletal structures

For the various writing parameters of the Micropen^{TM} deposition, "cross section" and "writing speed" were two important parameters which should be set first. As shown in Table 7.3, compared to the parameters listed in Table 6.4 for a 100-μm pen tip and the 35 vol% paste, the "writing speed" was kept constant at 25 mil/s, and a higher "cross section" of 30 mil^2 was chosen. By choosing these parameters, it was possible to obtain similar one-layer thickness when using a bigger pen tip.

Fig. 7.9 (a)-(f) show the optical images of as-deposited multilayer PZT skeletal structures for the composites with and without VFG in both rectangular and annular geometries. The deposited layers were 12, 10, 13, 11, 11 and 10 for the structures from (a) to (f), respectively. As it is shown, a serpentine pattern was used in rectangular geometry, and a connection between the individual rings was incorporated in annular geometry. Such design was made to ease the deposition process due to the continuous nature of the Micropen^{TM} writing. In addition, in annular geometry, a solid ceramic center with a diameter of ~1.4 mm was designed, in order to obtain a maximum pressure output at the center of composites. Furthermore, in rectangular geometry, "additional lines" were added at the left and upper regions of the structure (marked by circles in Fig. 7.9 a). Consequently, the starting point was moved from point A to B. Such small modifications were helpful to deposit multilayer structures successfully. As discussed in section 6.3.4, because it is challenging to exactly control the material flow at line starts and ends in the "transient" state, the first line is easy to be destroyed during deposition and it will affect the deposition of a whole structure. In contrast, writing the "additional lines" provided more time for the material flow to reach the "stationary" state. Also, the new starting

point B, located at the intersection of two lines, gave stronger support for the pen tip at the beginning of a deposition, especially when more layers were deposited.

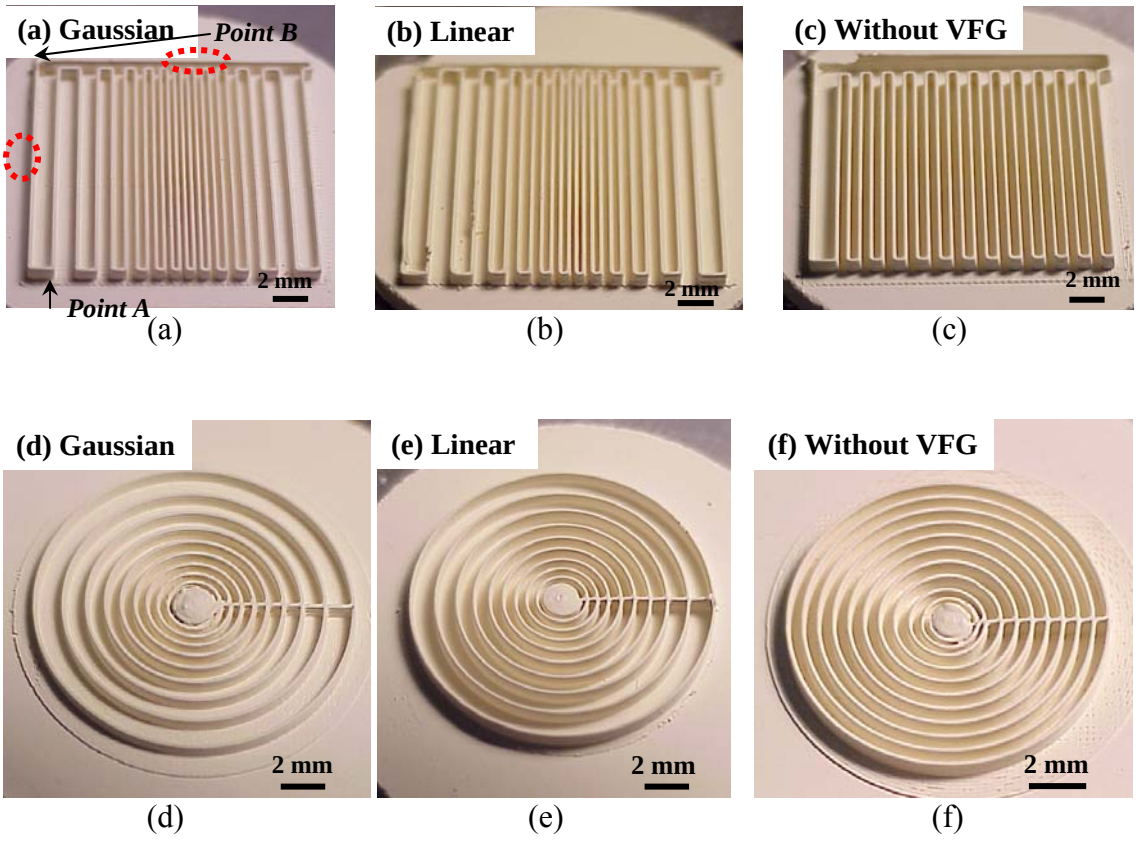

Fig. 7.9 (a)-(f) Optical images of as-deposited multilayer ceramic skeletal structures on PZT discs in rectangular and annular geometries.

7.3.4 Dielectric, piezoelectric and eletromechanical properties

After deposition and sintering, the average values for the maximum line width and one-layer thickness for a sintered ceramic element were about 170 μm and 60 μm, respectively. Fig. 7.10 (a)-(f) show the optical images of polished composites with and without VFG in rectangular and annular geometries. Their dielectric, piezoelectric and electromechanical properties are summarized in Table 7.5, along with a PZT disc for comparison. It was found that the dielectric constants were approximately proportional to the ceramic volume fractions in the composites. The dielectric losses (tanδ) were relatively low, in the range of 2.1-2.3%. The composites showed two main advantages over the ceramic bulk sample: higher thickness mode coupling factors (k_t: 0.66-0.72) and lower mechanical quality factors (Q_m: 5-9). The similar trends have been observed for the two composites using the 35 vol% paste in Chapter 6. The piezoelectric charge coefficient d_{33} varied from 260 to 320 pC/N, which were the average values of the entire composites.

For the Gaussian and linear composites designed in rectangular geometry, the impedance and phase angle spectra of the thickness mode were illustrated in Fig. 7.11 (a) and (b), respectively. It was found that the resonance frequency of the Gaussian composite was 3.1 MHz, and that of the linear composite was 3.4 MHz. It is noted that both of the gradient samples had clean thickness mode resonances. Such results indicate that (1) the thicknesses of the two composites were relatively uniform; (2) the aspect ratios of ceramic element for the two samples ($t/w \approx 2.5$) did not generate obvious lateral or other spurious modes to interfere with the thickness mode in the frequency range investigated (1-10 MHz).

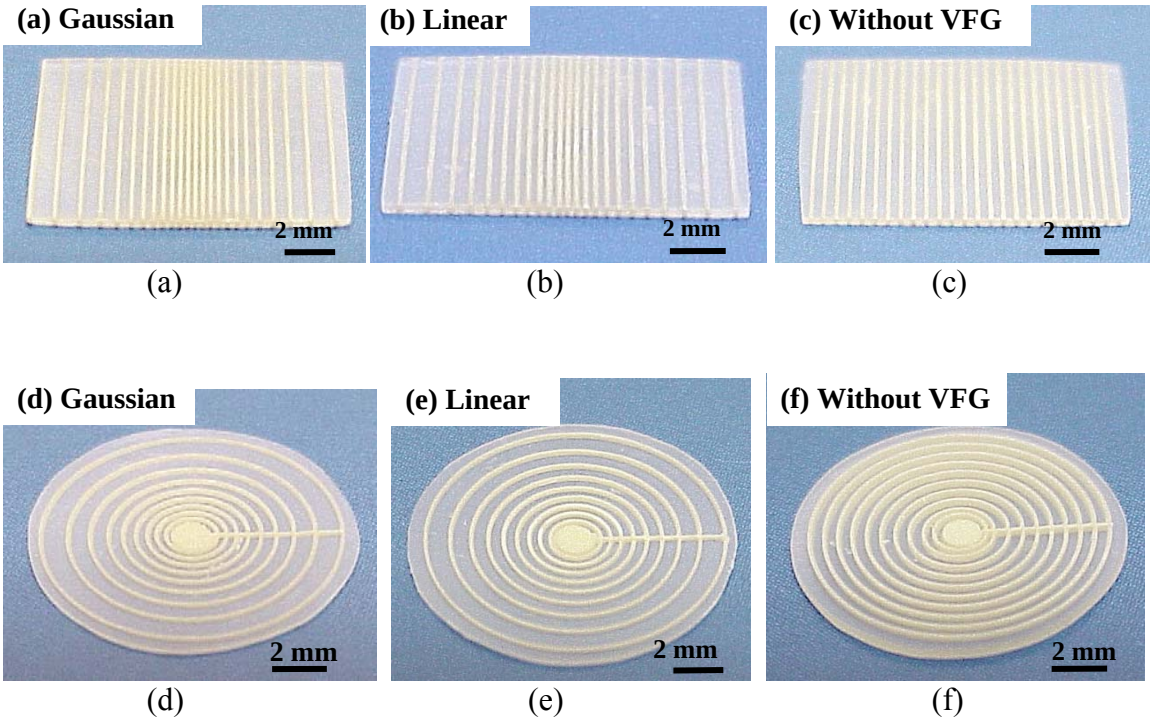

Fig. 7.10 (a)-(f) Optical images of polished composites with and without VFG in rectangular and annular geometries.

Table 7.5 Comparison of the dielectric, piezoelectric and electromechanical properties of a PZT disc and the composites with and without VFG fabricated by the Micropen™.

	Sample	V_{PZT} (vol%)	t (mm)	K	tanδ (%)	k_t	k_p or k_{31}	Q_m	d_{33} (pC/N)	Density (g/cm^3)
	Bulk	100	0.93	2880	1.8	0.56	k_p=0.74, k_{31}=-0.43	20	630	7.77
Rectangular	**(a) Gaussian**	28	0.45	630	2.3	0.72	k_{31}=-0.39	9	260	3.01
	(b) Linear	25	0.42	650	2.3	0.70	k_{31}=-0.39	6	290	2.80
	(c)Without VFG	28	0.32	640	2.1	0.68	k_{31}=-0.34	9	290	2.99
Annular	**(d) Gaussian**	23	0.22	565	2.1	0.70	k_p=0.36	7	280	2.62
	(e) Linear	22	0.27	540	2.1	0.72	k_p=0.37	5	265	2.55
	(f)Without VFG	26	0.42	640	2.2	0.66	k_p=0.35	7	320	2.84

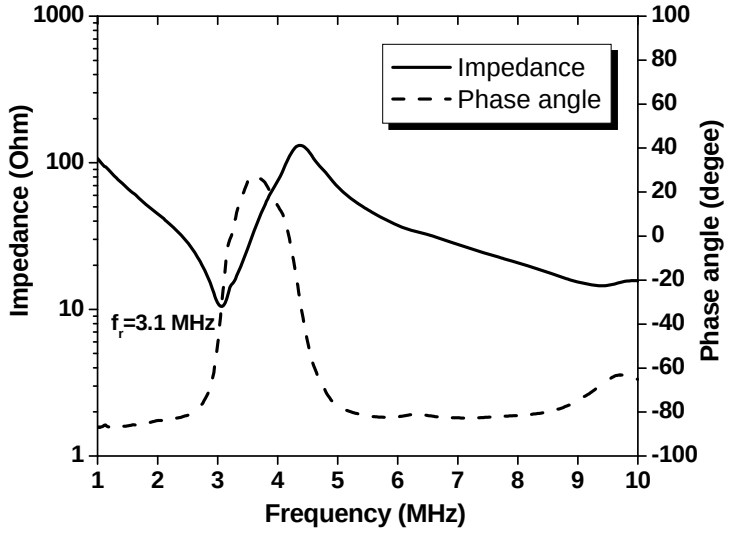

(a)

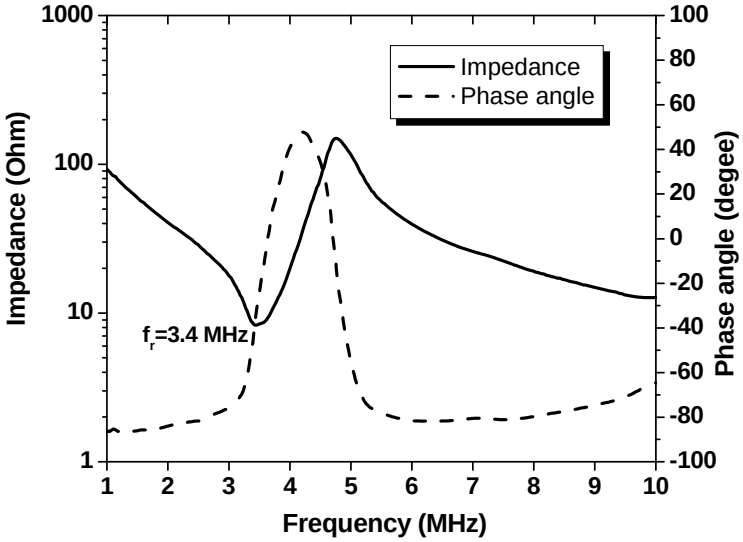

(b)

Fig. 7.11 Impedance and phase angle spectra of the (a) Gaussian and (b) linear composites in rectangular geometry.

For the three composites designed in annular geometry, Fig. 7.12 shows the planar and thickness mode resonances, along with a PZT disc for comparison. First, it is well known that thinner sample gives higher resonance frequency. It was found that for the PZT disc, composite without VFG, linear and Gaussian composites, with decreasing samples' thickness, the thickness mode resonance frequencies increased from 2.1 to 3.1, to 5.1 and to 5.7 MHz, respectively. Secondly, it is clear that the PZT disc had two main resonance modes: planar and thickness modes, and the planar mode is strong compared to thickness mode. Furthermore, many harmonic peaks of the fundamental planar mode resonance were observed which may cause the coupling between the planar and thickness mode resonances. In contrast, the three annular composites had only one main resonance mode: thickness mode. Their planar mode resonances became much weaker (shown in Fig. 12(b) and (c)), thus less coupling was expected between the planar and thickness modes. As a further evidence for this, the annular composites were found to have higher thickness coupling factors (k_t: ~0.66-0.72) and smaller planar coupling factors (k_p: ~0.35-0.37), compared to the PZT disc. The similar trend has been previously reported in the studies of a concentric ring composite fabricated by laser cutting and a PZT disc with destroyed geometry by chemical etching[151,152]. Therefore, an annular composite is more suitable than a ceramic disc for the ultrasound transducers which usually work in thickness mode. Thirdly, for all the three annular composites, small shoulders were observed at higher frequencies than the fundamental thickness mode resonances. It was probably caused by the geometry of the annular samples, which had a connection between individual rings due to the continuous nature of Micropen^{TM} deposition.

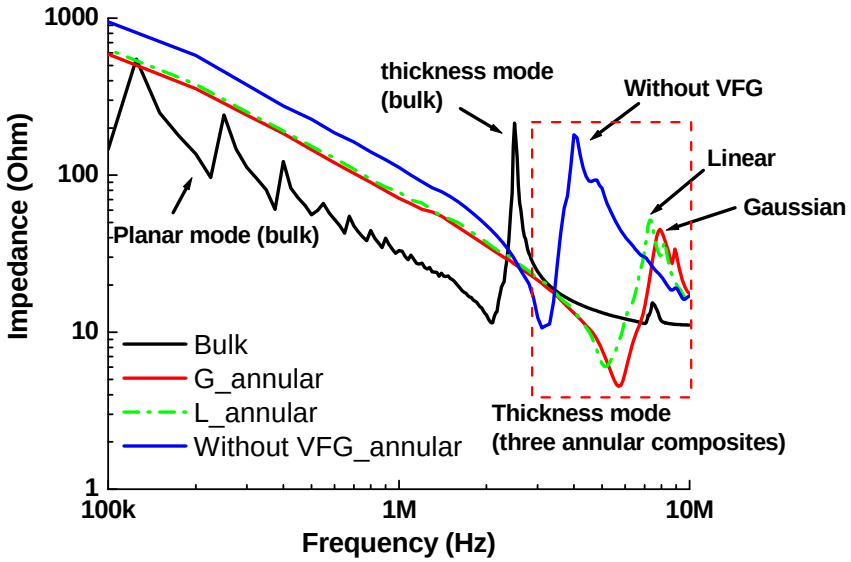

(a)

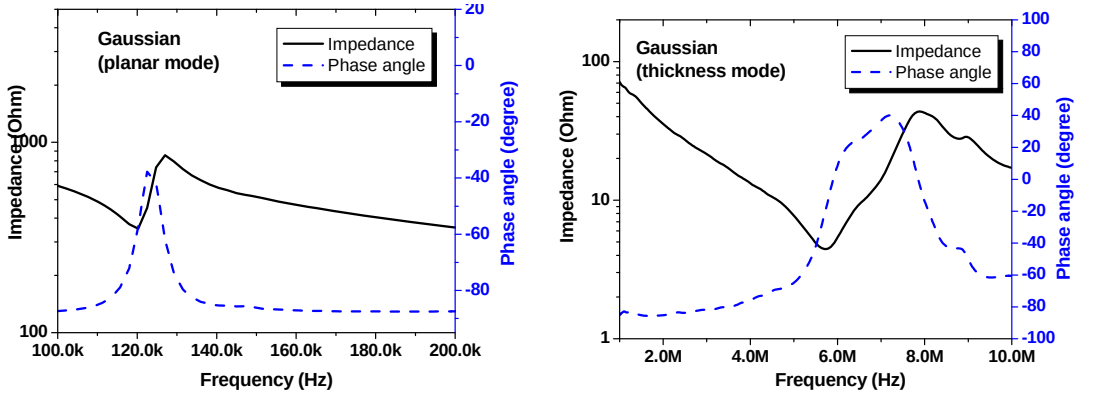

(b)

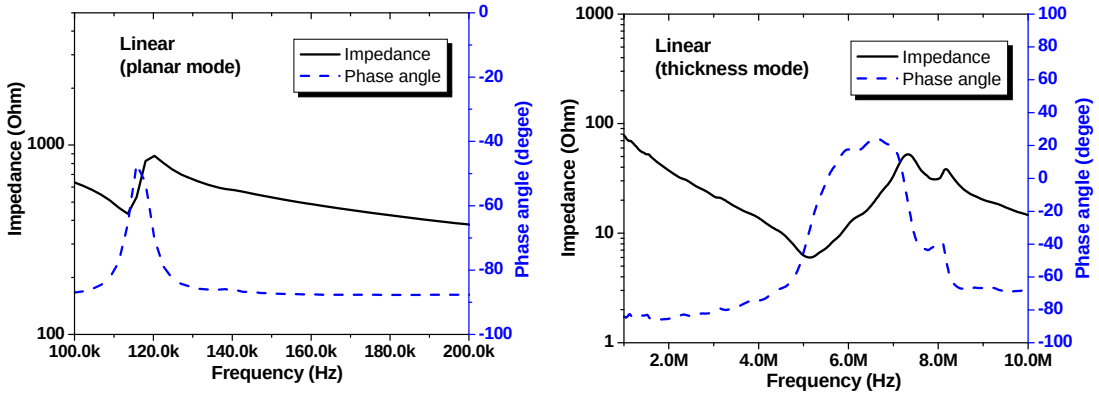

(c)

Fig. 7.12 Plots of the impedance characteristics of (a) a PZT disc and the three composites in annular geometry, (b) magnified portions of Gaussian and (c) linear composites.

The vibration amplitude profiles of the composites in rectangular and annular geometries are shown in Fig. 7.13 (a) and (b), respectively. The measurements were done as a function of the distance from center to edge of the composites, using the fotonic fiber-optic probe described in section 7.2.3. Since the probe had a diameter of 3.1 mm, and moved in steps of 1 mm, the recorded vibration amplitude was an average value and had a partial overlap in the two measurements in succession. As expected, the four gradient samples both in rectangular and annular geometries showed a decrease in the vibration amplitude with increasing distance from center. In addition, the vibration amplitude of the Gaussian composites dropped less compared to the linear composites. This is because the ceramic volume fraction of the Gaussian distribution decreases more slowly with the distance than that in the linear distribution[153 154]. On the contrary, the vibration amplitude of the rectangular composite without VFG was nearly constant with increasing distance. This behavior should be related to the constant ceramic content across the sample. While for the annular composite without VFG, at first a drop of ~ -3dB was observed at the distance of 2 mm. Then in the region of 2-4 mm, the amplitude did not vary much compared to the VFG annular samples. This could be explained by the design of the annular composite without VFG, which had a solid ceramic center and ceramic rings with constant spacing. It can be concluded that using the Micropen^{TM} technique, VFG composites were developed to control the vibration amplitude, and different gradients generated different vibration variations.

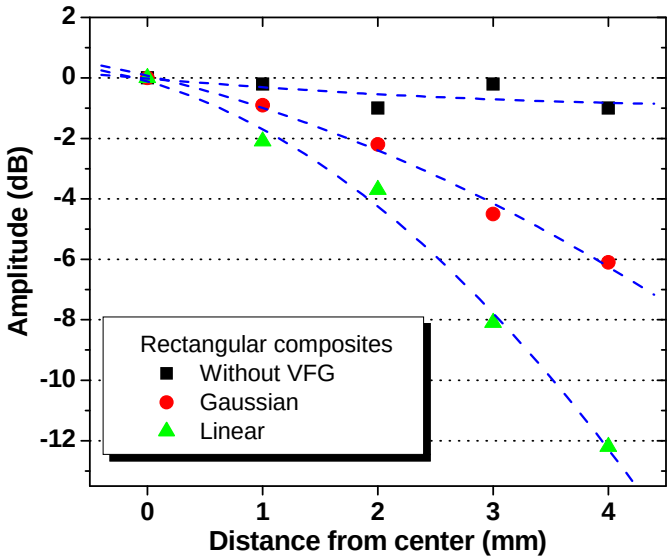

(a)

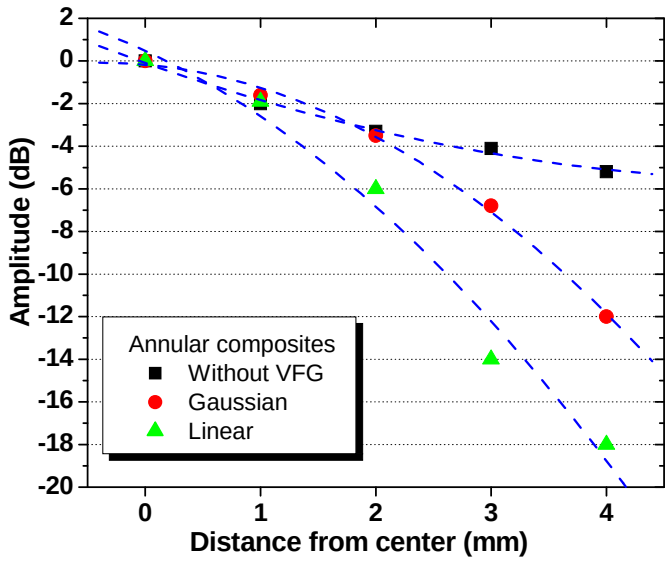

(b)

Fig. 7.13 The vibration amplitude profiles for the composites with and without VFG (a) in rectangular geometry and (b) in annular geometry.

7.4 Summary

Volume fraction gradient (VFG) composites have been fabricated by the Micropen^{TM} direct-write for the first time, with the intention of decreasing side lobe intensity in medical ultrasound transducers. The VFG composites with Gaussian and linear distributions in rectangular and annular geometries were designed and fabricated.

The VFG composites showed dielectric constant (K) of 540-640, dielectric loss (tanδ) of 2.1-2.3%, and good electromechanical properties (k_t=0.66-0.72, Q_m=5-9, d_{33}=260-320). The VFG composites in rectangular geometry showed clean thickness mode resonances, and the VFG composites in annular geometry were found to have reduced planar coupling factors (k_p=0.35-0.37).

The vibration profiles of the VFG composites were taken by measuring the displacements using a fiber-optic probe. The results showed that it was possible to control the vibration amplitude by using different ceramic volume fraction gradients.

CHAPTER8 CONCLUSIONS

In this thesis, a promising direct-write technique, Micropen^{TM} was investigated to develop novel two- and three-dimensional designs of various materials. Micropen^{TM} technique was successfully utilized to directly write poly(methyl methacrylate) (PMMA) and lead zirconate titanate (PZT) materials for a variety of applications. These studies include the direct writing of:

(1) Lines using PMMA/SiO_2 hybrid materials for optical applications;

(2) Thick films using modified sol-gel derived PZT ceramic pastes for MEMS or high frequency medical imaging applications;

(3) Novel skeletal structures using ceramic/binder based pastes for piezoelectric ceramic/polymer composites for transducers.

The following conclusions were drawn on the basis of numerous experiments using the Micropen^{TM} technique in the areas described below.

1. Direct-write of PMMA solutions and PMMA/SiO_2 hybrid materials：

- The study on the rheological properties of PMMA solutions showed that the solutions of 10, 15, 20, 25 and 30 wt% had lower viscosities (0.007-2 Pa·s) with Newtonian behavior, while the solutions of 35 and 40 wt% had higher viscosities (6 and 28 Pa·s), a small degree of shear thinning and elasticity.

- Line writing with the PMMA solutions was successful for both the Newtonian and shear thinning behaviors. Line width decreased and line height increased with increasing solution concentration. The best line resolution was obtained as ~ 330 μm width and ~ 18 μm height, using the 40 wt% PMMA solution and a 250-μm pen tip.

- Nearly linear correlations were observed for the line width, line height, and line width×line height as a function of the solution concentration, indicating a good control of the amount of materials dispensed during writing.
- It was challenging to obtain high quality line starts and ends, but the middle of lines exhibited relatively good consistency for the PMMA solutions (20-40 wt%).
- Organic/inorganic PMMA/SiO_2 hybrid monoliths with three organic/inorganic ratios (P80, P50 and P20) were synthesized by a sol-gel process.
- Among the three monoliths, the P80 sample showed higher thermal stability than pure PMMA, homogenous microstructure with the most uniform distribution of SiO_2, and low absorption both in the visible and near infrared regions.
- PMMA/SiO_2 lines were successfully deposited by Micropen^{TM} using the P80 solution. The optimum line width was ~220-240 μm, and the single-layer thickness was ~5-7 μm using a 200-μm pen tip.

2. Direct-write of PZT thick films:

- PZT thick films (6-70 μm in thickness) on silicon substrates have been successfully fabricated by Micropen^{TM} for the first time.
- The writing materials were derived from a modified sol-gel process, by dispersing PZT powder (~0.5 μm) in a sol-gel solution with different solids loadings (~15, 20, 25 and 30 vol%).
- The pastes exhibited shear thinning behavior with viscosities < 20 Pa·s at lower shear rates (1 s^{-1}) and < 3 Pa·s at higher shear rates (20 s^{-1}).

- The thick films were annealed at low temperature (700 ºC) for a short time (~ 2min).
- A Micropen^{TM} writing parameter, "cross section", was crucial for the control of film thickness. For example, using the 15 wt% paste, single-layer thickness was achievable from 1.5 to 7.8 μm by varying the "cross section" of deposition parameter.
- The microstructure revealed the film consisted of two different grains which came from the original commercial powder and the crystallized grains derived from the sol-gel solution.
- Using the 15 vol% paste, a 250-μm pen tip and "cross section"=10 mil^2, a 16-μm film was deposited by four layers on a silicon substrate.
- The films had comparable dielectric and ferroelectric properties with those of the films fabricated by other techniques: dielectric constant (K) of 870, dielectric loss (tanδ) of 4.1%, remanent polarization (P_r) of 12.2 μC/cm^2, and coercive field (E_c) of 27 kV/cm.

3. Direct-write of PZT skeletal structures of ceramic/polymer composites:

- PZT ceramic/polymer composites with 2-2 connectivity with and without volume fraction gradient (VFG) have been fabricated by Micropen^{TM} for the first time.
- A ceramic/binder based PZT paste with solids loading of 35 vol% was prepared as a writing material. It exhibited shear thinning behavior with a viscosity of ~45 Pa·s at lower shear rates (0.1 s^{-1}) and ~3 Pa·s at higher shear rates (20 s^{-1}).

- The writing parameter, "cross section", was important for the dimensional control of the deposited PZT lines. Line width and line height increased almost lineally with increasing the "cross section".

- The ceramic skeletal structures were sintered to full density, with good bonding among layers.

- Using a 100-μm pen tip, "cross section"=20 mil^2, typical one-layer thickness of the green and sintered ceramic line heights were ~60 and ~50 μm, respectively; and the green and sintered line widths were ~145 and ~120 μm, respectively.

- A ceramic/polymer composite containing 30 vol% PZT was fabricated, and the aspect ratio of ceramic elements (thickness to width) was ~ 3.0. The composite with thickness of ~360 μm showed the resonance frequencies of ~ 4 MHz, and dielectric and electromechanical properties of K=650, tanδ=2.1, k_t=0.60, Q_m=7 and d_{33} = 210 pC/N. Such results indicate that Micropen^{TM} direct-write has the potential to fabricate miniaturized 2-2 composites and composites with novel designs for medical imaging transducers.

- The VFG PZT/polymer composites with two types of gradients (Gaussian and linear distributions) and two geometries (rectangular and annular) were designed and fabricated.

- The average dielectric and electromechanical properties of the VFG composites were: K=540-640, tanδ=2.1-2.3%, k_t=0.66-0.72, Q_m=5-9 and d_{33}=260-320 pC/N.

- The VFG composites in rectangular geometry showed clean thickness mode resonances, and the VFG composites in annular geometry were found to have reduced planar coupling factors (k_p=0.35-0.37) which is desirable for medical imaging transducers.
- The vibration profiles of the VFG composites showed maximum output at center with gradual decreasing towards edge of the composites.

CHAPTER9 SUGGESTIONS FOR FUTURE WORK

In this thesis, a promising rapid prototyping technique, Micropen^{TM} direct-write was investigated for the direct writing of a variety of materials for different applications. Future work could focus on the aspects described below:

1. Direct-write of lines for optical applications:

- The lab-developed organic/inorganic materials (PMMA/SiO_2) with hydrogen bonding between the organic and inorganic phases were used in this study. For future work, commercially available materials could be used, such as fluorinated polymers or organic/inorganic hybrids with covalent bonding. The use of these materials could simplify the synthesis process, and thus we could focus more on Micropen^{TM} deposition and the characterization of fabricated components.

- Due to the instrument limitation in our group, no optical properties were measured for the deposited PMMA/SiO_2 lines. For further study, the function of guiding light and propagation loss at a certain wavelength could be measured by a waveguide test system equipped with a laser.

2. Direct-write of thick films:

- The pastes derived from a modified sol-gel were used in this work as writing materials for the direct write of thick films on silicon substrates. A separation between the PZT powder and the sol-gel matrix was observed after the pastes were left in a syringe for several days, especially for the pastes with higher solids loadings (>15 wt%). A stable paste is important to achieve homogenous films with good properties. Therefore,

an appropriate dispersant could be added to disperse the PZT powder more uniformly in the sol-gel solution. Another approach could be using PZT sol-gel solution with higher viscosity, simply by increasing the sol-gel solution concentration. The viscosity, uniformity and stability of the pastes of dispersing same amount of PZT powder in PZT sol-gel solutions with different viscosities could be studied. Then the optimum composition could be used for Micropen^{TM} deposition.

- Alternately, a ceramic/binder based paste could be used instead of a sol-gel derived paste. The choice of materials could be either a commercial paste or a lab-developed paste with a selected sintering aid, to achieve low temperature heat treatment desirable for silicon substrates.

- For high frequency medical ultrasound applications, thick-film transducers could be built using conventional transducer fabrication methods and silicon etching.

- To explore Micropen^{TM} capability of writing different features, the direct-write small circles and dots instead of rectangular geometry might be an interesting direction. Based on our preliminary work (refer to chapter 5), the future work could be the investigation on what is the smallest dimension of deposited circles or dots, and how is the continuity of direct-write of continuous dots or short lines. In addition, to obtain smooth and uniform surface, the materials should exhibit small degree of shear thinning or nearly Newtonian behavior. Therefore, either modified sol-gel derived pastes (< or ~ 15 vol%) or ceramic/binder based pastes with lower ceramic loading (<35 vol%) could be the choices of materials. Furthermore, smaller pen tips should be used for the deposition of finer structures with better uniformity, and Micropen^{TM} writing parameters should be carefully adjusted for high quality starts and ends of circles and dots.

3. Direct-write of skeletal structures of piezoelectric ceramic/polymer composites:

- Higher aspect ratio of ceramic elements is helpful to improve piezoelectric properties of composites. PZT pastes with higher solid loadings (>45 vol%) could be prepared to achieve higher degree of shear thinning and higher elasticity. Alternatively, materials used for robocasting deposition might be modified for Micropen^{TM} deposition to obtain even higher aspect ratios. In addition, smaller pen tips (< or ~ 100 μm in inner diameter) might be used for this purpose too.

REFERENCES

[1]A. Piqué, D.B. Chrisey, "Direct-write technologies for rapid prototyping applications: sensors, electronics, and integrated power sources", Academic press, USA, 2002.

[2] G.M. Gratson, "Colloidal and polyelectrolyte inks for direct-write assembly of 3D periodic structures", Ph.D. thesis, University of Illinois at Urbana-Champaign, 2005.

[3]A. Safari, J. Cesarano III, P.G. Clem, B. Bender, "Fabrication of advanced functional electroceramic components by layered manufacturing (LM) methods", IEEE-Proceedings of the 13th IEEE International Symposium on the Applications of Ferroelectrics (ISAF), p1, 2002.

[4] J.A. Lewis, G.M. Gratson, "Direct writing in three dimensions", Mater. Today, 7, p32, 2004.

[5] J.A. Lewis, J.E. Smay, J. Stuecker, J. Cesarano III, "Direct ink writing of three-dimensional ceramic structures", J. Am. Ceram. Soc., 89(12), p3599, 2006.

[6] J.A. Lewis, G.M. Gratson, "Direct writing in three dimensions", Mater. Today, July/August 2004.

[7] P. Calvert, "Inkjet printing for materials and devices", Chem. Mater., 13, p3299, 2001.

[8] X. Ding, Y. Li, D. Wang, Q. Yin, "Fabrication of $BaTiO_3$ dielectric films by direct ink-jet printing", Ceram. Inter., 30, p1885, 2004.

[9] D.H. Lee, B. Berby, "Preparation of PZT suspensions for direct ink jet printing", J. Eur. Ceram. Soc., 24, p1069, 2004.

[10] K.A.M. Seerden, N. Reis, J.R.G. Evans, B. Derdy, *et al.,* "Ink-jet printing of wax-based alumina suspension", J. Am. Ceram. Soc., 84(11), p2514, 2001.

[11] X. Zhao, J.R.G. Evans, M.J. Edirsinghe, "Direct ink-jet printing of vertical walls", J. Am. Ceram. Soc., 85(8), p2113, 2002.

[12] R. Noguera, M. Lejeune, T. Chartier, "3D fine scale ceramic components formed by ink-jet prototyping process", J. Eur. Ceram. Soc., 25, p2055, 2005.

[13] C.B. Arnold, P. Serra and A. Piqué, "Laser direct-write techniques for printing of complex materials", Mater. Bull. 32, Jan. 2007.

[14] A. Piqué, D.B. Chrisey, H.D. Wu, *et al.*, "Direct writing of electronic and sensor materials using a laser transfer technique", J. Mater. Res., 15(9), p1872, Sep. 2000.

[15] J.A. Barron, P. Wu, B.R. Bringeisen, *et al.*, "Biological laser printing: A novel technique for creating heterogeneous 3-dimensional cell patterns", Biomedical Microdevices, 6(2), p139, 2004.

[16] C. Zhang, D. Liu, H-D. Wu, D.B. Chrisey, *et al.*, "Laser direct-write and its application in low temperature co-fired ceramic (LTCC) technology", Microelectro. Eng., 70, p41, 2003.

[17] J.M. Fitz-Gerald, A. Piqué, D.B. Chrisey, *et al.*, "Laser direct writing of phosphor screens for high-definition displays", Appl. Phy. Lett., 76(11), 2000.

[18] http://www.micropen.com

[19] Micropen™ manual, model 406, Micropen Division of OhmCraft Inc., NY, USA.

[20] D. Dimos, P. Yang, T.J. Garino, M.V. Raymoud, M.A. Rodriguez, "Direct-write fabrication of integrated, multilayer ceramic components", in Solid Freeform Fabrication Symposium Proceedings, Austin, TX, University of Texas at Austin, p33, 1999.

[21] B.H. King, D. Dimos, P. Yang, S.L. Morissette, "Direct-write fabrication of integrated, multilayer ceramic components", J. Electroceram., 3:2, p173, 1999.

[22] S.L. Morissette, J.A. Lewis, P.G. Clem, J. Cesarano III, and D.B. Dimos, "Direct-write fabrication of $Pb(Nb,Zr,Ti)O_3$ devices: influence of paste rheology on print morphology and component properties", J. Am. Ceram. Soc., 84(11), p2462, 2001.

[23] V. Tohver, S.L. Morissette, J.A. Lewis, B.A. Tuttle, J.A. Voigt, and D.B. Dimos, "Direct-write fabrication of zinc oxide varistors", J. Am. Ceram. Soc., 85(1), p123, 2002.

[24] M. Allahverdi and A. Safari, "Direct-write PZT thick films", IEEE-Proceedings of the 14th IEEE International Symposium on the Applications of Ferroelectrics (ISAF), p250, 2004.

[25] M. Kunduraci, W.K. Simon, E.K. Akdogan, and A. Safari, "Paraelectric $(Ba_{0.6}Sr_{0.4})TiO_3$ thick films by direct-write", Proceedings of the 14th IEEE International Symposium on the Applications of Ferroelectrics (ISAF), p21, 2004.

[26] J.S. Reed, "Principles of Ceramics Processing" (2nd edition), John Wiley & Sons Inc., 1995.

[27] E.T. Severs, "Rheology of Polymers", Reinhold Publishing Corporation, New York, 1962.

[28] TA instruments manual: "Rheology solutions-oscillation".

[29] V.D. Noto, "Zeolitic inorganic-organic polymer electrolyte based on oligo(ethylene glycol)600 K_2PdCl_4 and $K_3Co(CN)_6$", J. Phys. Chem. B, 600, 104(44), p10116, 2000.

[30] C. Sanchez, B. Julián, P. Belleville, M. Popall, "Applications of hybrid organic-inorganic nanocomposites", J. Mater. Chem., 15, p3559, 2005.

[31] H. Schmidt, "New type of non-crystalline solids between inorganic and organic materials", J. Non-Cryst. Solids, 73, p681, 1985.

[32] "Sol-Gel Optics: Processing and Applications", edited by L.C. Klein, Kluwer Academic Publishers, Boston, 1994, J. Livage, F. Babonneau, C. Sanchez, p39.

[33] C. Sanchez, F. Ribot, "Design of hybrid organic-inorganic materials synthesized via sol-gel chemistry", New. J. Chem., 18, p1007, 1994.

[34] L.L. Díaz-Flores, P.P. Horley, J. González-Hernández, J.J. Pérez-Bueno, Yu.V. Vorobiev, P.M. Gorley, "Molecular aggregation and shape effects in the optical spectra of organic dye molecules in SiO_2 and SiO_2-PMMA matrices", J. Phys. Chem. Solids, 64, p2409, 2003.

[35] J. Guan, B. Chen, Y. Sun, H. Liang, Q. Zhang, "Effects of synergetic ligands on the thermal and radiative properties of $Eu(TTA)_3nL$-doped poly(methyl methacrylate)", J. Non-Cryst. Solids, 351, p829, 2005.

[36] Y.Q. Fu, Q.Q. Ni, M. Iwamoto, "Interaction of PMMA-SiO_2 in PMMA-silica hybrids under acid catalyst and catalyst-less conditions", J. Non-Cryst. Solids, 351, p760, 2005.

[37] G. Gu, Z. Zhang, H. Dang, "Hydrophobic inorganic-organic thin films with a low coefficient of friction", Mater. Res. Bull., 39, p1037, 2004.

[38] F. Mammeri, E. Le Bourhis, L. Rozes, C. Sanchez, "Elaboration and mechanical characterization of nanocomposites thin films, Part I: Determination of the mechanical properties of thin films prepared by *in situ* polymerization of tetraethoxysilane in poly(methyl methacrylate)", J. Eur. Ceram. Soc., 26, p259, 2006.

[39] C.J.T. Landry, B.K. Coltrain, B.K. Brady, "In situ polymerization of tetraethoxysilane in poly(methyl methacrylate): morphology and dynamic mechanical properties", Polymer, 33(7), p1486, 1992.

[40] Y.T. Wang, T.C. Chang, Y.S. Hong, H.B. Chen, "Effect of interfacial structure on the thermal stability of poly(methyl methacrylate)-silica hybrids", Thermochim. Acta, 397, p219, 2003.

[41] C.A. Avila-Herrera, O. Gómez-Guzmán, J.L. Almaral-Sánchez, J.M. Yáñez-Limón, J. Muñoz-Saldaña, R. Ramírez-Bon, "Mechanical and thermal properties of SiO_2-PMMA monoliths", J. Non-Cryst. Solids, 352, p3561, 2006.

[42] C. Li, J. Wu, J. Zhao, D. Zhao, Q. Fan, "Effect of inorganic phase on polymeric relaxation dynamics in PMMA/silica hybrids studied by dielectric analysis", Eur. Polym. J., 40, p1807, 2004.

[43] C.J.T. Landry, B.K. Coltrain, J.A. Wesson, N. Zumbulyadis, J.L. Lippert, "*In situ* polymerization of tetraethoxysilane in polymers: chemical nature of the interactions", Polymer, 33(7), p1496, 1992.

[44] "Sol-Gel Optics: Processing and Applications", edited by L.C. Klein, Kluwer Academic Publishers, Boston, 1994, L.C. Klein, p215.

[45] L. Bian, X. Qian, J. Yin, Z. Zhu, Q. Lu, "Preparation and luminescence property of the PMMA/SiO_2/EuL_3•$2H_2O$ hybrids by a sol-gel method", Mater. Sci. Eng. B, 100, p53, 2003.

[46] X. Zhang, Z. Zhao, M. Qian, P. Plante, "Fabrication of waveguide splitters using sol-gel hybrid materials", IEEE-International meeting on Microwave Photonics, Oct., 2006.

[47] P. Etienne, P. Coudray, J. Porque, Y. Moreau, "Active erbium-doped organic-inorganic waveguide", Opt. Comm., 174, p413, 2000.

[48] K.F. Silveira, I. Valéria, P. Yoshida, S.P. Nunes, "Phase separation in PMMA/silica sol-gel systems", Polymer, 36(7), p1425, 1995.

[49] A.A. Hamza, I.M. Fouda, T.Z.N. Sokkar, M.A. El-Bakary, "Opto-thermal properties of fibers: effect of anisotropic optical parameters in polypropylene fibers as a function of annealing process", Polym. Testing, 15, p245, 1996.

[50] Z.H. Huang, K.Y. Qiu, "The effects of interactions on the properties of acrylic polymers/silica hybrid materials prepared by the *in situ* sol-gel process", Polymer, 38(3) p521, 1997.

[51] H. Wang, P. Xu, W. Zhong, L. Shen, Q. Du, "Transparent poly(methyl methacrylate) /silica/zirconia nanocomposites with excellent thermal stabilities", Polym. Degrad. Stab., 87, p319, 2005.

[52] A.B. Wojcik, A. Ting, L.C. Klein, "High molecular weight poly(ethylene oxide)/silica hybrids by the sol-gel process", Mater. Sci. Eng. C, 6, p115, 1998.

[53] Y. Yang, Y. Dan, "Preparation of PMMA/SiO2 composite particles via emulsion polymerization", Colloid Polym. Sci., 281, p794, 2003.

[54] R. Takahashi, K. Nakanishi, N. Soga, "Aggregation behavior of alkoxide-derived silica in sol-gel process in presence of poly(ethylene oxide)", J. Sol-Gel Sci. Technol., 17, p7, 2000.

[55] C.K. Chan, S.L. Peng, I.M. Chu, S.C. Ni, "Effects of heat treatment on the properties of poly(methyl methacrylate)/silica hybrid materials prepared by sol-gel process", Polymer, 42, p4189, 2001.

[56] Y.Y. Yu, C.Y. Chen, W.C. Chen, "Synthesis and characterization of organic-inorganic hybrid thin films from poly(acrylic) and monodispersed colloidal silica", Polymer, 44, p593, 2003.

[57] "Characterization of Materials", edited by E.N. Kaufmann, John Wiley & Sons Publications, Hoboken, New Jersey, p691, 2003.

[58] H. Wang, W. Zhong, P. Xu, Q.G. Du, "Properties of polyamide/silica nanohybrids from silicic acid oligomer", Macromol. Mater. Eng., 289, p793, 2004.

[59] "Electroceramics: production, properties and microstructures", edited by W.E. Lee and A. Bell, The University Press, Cambridge, UK, 1994, p57, J.S. Obhi, A. Patel and D.A. Tossell, "Sol-gel ferroelectric PZT thin films for non-volatile memory applications".

[60] M.J. Lefevre, J.S. Speck, R.W. Schwartz, D. Dimos, S.J. Lockwood, "Microstructural development in sol-gel derived lead zirconate titanate thin films: The role of precursor stoichiometry and processing environment", J. Mater. Sci., 11(8), p2076, 1996.

[61] G. Yi, Z. Wu, M. Sayer, "Preparation of Pb(Zr, Ti)O_3 thin films by sol gel processing: electrical, optical and electro-optic properties", J. Appl. Phys., 64(5), p2717, 1988.

[62] J.B. Blum, S.R. Gurkovich, "Sol-gel derived $PbTiO_3$", J. Mater. Sci., 20, p4479, 1985.

[63] C. Livage, A. Safari and L. C. Klein, "Sol-gel lead zirconate-titanate thin films: effects of solution concentration", IEEE-ISAF92, p447, 1992.

[64] G. Yi and M. Sayer, "Sol-gel processing of thick PZT films", IEEE-ISAF92, p289, 1992.

[65] H. Brunckova, L. Medvecky, J. Briancin, K. Saksl, "Influence of hydrolysis conditions of the acetate of sol-gel process on the stoichiometry of PZT powders", Ceram. Int., 30, p453, 2004.

[66] Q.F. Zhou, H.L.W. Chan, C.L. Choy, "PZT ceramic/ceramic 0-3 nanocomposite films for ultrasonic transducer applications", Thin Solid Films, 375, p95, 2000.

[67] "Piezoelectric an acoustic materials for transducer applications", edited by A. Safari, E.K. Akdogan, Springer Science LLC., 2008, p413, B. Nazanin, "Chapter 20, Piezoelectric MEMS: materials and devices".

[68] B. Belgacem, F. Calame, P. Muralt, "Piezoelectric micromachined ultrasonic transducers with thick PZT sol-gel films", J. Electroceram, 19, p369, 2007.

[69] R. Lou-Moeller, C.C. Hindrichsen, L.H. Thamdrup, *et. al.*, "Screen-printed piezoceramic thick films for miniaturized devices", J. Electroceram., 19, p333, 2007.

[70] R. Seveno, P. Limousin, D. Averty, J. Chartier, R.L. Bihan, H.W. Gundel, "Preparation of multi-coating PZT thick films by sol-gel method onto stainless steel substrates", J. Eur. Ceram. Soc., 20, p2025, 2000.

[71] D.A. Barrow, T.E. Petroff, M. Sayer, "Thick ceramic coatings using a sol-gel based ceramic-ceramic 0-3 composite", Surface and Coating Tech., 76-77, p113, 1995.

[72] Z. Wang, W. Zhu, C. Zhao, O.K. Tan, "Dense PZT thick films derived from sol-gel based nanocomposites process", Mat. Sci. Eng. B, 99, p56, 2003.

[73] D.A. Barrow, T.E. Petroff, R. P. Tandon, M. Sayer, "Characterization of thick lead zirconate titanate films fabricated using a new sol gel based process", J. Appl. Phys., 81 (2), p876, 1997.

[74] Q.F. Zhou, H.L.W. Chan, C.L. Choy, "PZT ceramic/ceramic 0-3 nanocomposite films for ultrasonic transducer applications", Thin Solid Films, 375, p95, 2000.

[75] D. Xia, M. Liu, Y. Zeng, C. Li, "Fabrication and electrical properties of lead zirconate titanate thick films by the new sol-gel method", Mat. Sci. Eng. B, 87, p160, 2003.

[76] Q.F. Zhou, K.K. Shung, Y. Huang, "Improvement electrical properties of sol-gel derived lead zirconate titanate thick films for ultrasonic transducer applications", J. Mater. Sci., 42, p4480, 2007.

[77] C. Livage, A. Safari, L.C. Klein, "Glycol-based sol-gel process for the fabrication of ferroelectric PZT thin films", J. Sol-Gel Sci. Tech., 2, p605, 1994.

[78] C. Zhao, Z. Wang, W. Zhu, X. Yao, W. Liu, "PZT thick films fabrication using a sol-gel based 0-3 composite processing", Inter. J. Morden Phy. B, 16 (1 &2), p242, 2002.

[79] M. Allahverdi and A. Safari, “Direct-write PZT thick films”, IEEE-Proceedings of the 14th IEEE International Symposium on the Applications of Ferroelectrics (ISAF), p250, 2004.

[80] B. Jaffe, W.R. Cook, H. Jaffe, “Piezoelectric ceramics”, Academic Press Inc., New York, 1971.

[81] R.E. Newnham, “Properties of materials anisotropy, symmetry, structure”, Oxford University Press Inc., New York, 2005.

[82] F. Mohammadi, “An investigation on the development of novel design piezoelectric actuator designs by fused deposition of ceramics (FDC)”, Ph.D. Thesis, Rutgers University, New Brunswick, NJ, 2001.

[83] K.K. Shung, “Advances in Ultrasound”, IEEE engineering in medicine and biology, 15, p18, 1996.

[84] T.R. Gururaja, “Piezoelectric transducers for medical ultrasonic imaging”, ISAF1990, p259, 1990.

[85] A. Safari, V.F. Janas, A. Bandyopadhyay, “Development of fine-scale piezoelectric composites for transducers”, Ceramics Processing, 43(11A), p2849, 1997.

[86] T.R. Gururaja, “Piezoelectrics for medical ultrasonic imaging”, Am. Ceram. Soc. Bull., 73, p50, 1994.

[87] K. Li, H.L.W. Chan, C.L. Choy, “Samarium and manganese-doped lead titanate ceramic fiber/epoxy 1-3 composite for high-frequency transducer application”, IEEE Trans. Ultrason. Ferroelectr. Freq. Control, 50(10), p1371, 2003.

[88] http:// www.usra.ca/basic_p

[89] W.A. Smith, “Composite piezoelectric materials for medical ultrasonic imaging transducers-A review”, IEEE-ISAF, p249, 1986.

[90] R. Panda, “Development of novel piezoelectric composites by solid freeform fabrication techniques”, Ph.D. thesis, Rutgers University, New Brunswick, NJ, 1998.

[91] J. Chen, R. Panda, “Review: Commercialization of piezoelectric single crystals for medical imaging applications”, IEEE Ultrason. Symp., p235, 2005.

[92] W.A. Smith, A.A. Shaulov, “Composite piezoelectrics: basic research to a practical device”, Ferroelectrics, 87, p309, 1988.

[93] T. Ritter, X. Geng, K.K. Shung, P.D. Lopath, S. Park, T.R. Shrout, "Single crystal PZN/PT-polymer composites for ultrasound transducer applications", IEEE Trans. Ultrason. Ferroelectr. Freq. Control, 47(4), p792, 2000.

[94] K.C. Cheng, H.L.W. Chan, C.L. Choy, Z. Yin, "Single crystal PMN-0.33PT/Epoxy 1-3 composites for ultrasonic transducer applications", IEEE Trans. Ultrason. Ferroelectr. Freq. Control, 50(9), p1177, 2003.

[95] K. Ren, Y. Liu, X. Geng, H.F. Hofmann, Q.M. Zhang, "Single crystal PMN-PT/epoxy 1-3 composite for energy-harvesting application", IEEE Trans. Ultrason. Ferroelectr. Freq. Control, 53(3), p631, 2006.

[96] B. Jadidian, N.M. Hagn, A.A. Winder and A. Safari, "25 MHz ultrasonic transducers with lead free piezoceramic, 1-3 PZT fiber-epoxy composite, and PVDF polymer active elements", IEEE Trans. Ultrason. Ferroelectr. Freq. Control, 56(2), p368, 2009.

[97] S.H. Choy, W.K. Li, H.K. Li, K.H. Lam, H.L.W. Chan, "Study of BNKLBT-1.5 lead-free ceramic/epoxy 1-3 composites", J. Appl. Phys., 102, p114111, 2007.

[98] Y. Zhen, J. Li, K. Wang, "Fabrication and electrical properties of fine-scale 1-3 piezoceramic/epoxy composites using (K,Na)NbO_3-based lead-free ceramics", Ferroelec., 358, p161, 2007.

[99] Q.Q. Zhang, F.T. Djuth, Q.F. Zhou, C.H. Hu, J.H. Cha, K.K. Shung, "High frequency broadband PZT thick film ultrasonic transducers for medical imaging applications", Ultrasonics, 44, pe711, 2006.

[100] R.E. Newnham, D.P. Skinner, L.E. Cross, "Connectivity and piezoelectric-pyroelectric composites", Mater. Res. Bull., 13, p525, 1978.

[101] D. Hall, J.T. Bennett, G. Hayward, "the design and evaluation of ultrasonic arrays using 1-3 connectivity composites", Proc. of SPIE, 1733, p216, 1992.

[102] G.M. Lous, "Fabrication of piezoelectric ceramic/polymer composite transducers for medical imaging applications using fused deposition of ceramics", M.S. Thesis, Rutgers University, New Brunswick, NJ, 1999.

[103] W.A. Smith, "The application of 1-3 piezocomposites in acoustic transducers", IEEE-ISAF, p145, 1990.

[104] Y. Zhen, J. Li, "Preparation and electrical properties of fine-scale 1-3 lead zirconic titanate/epoxy composite thick films for high-frequency ultrasonic transducers", J. Appl. Phys., 103, p084119, 2008.

[105] Y. Shui, Q. Xue, "Dynamic characteristics of 2-2 piezoelectric composite transducers", IEEE Trans. Ultrason. Ferroelectr. Freq. Control, 44(5), p1110, 1997.

[106] R. Lerch, "Simulation of piezoelectric devices by two-and three-dimensional finite elements", IEEE Trans. Ultrason. Ferroelectr. Freq. Control, 37, p233, 1990.

[107] W. Hackenberger, S. Kwon, P. Rehrig, et. al., "2-2 PZT-polymer composites for high frequency (>20 MHz) ultrasound transducers", 2002 IEEE Ultrason. Symp., 2, p1253, 2002.

[108] V.F. Janas, A. Safari, "Overview of fine-scale piezoelectric ceramic/polymer composite processing", J. Am. Ceram. Soc., 78(11), p2945, 1995.

[109] K.K. Shung, J.M. Cannata, Q.F. Zhou, "Piezoelectric materials for high frequency medical imaging applications: A review", J. Electroceramics, 19, p139-145, 2007.

[110] T.A. Ritter, T.R. Shrout, K.K. Shung, "Development of high frequency medical ultrasound arrays", IEEE Ultrason. Symp., p1127, 2001.

[111] R. Liu, D. Knapik, K.A. Harasiewicz, F.S. Foster, "Fabrication of 2-2 piezoelectric composites by interdigital pair bonding", IEEE Ultrason. Symp., p973, 1999.

[112] R. Liu, K.A. Harasiewicz, F.S. Foster, "Interdigital pair bonding for high frequency (20-50 MHz) ultrasonic composite transducers, IEEE Trans. Ultrason. Ferroelectr. Freq. Control, 48(1), p299, 2001.

[113] J. Yin, M. Lukacs, K.A. Harasiewicz, F.S. Foster, "Ultra-fine piezoelectric composites for high frequency ultrasonic transducers", IEEE Ultrason. Symp., 3, p1962, 2004.

[114] S. Michau, P. Mauchamp, R. Dufait, "Piezocomposite 30 MHz linear array for medical imaging: design challenges and performances evaluation of a 128 elements array", 2004 IEEE Ultrason. Symp., p898, 2004.

[115] J. M. Cannata, J.A. Williams, Q. Zhou, T.A. Ritter, K.K. Shung, "Development of a 35-MHz piezo-composite ultrasound array for medial imaging", IEEE Trans. Ultrason. Ferroelectr. Freq. Control, 53(1), p224, 2006.

[116] K. Li, D. W. Zeng, K.C. Yung, et. al., "Study on ceramic/polymer composite fabricated by laser cutting", Mater. Chem. Phy., 75, p147, 2002.

[117] Y. Koh, C. Yoon, S. Lee, et.al., "Thermoplastic green machining for the fabrication of a piezoelectric ceramic/polymer composite with 2-2 connectivity", J. Am. Ceram. Soc., 88(4), p1060, 2005.

[118] B. Belgacem, F. Calame, P. Muralt, "Piezoelectric micromachined ultrasonic transducers with thick PZT sol gel films", J. Electroceram., 19, p369, 2007.

[119] G.M. Lous, I.A. Cornejo, T.F. McNulty, A. Safari, S.C. Danforth, "Fabrication of piezoelectric ceramic/polymer composite transducers using fused deposition of ceramics", J. Am. Ceram. Soc., 83(1), p12, 2000.

[120] S. Turcu, B. Jadidian, S.C. Danforth, A. Safari, "Piezoelectric properties of novel oriented ceramic-polymer composites with 2-2 and 3-3 connectivity", J. Electroceram., 9, p165, 2002.

[121] J.E. Smay, J. Cesarano III, B.A. Tuttle, J.A. Lewis, "Directed colloid assembly of linear and annular lead zirconate titanate arrays", J. Am. Ceram. Soc., 87(2), p293, 2004.

[122] O. Dufaud, P. Marchal, S. Corbel, "Rheological properties of PZT suspensions for stereolithography", J. Eur. Ceram. Soc., 22, p2081, 2002.

[123] R. Noguera, M. Lejeune, T. Chartier, "3D fine scale ceramic components formed by ink-jet prototyping process", J. Eur. Ceram. Soc., 25, p2055, 2005.

[124] A. Piqué, D.B. Chrisey, "Direct-write technologies for rapid prototyping applications: sensors, electronics, and integrated powder sources", Ed. by A. Piqué, D.B. Chrisey, Academic Press Inc., New York, 2001.

[125] S. Turcu, "Development and properties of novel oriented piezoelectric ceramic/polymer composites", M.S. thesis, Rutgers University, New Brunswick, NJ, 2002.

[126] IEEE Standard on Piezoelectricity, ANSI/IEEE Std. 176, (the Institute of Electrical and Electronics Engineers (IEEE), Inc., New York, 1987.

[127] E.K. Akdoğan, "Dielectric and piezoelectric properties of doped PZT ceramics", M.S. Thesis, METU, Ankara, Turkey, 1994.

[128] IRE Standards of Piezoelectric Crystals: Measurements of Piezoelectric Ceramics, IEEE, 1961.

[129] J.S. Reed, "Principles of Ceramics Processing", John Wiley & Sons Press Inc., New York, 1995.

[130] D. Dimos, P. Yang, T.J. Garino, et. al., "Direct-write fabrication of integrated, multilayer ceramic components", in *Proc. of Solid Freeform Fabrication Symp.*, Austin, TX, University of Texas at Austin, p33, 1997.

[131] T.R. Gururaja, R.E. Newnham, K.A. Klicker, et. al., "Composite piezoelectric transducers", Ultrason. Symp., p576, 1980.

[132] W.A. Smith, "The role of piezocomposites in ultrasonic transducers", IEEE Ultrason. Symp., 2, p755, 1989.

[133] T.R. Gururaja, W.A. Schulze, L.E. Cross, *et. al.*, "Piezoelectric composite materials for ultrasonic transducer application. Part I: resonant modes of vibration of PZT rod-polymer composites", IEEE Trans. Sonics Ultrasonics, SU-32 (4), p481, 1985.

[134] W. Cao, Q.M. Zhang, L.E. Cross, "Theoretical study on the static performance of piezoelectric ceramic-polymer composites with 2-2 connectivity", IEEE Trans. Ultrason. Ferroelec. Freq. Control, 40(2), p103, 1993.

[135] K.A. Snook, J. Zhao, C.H.F. Alvers, J.M. Cannata, T.A. Ritter, K.K. Shung, "Design, fabrication, and evaluation of high frequency, single-element transducers incorporating different materials", IEEE Trans. Ultrason. Ferroelectr. Freq. Control, 49(2), p169, 2002.

[136] J.M. Cannata, "High frequency (>20 MHz) ultrasonic arrays for medical imaging applications", Ph.D. thesis, The Pennsylvania State University, PA, 2004.

[137] "Piezoelectric an acoustic materials for transducer applications", edited by A. Safari, E.K. Akdogan, Springer Science LLC., 2008, p191, M. Lethiecq, F. Levassort, D. Certon, L.P. Tran-Huu-Hue, "Chapter 10, Piezoelectric transducer design for medical diagnosis and NDE".

[138] K.A. Snook, T.R. Shout, K.K. Shung, "Development of high frequency annular arrays for medical imaging", IEEE Ultrason. Symp., p865, 2003.

[139] C.E. Morton, G. R. Lockwood, "Design of a 40 MHz annular array", IEEE Ultrason. Symp., p1135, 2001.

[140] "Piezoelectric and acoustic materials for transducer applications", edited by A. Safari, E.K. Akdogan, Springer Science LLC., 2008, p431, K.K. Shung, J.M. Cannata, Q. Zhou. "Chapter 21, High-frequency ultrasonic transducers and arrays".

[141] K.A. Snook, C. Hu, T.R. Shrout, K.K. Shung, "High-frequency ultrasound annular-array imaging. Part I: Array design and fabrication", IEEE Trans. Ultrason. Ferroelectr. Freq. Control, 53(2), p300, 2006.

[142] J.A. Brown, C.E.M. Dáemore, G.R. Lockwood, "Design and Fabrication of annular arrays for high-frequency ultrasound", IEEE Trans. Ultrason. Ferroelectr. Freq. Control, 51(8), p1010, 2004.

[143] E.J. Gottlieb, J.M. Cannata, C. Hu, K.K. Shung, "Development of a high-frequency (>50 MHz) copolymer annular-array, ultrasound transducer", IEEE Trans. Ultrason. Ferroelectr. Freq. Control, 53(5), p1037, 2006.

[144] R.K. Panda, A.L. Kholkin, A. Safari, "Design and fabrication of volume fraction gradient piezoelectric composites for medical imaging applications", IEEE-ISAF, p265, 1998.

[145] C. Nakaya, H. Takeuchi, K. Katakura, "Ultrasonic transducer using piezoelectric composite", US Patent, No. 4658176, 1987.

[146] W.B. Walters, S. Ayter, J.A. Hossack, et al., "Ultrasound transducers with reduced sidelobes and method for manufacture thereof:", US Patent, No. 5410208, 1995.

[147] A. Safari, S.C. Danforth, R.K. Panda, G. Lous, et al., "Novel piezocomposites for ultrasonic transducer applications", IEEE Ultrason. Symp., p615, 1998.

[148] A. Safari, "Novel piezoelectric ceramic and composites for sensor and actuator applications", Mat. Res. Innovat., 2, p263, 1999.

[149] N.P. Vyshatko, P.M. Brioso, A.L. Kholkin, "Fiber-optic based method for the measurements of electric-field induced displacements in ferroelectric materials", Rev. Sci. Instr., 76, p085101, 2005.

[150] MTI-2000 Fotonic™ Sensor, instruction manual, Albany, NY.

[151] K. Li, D. W. Zeng, K.C. Yung, et. al., "Study on ceramic/polymer composite fabricated by laser cutting", Mater. Chem. Phy., 75, p147, 2002.

[152] S.E. Trolier, Q.C. Xu, R.E. Newnham, "A modified thickness extensional disk transducer", IEEE Trans. Ultrason. Ferroelectr. Freq. Control, 35(6), p839, 1988.

[154] A. Safari, M. Allahverdi, E.K. Akdogan, "Solid freeform fabrication of piezoelectric sensors and actuators", J. Mater. Sci., 41, p177, 2006.

Curriculum Vitae

Jingjing Sun

2004-2010	Ph.D., Materials Science and Engineering, Rutgers University, New Brunswick, NJ, USA
2002-2004	M.S, Materials Science and Engineering, Rutgers University, New Brunswick, NJ, USA
2000-2002	M.S, Materials Science and Engineering, Tsinghua University, Beijing, China
1995-2000	B.S, Materials Science and Engineering, Tsinghua University, Beijing, China

Publications

[1] J. Sun, E. K. Akdoğan, A. Safari, *et al.*, Development of 2-2 piezoelectric ceramic/polymer composites by direct-write technique (*Journal of Electroceramics,DOI:10.1007/s10832-009-9561-3, Jan2009 on-line available)*

[2] J. Sun, L.C. Klein, A. Safari, *et al.*, Characterization and optical properties of sol–gel processed PMMA/SiO_2 hybrid monoliths, *Journal of Non-Crystalline Solids*, 353 (2007), 2807-2812.

[3] J. Sun, M. Vittadello, A. Safari, *et al.*, Direct-write deposition of PZT thick films derived from modified sol-gel process, *Proceedings of the 15th IEEE International Symposium on the Applications of Ferroelectrics (IEEE-ISAF)* (2006), 57-60.

[4] J. Sun, J. Li and G. Sun, Effects of La_2O_3 and Gd_2O_3 on some properties of Ni-Zn ferrite, *Journal of Magnetism and Magnetic Materials*, 250 (2002), 20-24.

[5] J. Sun, J. Li, G. Sun, Synthesis of dense NiZn ferrites by spark plasma sintering, *Ceramics International*, 28 (2002), 855-858.

[6] J. Sun, J. Li, G. Sun, *et al.*, Dielectric and infrared properties of silicon carbide nanopowders, *Ceramics International,* 28, (2002), 741-745.

[7] B. Zhang, J. Li, J. Sun, *et al.*, Solid solution of Al and N in nano-sized α-SiC powder by carbothermal reduction of the xerogels of SiO_2-Al_2O_3, *Materials Letters,* 51 (2001), 219-224.